INVESTIGATING THE MECHANICS OF EARTHQUAKES USING MACROSCOPIC SEISMIC PARAMETERS

Thesis by

Anupama Venkataraman

In Partial Fulfillment of the Requirements

for the Degree of

Doctor of Philosophy

California Institute of Technology

Pasadena, California

2002

(Defended April 29, 2002)

"If we knew what it was we were doing, it would not be called research, would it?”

- *Albert Einstein.*

Acknowledgements

Through my six years at the Seismological Laboratory at Caltech, I have benefited from my interactions with several members of the lab, and express my sincere gratitude to all of them. Foremost among them have been the interesting and exciting discussions with my advisor, Hiroo Kanamori. I would like to thank him for his support, constant guidance and for his patience in helping me understand and learn the different aspects of seismology.

I would like to thank Rob Clayton and Joann Stock for carefully reviewing my papers and research statements, and Tom Heaton and Ares Rosakis for their enthusiasm about my research. Jim Mori at Kyoto University answered some of my basic questions and helped us with our first paper. Luis Rivera from the Institut de Physique du Globe de Strasbourg, collaborated with us on our second paper, and worked with me on directivity; the numerous conversations with him helped me understand my research better.

I used several codes and models of Jascha Polet, Jeroen Ritsema, Ji Chen, and Lupei Zhu, and benefited from scientific discussions with them. I would like to acknowledge Patricia for her friendship and for her constant support and encouragement. Jascha, Javier, Bill, Vala, Jane, Hong Kie, Brian, Zhimei, Ozgun and my office mates made life at seismo lab interesting and enjoyable. I would also like to thank Ann, Michele, Viola and Emery for all their help. Parandeh Kia at the international student programs has been a great resource through these years and without her persistent efforts, I would not have been able to obtain a visa to come to Caltech!!

I am grateful to Bhavna and Anil for their support during my initial years at Caltech; to Nandita and Kiran for the many invigorating discussions, and to Ravi, Swami and Suresh for all the fun times together. I would like to thank Prakash, Vidya and Kirana for sharing their music. Ganesh’s friendship and humor kept me in good spirits during my final years at Caltech.

I owe my foray into seismology to the encouragement provided by Dr. J. R. Kayal of the Geological Survey of India. I am grateful to my parents and my brother for encouraging my curiosity and providing a stimulating environment during my years at home, for their love and confidence in my capabilities and for always being there for me. Most of all I am grateful to Jeetu, my husband, for without his patience, love and friendship this thesis would not have seen the light of day.

Abstract

To understand the physics of earthquake rupture mechanics, we have to relate seismologically observable parameters to the dynamics of faulting. One of the key seismological parameters that will help us achieve this objective is the energy radiated by seismic waves. In this work, we develop a new method of estimating radiated energy from regional data using an empirical Green's function method; we also modify existing methods of estimating radiated energy from teleseismic data by improving the corrections applied to the observed seismic data for attenuation and directivity effects.

We compute teleseismic estimates of radiated energy for 23 large subduction zone earthquakes recorded between 1992 and 2001; most of these earthquakes have a magnitude $M_w > 7.5$, but we also include some smaller ($M_w \sim 6.7$) well-studied subduction zone earthquakes and 6 crustal earthquakes. We compile the static stress drop estimates for these 29 earthquakes from published literature. We then determine radiation efficiency of these earthquakes using a stress relaxation model that relates measurable and macroscopic seismological parameters to the physical processes on the fault zone via fracture energy. We also determine the rupture velocity of these earthquakes from published literature. A comparison of radiation efficiencies and rupture velocities of these earthquakes with the expected theoretical values for different modes crack propagation validates the use of the stress relaxation model to understand earthquake rupture mechanics.

From our calculations, we observe that most earthquakes have radiation efficiencies between 0.25 and 1 and are hence efficient in generating seismic waves, but tsunami earthquakes and two deep earthquakes, the 1994 deep earthquake that occurred in

Bolivia and the 1999 Russia-China border earthquake, have very small radiation efficiencies (<0.25) and hence dissipate a large amount of energy on the fault plane. We suggest that the difference in the radiation efficiencies of the different types of earthquakes they could be due to fundamental differences in the rupture mechanics of different events. In case of deep events, the energy is probably dissipated in thermal processes on the fault zone, while it is possible that the morphology of the trench causes branching and bifurcation of rupture resulting in the large energy dissipation during the rupture process of tsunami earthquake.

Table of Contents

List of Figures

List of Tables

CHAPTER 1

Introduction

The recent destructive earthquakes in Izmit, Turkey (August 17, 1999), Chi-chi, Taiwan (September 20, 1999) and Bhuj, India (January 26, 2001) caused an enormous amount of damage to life and property. The swiftness with which an earthquake unleashes its energy and the destruction that is left behind in its wake make earthquakes a hazard for mankind. To reduce the hazard from earthquakes, it is imperative that we understand the physics of the processes that occur during earthquakes. An earthquake happens when the accumulated strain energy in the earth is released suddenly. A part of the energy released, called fracture energy, is used in mechanical processes other than frictional heating on the fault zone as the rupture propagates; a part of the energy, frictional energy, is dissipated as heat on the fault surface and yet another part, wave energy, moves the particles on the fault generating seismic waves that are felt by people and recorded by instruments all over the world. The only part of the energy released in an earthquake that we have direct access to is the wave energy (henceforth referred to as radiated energy).

In an attempt to understand the physics of the rupture process, many recent studies have focused on the determination of spatial and temporal variations of slip, estimation of critical slip, and fracture energy from detailed inversion of seismic wave-forms [e.g., *Boatwright and Cocco*, 1996; *Guatteri and Spudich*, 2000; *Ide and Takeo*, 1997; *Ji et al.*, 2002b; *Pulido and Irikura*, 2000; *Wald and Heaton*, 1994]. An alternative approach would be to estimate the radiated energy, because radiated energy reflects the overall frictional conditions during rupture [e.g., *Kanamori and Heaton*, 2000]. Thus, instead of trying to understand the small-scale complex details of the rupture process, we use the macroscopic parameters–radiated energy, seismic moment, rupture area and rupture velocity to better understand the dynamics of earthquake rupture.

1.1 Energy as a Measure of the Size of an Earthquake

Traditionally, radiated energy has been used as a measure of the size of earthquakes. Early attempts to quantify the size of earthquakes were based on estimating the intensity of damage in earthquakes [*Wood and Neumann*, 1931]. With the advent of instrumental seismology, the size of an earthquake was measured as a function of the amplitude of different seismic waves [*Richter*, 1935]. The idea of using a physical and fundamental quantity to measure the size of the earthquakes led Gutenberg to use radiated energy as a measure of earthquake size [*Gutenberg*, 1942, 1956; *Gutenberg and Richter*, 1956a, 1956b]. Based on the then available seismic data, Gutenberg introduced an empirical scale (the Gutenberg-Richter energy-magnitude relation) that related radiated energy, E_R (in ergs), to surface wave magnitude, M_S, and is given as $\log E_R = 1.5 M_S + 11.8$. However, due to poor seismic data quality and limited computing facilities, estimating radiated energy was difficult; thus, the commonly used measure of earthquake size was based on the amplitude of surface waves (surface wave magnitude).

Subsequently, with the introduction of seismic moment [*Aki*, 1966] the moment magnitude scale came into vogue [*Kanamori*, 1977]. *Kanamori* [1977] determined radiated energy from seismic moment assuming the Orowan condition, i.e., the final stress on the fault, σ_1, is equal to the residual frictional stress on the fault, σ_{f0}, [*Orowan*, 1960], and assuming a constant stress drop of 3 MPa. The calculated radiated energy was then used backward in the Gutenberg-Richter magnitude-energy relationship to determine the moment magnitude scale [*Kanamori*, 1977]; in this scale the magnitude of an earthquake, M_w, is calculated from seismic moment, M_0 (in dyne-cm), using the relation, log M_0=1.5(M_w+10.73). However, in the moment magnitude scale radiated energy was determined from seismic moment. With the advent of broadband seismometers, we can now directly integrate seismic velocity data to determine radiated energy [*Boatwright and Choy*, 1986]; we now have two independent measures of earthquake size, seismic moment and radiated energy, and the relationship between the two can be used to better understand the earthquake source. Thus, radiated energy is not only a measure of the size of the earthquake, but also a macroscopic parameter that can be used to obtain insights into the rupture mechanisms of earthquakes.

1.2 Using Macroscopic Seismic Parameters to Understand Different Types of Earthquakes

To study the differences between earthquakes, it is useful to group earthquakes into different categories depending on the tectonic environments in which they occur. Though this is not an exhaustive list, we can broadly divide earthquakes into the following main categories:

1. Interplate earthquakes: these occur at mature plate boundaries with active continental fault zones (e.g., earthquakes on the San Andreas fault) or at active subduction zones. Faults that host these earthquakes are usually long, well developed and have been active for a long time.
2. Intraplate earthquakes: earthquakes that occur within the subducting slab at depths less than 250 km [*Gutenberg and Richter*, 1938, 1939] and those which occur away from known plate boundaries can be grouped in this category. However, there are several earthquakes that occur in diffuse plate boundaries, e.g., the 1992 Landers earthquake ruptured a set of faults in the Mojave desert

which are part of the diffuse plate boundary between the Pacific plate and the North American plate, and hence such earthquakes cannot be strictly classified as interplate or Intraplate [*Kanamori and Allen*, 1986; *Scholz et al.*, 1986].

3. Deep earthquakes: these occur at depths greater than 500 km [*Gutenberg and Richter*, 1938, 1939] within subducting slabs and are probably the least understood.
4. Tsunami earthquakes: earthquakes that rupture the shallow portions of subduction zones, and generate much larger tsunamis than are expected from their seismic moment magnitude.

This classification of earthquakes includes all the earthquakes studied in this thesis; it does not include several other types of earthquakes. This thesis only considers large earthquakes (M_w>6.5), because the computation of radiated energy of earthquakes requires broadband data with high signal-to-noise ratios. At teleseismic distances, only earthquakes with M_w>7.5 satisfy these criteria; at regional distances, we can estimate radiated energy for smaller events. The focus of this study was to obtain accurate estimates of radiated energy for larger events and to develop and calibrate techniques of estimating radiated energy, so that the methods used here can in future be extended to smaller earthquakes.

It has been observed that earthquakes in the different categories mentioned above have different characteristics. For example, tsunami earthquakes propagate with small rupture velocities and produce mild shaking but are followed by destructive tsunamis [*Kanamori*, 1972; *Polet and Kanamori*, 2000]. The 1994 deep Bolivian earthquake is the largest deep earthquake instrumentally recorded and seems to have propagated very slowly; a large amount of the total energy available for faulting was probably dissipated on the fault zone causing frictional melting on the fault [*Kanamori et al.*, 1998]. These striking differences observed between different earthquakes are probably due to the different physical mechanisms that control the rupture of these earthquakes. Thus, to understand the differences between these earthquakes, it is important that we understand the physics that controls their rupture mechanics.

Over the years, several parameters have been used to characterize the different types of earthquakes. One of the most commonly used parameters is static stress drop, which is defined as the change in the average state of stress on a fault before and after rupture. Several earlier studies noted that intraplate earthquakes had systematically larger static stress drops as compared to interplate earthquakes [e.g., *Molnar and Wyss*, 1972; *Kanamori and Anderson*, 1975; *Scholz et al.*, 1986]. *Kanamori and Allen* [1986] also studied the repeat times of earthquakes and concluded that faults with longer repeat times had higher stress drops. They observed that interplate earthquakes on mature faults occur more frequently than Intraplate earthquakes and hence faults at plate boundaries have larger slip rates. Magnitude-frequency relationships have also been used to understand the differences between different types of earthquakes [e.g., *Frolich*, 1989].

Another parameter that has been used to comprehend the differences between the various types of earthquakes is radiated energy. Several investigators related radiated energy to the static stress drop [e.g., *Savage and Wood*, 1971; *Aki*, 1972]. However, in most of these studies, radiated energy was not estimated directly from seismic waves. Instead, the empirical Gutenberg-Richter energy-magnitude relationship was used to calculate the radiated energy for an earthquake of given magnitude; estimates of radiated energy were also obtained for specific fault geometries using kinematic models (e.g., *Aki* [1972] used the unilateral Haskell model). Additionally, the results from most of these studies were interpreted using kinematic models of the earthquake source in which the displacement history of fault motion is prescribed, a priori, and hence these models, though useful in describing the earthquake source, do not give us any physical insight into the dynamics of the rupture. Some of the more recent studies [*Kikuchi and Fukao*, 1988; *Kikuchi*, 1992] used dynamic models to interpret their results, and though they tried to estimate radiated energy from seismic data, the accuracy of their estimates suffered for want of data with high signal-to-noise.

To understand the physics of earthquake processes, we have to relate the seismologically observable parameters to the *dynamics* of faulting. One of the key seismological parameters that will help us achieve this objective is radiated energy but, as mentioned above, the lack of good quality (broadband, high signal-to-noise ratio) seismic data has resulted in inaccurate estimates of this parameter. In this thesis, we improve direct estimates of radiated energy from seismic waves and use radiated energy with other macroscopic parameters like seismic moment, rupture area and rupture velocity to understand the differences between the rupture mechanics of different earthquakes.

1.3 Objective of the thesis

The primary goal of this thesis is to obtain better estimates of radiated energy and use these estimates along with estimates of other macroscopic seismic parameters to understand the mechanics of earthquakes. Radiated energy, as was mentioned earlier, can be determined from seismic waves, but only recently, with the advent of broadband seismometers, have we been able to estimate this quantity directly from seismic waves

[*Boatwright and Choy*, 1986]. Thus, the use of this parameter to understand earthquakes has not been fully exploited. The first part of this thesis focuses on improving the estimates of radiated energy from regional and teleseismic data. In estimating radiated energy, we have to correct the observed seismic waves for propagation (path) effects such as attenuation, and source effects such as directivity. We develop a new method of estimating radiated energy from regional data using an empirical Green's function method; we also modify existing methods of estimating radiated energy from teleseismic data by improving the corrections applied to the observed seismic data for attenuation and directivity effects.

In the second part of the thesis, we relate the seismologically observed parameters– radiated energy, seismic moment, rupture area and rupture velocity, to the dynamics of faulting. Seismic moment, which is the amplitude of the zero-frequency end (long period end for practical purposes) of the seismic source spectrum, is one of the most well determined seismological parameters; estimates of seismic moment by different investigators seldom differ by more than a factor of two. But rupture area, another important macroscopic parameter, is a poorly determined quantity; estimates of rupture area of the same earthquake often differ by more than a factor of ten. Rupture area is the area over which most of the slip in an earthquake occurs. It is a difficult parameter to estimate because it depends on the distribution of slip on the fault, which can be very heterogeneous. Moreover, the nonunique slip distribution obtained from inversion of seismic data coupled with the different methods used by investigators to estimate the area over which most of the slip is concentrated causes uncertainty in estimates of this parameter. Since rupture area is directly related to static stress drop on the fault, uncertainties in the rupture area introduce uncertainties in the associated static stress drop values.

In this thesis, we compile published static stress drop estimates for several large earthquakes, and when possible give lower and upper bounds of the static stress drop. Using the moment, radiated energy and static stress drop, we try to understand the partitioning of energy in earthquakes using a stress relaxation model. The advantage in using such a model lies in that it is a dynamic model that relates measurable and macroscopic seismological parameters to the physical processes on the fault zone via fracture energy. As will be discussed in Chapter 3, fracture energy can be related to the rupture velocity; thus, we can use this parameter to understand the dynamic propagation of rupture on the fault plane.

An outline of the contents of the thesis is in order. In Chapter 2, we discuss the methods used to determine radiated energy, the problems in estimating radiated energy and how we overcome them. We discuss in detail the uncertainties related to directivity and attenuation corrections and touch upon the other corrections that have already been discussed in greater detail by other investigators. We discuss a new method of estimating radiated energy from regional data using empirical Green's functions and the application of this method to determine radiated energy from the 1999, Hector Mine, California, earthquake. This method overcomes the problems related to inaccurate corrections for propagation path effects because of the use of aftershocks as empirical Green's functions. We also estimate radiated energy for the Hector Mine earthquake from teleseismic data by modifying the conventional methods of estimating teleseismic energy, and compare the regional and teleseismic estimates for this earthquake. We briefly discuss the problems in estimating radiated energy from small earthquakes and conclude the chapter by comparing the regional energy estimates for different earthquakes obtained by different investigators.

A brief introduction to some aspects of fracture mechanics is given in Chapter 3. We discuss two models: the crack model and the frictional sliding model and explain how they can be used to understand the dynamic processes on the fault zone. We then use these concepts to relate a simple stress relaxation model to the partitioning of energy in earthquakes and show how we can use this model and observed seismological parameters to determine radiation efficiency, η_R, which is defined as the ratio of the radiated energy, E_R, to sum of radiated energy and fracture energy, E_G, released in an earthquake, i.e., $\eta_R = E_R/(E_R + E_G)$. Seismic efficiency, η, is defined as the fraction of the total energy released in an earthquake that is available to generate seismic waves, i.e., $\eta = E_R/(E_R + E_G + E_F)$. However, E_F, the energy that is dissipated in frictional heating on the fault zone, cannot be directly determined from seismology; hence, we cannot determine seismic efficiency from seismic waves alone. On the other hand, we can determine radiation efficiency from seismic waves, and use this quantity to understand physical processes on the fault zone. Thus, radiation efficiency, which can be estimated from seismology, gives the *maximum* seismic efficiency of an earthquake. We also discuss how radiated energy and fracture energy can be related to rupture velocity.

In Chapter 4, we compute teleseismic estimates of radiated energy for 23 large subduction zone earthquakes recorded between 1992 and 2001; most of these earthquakes have $M_w > 7.5$, but we also included some smaller well-studied earthquakes. For comparison, we include 6 crustal earthquakes. For these earthquakes, we obtain static stress drops from literature. We briefly describe the methods that are currently used to determine static stress drops and discuss the problems and uncertainties associated with these estimates. We use the estimates of radiated energy, moment and static stress drops to discuss the partitioning of energy in these earthquakes by calculating the radiation efficiency of these earthquakes. Large radiation efficiency would imply that more energy is radiated in seismic waves and less energy is consumed in the fracture process, while small radiation efficiency would imply that most of the energy is dissipated on the fault plane and only a small amount is radiated. We observe that most earthquakes have high radiation efficiencies, but tsunami earthquakes and two deep earthquakes, the 1994 deep earthquake that occurred in Bolivia and the 1999 Russia-China border earthquake, have very small radiation efficiencies. We discuss the possible reasons for this difference in the radiation efficiencies of tsunami earthquakes and the deep Bolivian earthquake and suggest that it could be due to fundamental differences in the rupture mechanics of different events. We conclude by discussing the implications of our results.

Chapter 5 summarizes the main conclusions of the thesis.

CHAPTER 2

Estimating Radiated Energy

Radiated energy is defined as the wave energy that would be transmitted to infinity if an earthquake occurred in an infinite, lossless medium [*Haskell*, 1964].

An earthquake generates seismic waves that travel through the earth and are recorded by seismometers on the surface of the earth. When the seismic waves travel through the earth, the earth structure acts like a filter and modifies the waves. Thus, to calculate radiated energy, we have to correct the recorded seismic waves for propagation path effects like dissipation of energy due to attenuation, site effects and geometric spreading. In addition to correcting the seismic waves for the propagation path effects, another challenging aspect of obtaining accurate estimates of radiated energy lies in determining the corrections for a source effect known as directivity (to be discussed later).

While seismic moment, a well-determined parameter in seismology, depends on the long-period end of the seismic source spectrum, radiated energy is a broadband measure and depends on the entire frequency band. Thus, to determine radiated energy, we require information of the earth structure over the entire frequency band (typically between 0.01 Hz to 1 Hz). Though tremendous progress has been made in the study of the structure of the earth, we still have insufficient information on the structural details that would be important at higher frequencies. Thus, inaccuracies in the corrections applied at higher frequencies could result in uncertainties in energy estimates.

Gutenberg [1942] and *Gutenberg and Richter* [1956a;1956b] related radiated energy (E_R) in ergs to surface wave magnitude (M_S) by the relation: $\log E_R = 1.5 M_S + 11.8$. Earlier studies used this empirical relation to estimate radiated energy [e.g., *Wyss and Brune*, 1971]. Radiated energy has also been estimated from average pulse widths of *P* wave arrivals for deep focus earthquakes [*Vassiliou and Kanamori*, 1982] and from source time functions determined by inversion of seismograms [*Kikuchi and Fukao*, 1988]. With the advent of broadband networks, estimates of radiated energy by direct integration of velocity records improved considerably [*Boatwright and Choy*, 1986; *Boatwright and Fletcher*, 1984; *Choy and Boatwright*, 1995; *Houston*, 1990a; *Houston and Kanamori*, 1990; *Kanamori et al.*, 1993; *Singh and Ordaz*, 1994; *Winslow and Ruff*, 1999].

Despite the increased availability of broadband data, it has been observed that for the same earthquake the estimates of radiated energy from regional data differ from those obtained from teleseismic data by as much as a factor of 10 [*Singh and Ordaz*, 1994]. Additionally, the ratios of the radiated energy to seismic moment, E_R / M_0, for small earthquakes [*Abercrombie*, 1995] are observed to be significantly smaller than those for large earthquakes, leading some authors to suggest drastically different energy release mechanisms for small and large earthquakes [*Kanamori and Heaton*, 2000]. However, the uncertainties in the currently available estimates of radiated energy are large and the differences in the E_R / M_0 ratio between small and large earthquakes may be due to errors in the radiated energy estimates; more tightly constrained estimates are required to understand these differences and to validate the proposed mechanisms.

In this chapter, we discuss our modifications to existing techniques of estimating radiated energy from teleseismic data and a new technique that we used to estimate radiated energy from regional data. First, we discuss the formulae involved in calculating radiated energy from seismic waves. Subsequently, we will discuss the assumptions in the methods we used to estimate radiated energy from seismic waves and the corrections applied to these estimates.

The energy of the seismic wave as it crosses a unit area in unit time is the product of the energy per unit volume, both kinetic and potential, and the wave velocity, c. Thus, if the particle velocity is $\mathrm{v(t)}$, and the density is ρ, the kinetic energy per unit area is $\frac{1}{2}\rho\,\mathrm{c}\int_0^{\mathrm{t}}\mathrm{v}^2(\mathrm{t})\,dt$. Since the potential energy is on an average equal to the kinetic energy [*Bath*, 1966] the wave energy crossing a unit area is $\rho\,\mathrm{c}\int_0^{\mathrm{t}}\mathrm{v}^2(\mathrm{t})\,dt$. Hence, the radiated energy of seismic waves can be given as: $E_R = \rho\,\mathrm{c}\int_{\mathrm{s}}\int_0^{\mathrm{t}}\mathrm{v}^2(\mathrm{t})\,dt\,dS$ where S is the surface area of integration. Stating this more formally, to obtain estimates of radiated energy, we integrate the squared velocity records over time [e.g., *Haskell*, 1964] over a homogeneous spherical surface around the source:

$$E_R = \int_{-\infty}^{\infty}\int_S \rho[\alpha\,\dot{u}_\alpha{}^2 + \beta\,\dot{u}_\beta{}^2]\,dS\,dt\,, \qquad \mathbf{(2.1)}$$

where ρ is the density at the source, α and β are the *P* and *S* wave velocities at the source, $\dot{u}_\alpha(t)$ and $\dot{u}_\beta(t)$ are the far-field *P* and *S* wave velocity records respectively and S is the surface area of the spherical surface of integration. The far-field displacement functions for the *P* and *S* waves, $u_\alpha(t)$ and $u_\beta(t)$, are given as shown below:

$$u_\alpha(t) = \frac{R_\alpha(\theta,\phi)}{4\pi r}\frac{\beta^2}{\alpha^3}\int_s \dot{D}(\vec{\xi}, t - r/\alpha)\, ds \tag{2.2}$$

$$u_\beta(t) = \frac{R_\beta(\theta,\phi)}{4\pi r}\frac{1}{\beta}\int_s \dot{D}(\vec{\xi}, t - r/\beta)\, ds\ , \tag{2.3}$$

where s is the rupture area, $\dot{D}(\vec{\xi}, t - r/\alpha)$ is the source time function (also known as the far-field slip rate function) at distance r from the source, and r is a function of the location of slip on the fault, $\vec{\xi}$, and the position of the observation point given by θ and ϕ . For a propagating rupture, the source time function is different at different stations, an effect that is called directivity. $R_\alpha(\theta,\varphi)$ and $R_\beta(\theta,\phi)$ are *P* and *S* wave radiation pattern factors respectively, where

$$R_\alpha(\theta,\phi) = \sin^2(\theta)\sin(2\phi) \tag{2.4}$$

and $R_\beta(\theta,\phi)$ is given for the *SH* and *SV* waves as:

$$\begin{aligned} R_{SH}(\theta,\phi) &= \frac{1}{2}\sin(2\theta)\sin(2\phi) \\ R_{SV}(\theta,\phi) &= \sin(\theta)\cos(2\phi) \end{aligned} \tag{2.5}$$

These are the radiation pattern coefficients for a point double couple, where the co-ordinate axes are fixed to the double couple. If we consider the X, Y, and Z axes where the Z-axis is vertical upwards and the X-axis is along the strike of the fault, θ is the take-off angle measured clockwise from the Z-axis in the vertical plane and ϕ is the station azimuth measured counter-clockwise from the X-axis on the horizontal plane.

In computing radiated energy from observed velocity records, we backproject the *P* and *S* waves to the source and integrate the squared velocity records over the focal sphere. Since the earthquake source is completely described by the *P* and *S* waves and surface waves are only a combination of these body waves, by calculating the radiated energy from the direct *P* and *S* arrivals, we account for the total energy radiated by the earthquake.

Actual total radiated energy

The actual total radiated energy for an earthquake can be determined using equation (2.1) along with equations (2.2) and (2.3). Thus, the actual total energy, E_R, is the sum of the *P* wave energy, E_α and *S* wave energy, E_β and is given as

$$E_R = E_\alpha + E_\beta \, ,$$

where

$$E_\alpha = \int_{-\infty}^{\infty}\int_S \rho\alpha \left[\left(\frac{R_\alpha(\theta,\phi)}{4\pi r} \frac{\beta^2}{\alpha^3} \right) \int_s \ddot{D}(\vec{\xi}, t - r/\alpha)\, ds \right]^2 dSdt$$

$$E_\beta = \int_{-\infty}^{\infty}\int_S \rho\beta \left[\left(\frac{R_\beta(\theta,\phi)}{4\pi r} \frac{1}{\beta} \right) \int_s \ddot{D}(\vec{\xi}, t - r/\beta)\, ds \right]^2 dSdt$$

Single-station method

Ideally, we would like to determine the radiated energy flux due to a finite source at every point on the earth using the above equations, correct the flux for attenuation and geometric spreading, and then sum the flux over all the points to obtain the total radiated energy. In practice, since we have seismic stations only at certain locations on the earth, we can determine the radiated energy flux only at these locations. Consequently, to account for the total energy from the seismic waves recorded at these stations, we use a method that we refer to as the single-station method to estimate radiated energy.

In the single-station method, we assume that the earthquake source is a point source. For a point source, the source time functions in equations (2.2) and (2.3) will become independent of station location, i.e., the source time functions are not functions of θ and ϕ. Thus, we can rewrite $u_\alpha(t)$ and $u_\beta(t)$ from equations (2.3) and (2.4) as

$$u_\alpha(t) = \frac{R_\alpha(\theta,\phi)}{4\pi\rho\, r\alpha^3}\dot{M}(t) \tag{2.6}$$

$$u_\beta(t) = \frac{R_\beta(\theta,\phi)}{4\pi\rho\, r\beta^3}\dot{M}(t)\,, \tag{2.7}$$

where the moment rate function, $\dot{M}(t) = \rho\beta^2 \iint_s \dot{D}(t)ds$, is now exactly the same at all stations. Substituting (2.4) into (2.6) and then into (2.1), for the *P* wave energy, we have

$$\begin{aligned} E_\alpha &= \int_{-\infty}^{\infty} dt \int_S \rho\alpha \left(\frac{R_\alpha(\theta,\phi)}{4\pi\rho\alpha^3 r}\ddot{M}(t) \right)^2 dS \\ &= \frac{1}{16\pi^2\rho\alpha^5}\int_0^{\infty}\ddot{M}^2(t)dt \int_\phi\int_\theta \frac{R_\alpha(\theta,\phi)}{r^2} r^2 \sin(\theta)d\theta d\phi \\ &= \frac{\overline{R}_\alpha^2}{4\pi\rho\alpha^5}\int_{-\infty}^{\infty}\ddot{M}^2(t)dt, \end{aligned} \tag{2.8}$$

where $\overline{R}_\alpha^2$ is the average radiation pattern coefficient for *P* waves and is given by

$$\overline{R}_\alpha^2 = \frac{1}{4\pi}\int_0^{\pi}\int_0^{2\pi} R_\alpha^2(\theta,\phi)\sin(\theta)\,d\theta\,d\phi = \frac{4}{15} \tag{2.9}$$

Similarly, for the *S* waves we can write

$$E_\beta = \frac{\overline{R}_\beta^2}{4\pi\rho\beta^5}\int_{-\infty}^{\infty}\ddot{M}^2(t)dt\,, \tag{2.10}$$

where $\overline{R}_\beta^2$ is the average radiation pattern coefficient for *S* waves and is given by

$$\overline{R}_\beta^2 = \frac{1}{4\pi}\int_0^{\pi}\int_0^{2\pi} (R_{SH}^2(\theta,\phi) + R_{SV}^2(\theta,\phi))\sin(\theta)\,d\theta\,d\phi = \frac{2}{5} \tag{2.11}$$

Thus, we can write the total radiated energy as

$$E_R = E_\alpha + E_\beta = \frac{1}{15\pi\rho\alpha^5}\int_{-\infty}^{\infty}\ddot{M}^2(t)dt + \frac{1}{10\pi\rho\beta^5}\int_{-\infty}^{\infty}\ddot{M}^2(t)dt \tag{2.12}$$

Using Parseval's theorem, $\frac{1}{2\pi}\int_{-\infty}^{\infty}|\hat{g}(\omega)|^2\,d\omega=\int_{-\infty}^{\infty}|g(t)|^2\,dt$, we can write the energy in the frequency domain as follows

$$E_R=\left[\frac{1}{15\pi^2\rho\alpha^5}+\frac{1}{10\pi^2\rho\beta^5}\right]\int_0^{\infty}\omega^2\,|\hat{\dot{M}}(\omega)|^2\,d\omega \qquad \textbf{(2.13)}$$

where $\hat{\dot{M}}(\omega)$ is the moment rate spectrum and the hat(^) is used to denote a quantity in the frequency domain (since $\hat{\ddot{M}}(\omega)=\omega\,\hat{\dot{M}}(\omega)$). We can also write the radiated energy as

$$E_R=\left[\frac{8\pi}{15\rho\alpha^5}+\frac{8\pi}{10\rho\beta^5}\right]\int_0^{\infty}f^2\,|\hat{\dot{M}}(f)|^2\,df \qquad \textbf{(2.14)}$$

where $\omega=2\pi f$, and f is the frequency in Hz.

As the contribution from the *P* waves is less than 5%, it is usually negligible. However, in teleseismic estimates, we have to use *P* wave data to calculate the energy. *S* waves are attenuated about 4 times as much as the *P* waves as they travel through the earth; hence, at teleseismic distances *S* waves have little energy at frequencies above 0.5 Hz and cannot be used to determine accurate estimates of energy.

Thus, in the single-station method, we assume a point source and calculate the radiated energy at every station. The radiated energy of the earthquake is equal to the average of the single-station estimates.

2.1 Corrections Applied to the Observed Data

In estimating the radiated energy from an earthquake source, we would like to determine the seismic waveform as it would be if the source were in an infinite homogenous medium. Thus, we try to reduce the data to a focal sphere enclosing a homogeneous, non-dissipative medium around the source (Figure 2.1).

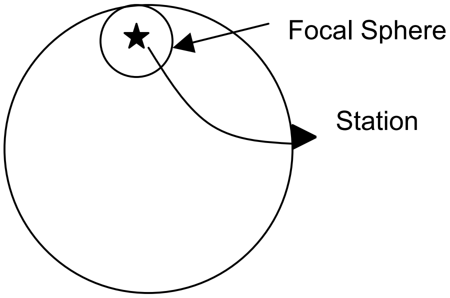

Figure 2.1 Diagram to depict the passage of seismic waves from the source (star) to the receiver (triangle); to compute energy we would like to correct for the effects of the propagation path and calculate the total energy that would be transmitted if the source were in a homogeneous non-dissipative medium.

To compute the radiated energy from data using the single-station method, we have to determine the moment rate spectrum, $\hat{\dot{M}}(f)$, and then use equation (2.13) to calculate the radiated energy. But we have to first determine the moment rate spectrum from the observed displacement spectrum. At teleseismic distances, the displacement spectrum at each station can be given as

$$|\hat{u}(f)| = \frac{R(\theta,\phi)}{4\pi\rho^3 \mathrm{v}^3_{\alpha,\beta}} \frac{C\, g(\Delta)\, |\hat{I}(f)|}{R_E} e^{(-\pi f t^*)}\, |\hat{\dot{M}}(f)|, \qquad \textbf{(2.15)}$$

where at teleseismic distances the geometric spreading factor $1/r$ is replaced by $g(\Delta)/R_E$, R_E = 6371 km is the radius of the earth, $\mathrm{v}_{\alpha,\beta}$ is the *P* wave or *S* wave velocity, t^* is the attenuation factor (equal to the travel time divided by the path-averaged attenuation, Q, see section 2.1.2), C is the free surface receiver effect, and $\hat{I}(f)$ is the instrument response. Equation (2.15) is the frequency domain equivalent of equations (2.6) and (2.7); additionally, it includes the free surface receiver effect, the geometric spreading factor for teleseismic distances, the instrument response, and the attenuation factor for wave propagation through the earth. From the displacement spectrum, $\hat{u}(f)$, we can determine the moment rate spectrum, $\hat{\dot{M}}(f)$,

$$|\hat{\dot{M}}(f)| = \frac{4\pi\rho^{3}\mathrm{v}_{\alpha,\beta}^{3} R_{E} e^{(\pi f t^{*})} \, |\hat{u}(f)|}{g(\Delta) R(\theta,\phi) \, C \, |\hat{I}(f)|} \qquad \textbf{(2.16)}$$

Thus, by correcting the observed displacement spectrum for geometric spreading, radiation pattern factor and attenuation, we can determine the moment rate spectrum as shown in equation (2.16). By applying these corrections, we can account for the source mechanism and propagation path of the seismic waves; and once the moment rate spectrum is determined, the radiated energy can be determined by using the single-station method.

In practice, we determine the moment rate spectrum, $\hat{\dot{M}}(f)$, at each station and then determine the single-station estimates of radiated energy at all the available stations. If an earthquake can be described by a point source, this method would give exactly the same estimate of radiated energy at all the stations. However, all faults are finite and the assumption of a point source is not accurate; thus, the individual stations will have different single-station energy estimates. By taking an average of these estimates, we try to average out the directivity (source finiteness) effect. But, even for a large number of stations with a good azimuthal coverage, an average of the single-station estimates is not equal to the actual radiated energy of an earthquake. Thus, we have to correct the average single-station estimate of radiated energy for the directivity effect.

In the following sections, we will discuss the various corrections applied to the data, i.e., we will discuss the directivity correction for source finiteness, and the corrections for attenuation, source structure and scattering. We will also discuss the importance of these corrections, and the uncertainties in the energy estimates due to inadequate corrections.

2.1.1 Directivity

The single-station estimate of radiated energy should be exactly the same at all stations for a point source. When the source is finite, however, the rupture propagates along the fault and breaks different parts of the fault at different times. Thus, for finite faults, akin to the Doppler effect, the seismic energy is focused in the direction of rupture propagation, an effect that is called directivity. Consequently, each station receives a different amount of energy, and the single-station estimates of energy change with station location; as mentioned earlier, an average of these single-station estimates is not equal to the actual total energy radiated by the earthquake. Thus, we have to correct the average of the single-station estimates for directivity.

To evaluate the effect of directivity on energy estimates, we compute the seismic energy radiated by a theoretical Haskell source [*Haskell*, 1964]. First, we consider a longitudinal shear fault in which the rupture propagates along the slip direction, and the final displacement along the length of the fault is constant; we will refer to this model as a unilateral strike-slip model (strike=0^0, dip=90^0 and rake=0^0). For a unilateral strike-slip model with a fault of length L=70 km, width W=15km, a slip function which is a ramp function with a rise time of 2.4s, maximum slip=3.2m, and rupture velocity=0.9 times shear wave velocity, with the rupture propagating along strike to the north (at an azimuth of 0^0), we compute the single-station energy estimates using equation (2.13) for different azimuths and take-off angles, and the energy flux at the same azimuths and take-off angles using equation (2.1) for a particular θ and ϕ. These estimates of energy flux are multiplied with the area of the focal sphere over which the energy is calculated, so that we can compare these estimates of actual energy at a station to the single-station estimates of energy at the same stations.

The focal sphere is divided into regions of equal area; we use about 50 values of θ (take-off angle) where θ varies from 0^0 to 180^0 and 50 values of ϕ (azimuth) at the equator; ϕ varies from 0^0 to 360^0. For the unilateral strike-slip model described above, Figure 2.2(a) shows the single-station energy estimates (red pluses) and the actual energy (blue squares) as a function of azimuth; for each azimuth we compute the energy estimates at a range of take-off angles. Thus, each line represents the variation in energy estimates with azimuth for a particular take-off angle. All the computations are done using the analytical solution for radiated energy given by *Haskell*, 1964. Since the rupture is propagating to the north, the radiated energy is focused towards this azimuth, and the radiated energy is minimal at stations away from the rupture direction (i.e., stations at an azimuth of 180^0). For a point source, the single-station energy estimates will be exactly the same at all stations; however, the finiteness of the source introduces strong directivity effects, and the resulting differences in the single-station energy estimates at different stations are quite pronounced.

For the same azimuth and take-off angle, the single-station estimate (red) is not equal to the actual energy at the station (blue) because in computing the single-station estimates we use the average radiation pattern factor (equation 2.12), whereas to compute the actual energy estimates at a station we use the radiation pattern at the station. Thus, the actual energy at stations includes both the directivity effect and the radiation pattern effect, while the single-station estimates show the effect of directivity only. We also observe that the average energy obtained from the single-station method is not exactly equal to the actual total radiated energy (which is equal to sum of the actual energy over all the points divided by the number of points). Thus, even if the station coverage is good, in the presence of strong directivity effects, we cannot recover the actual total radiated energy from the single-station method. In the case considered in Figure 2.2(a), the ratio:

Actual total energy/ Average single-station estimate = 1.53

To study the effects of fault length on directivity, we modified the length of the fault from L=80 km to L=110 km, keeping all other parameters the same. For the Haskell model, the actual total energy and the average energy from single-station estimates do not depend on fault length (as long as the smallest duration of the source time function is larger than the rise time; i.e., $L(1/V_r - 1/\beta)$ > rise time). Thus, directivity, a factor that is thought to be more important for longer faults, is independent of fault length in the Haskell model (within the limitations pointed out). This is because, in these models, energy is radiated only at the edges of the fault, i.e., at the beginning and end of rupture.

(a) Unilateral strike-slip

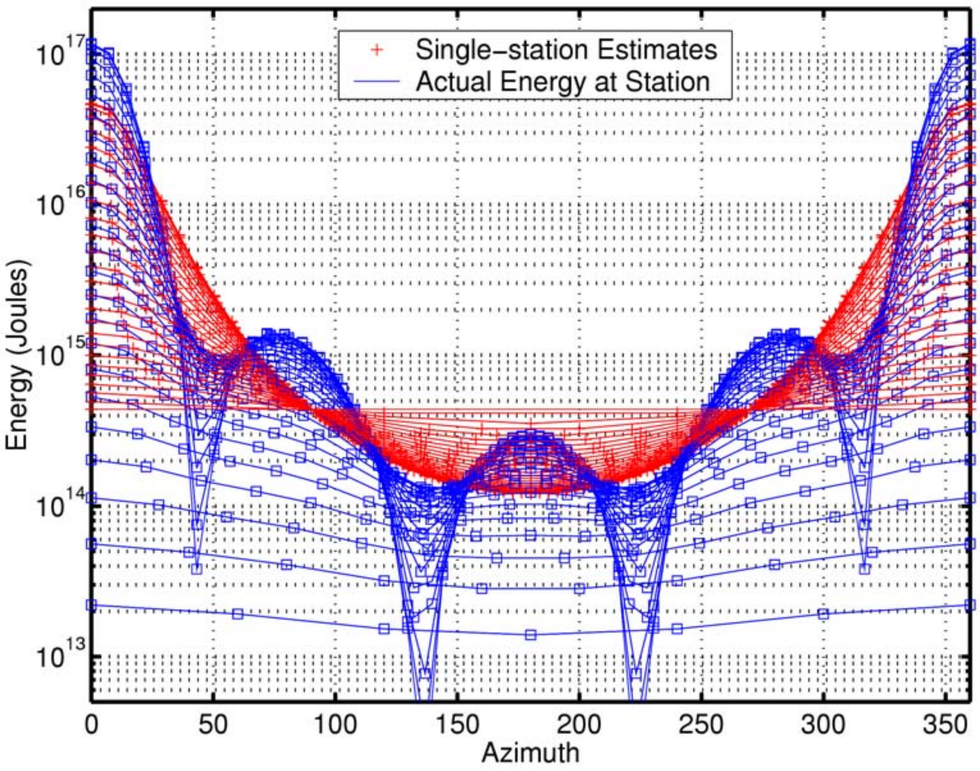

Bilateral strike-slip

(b)

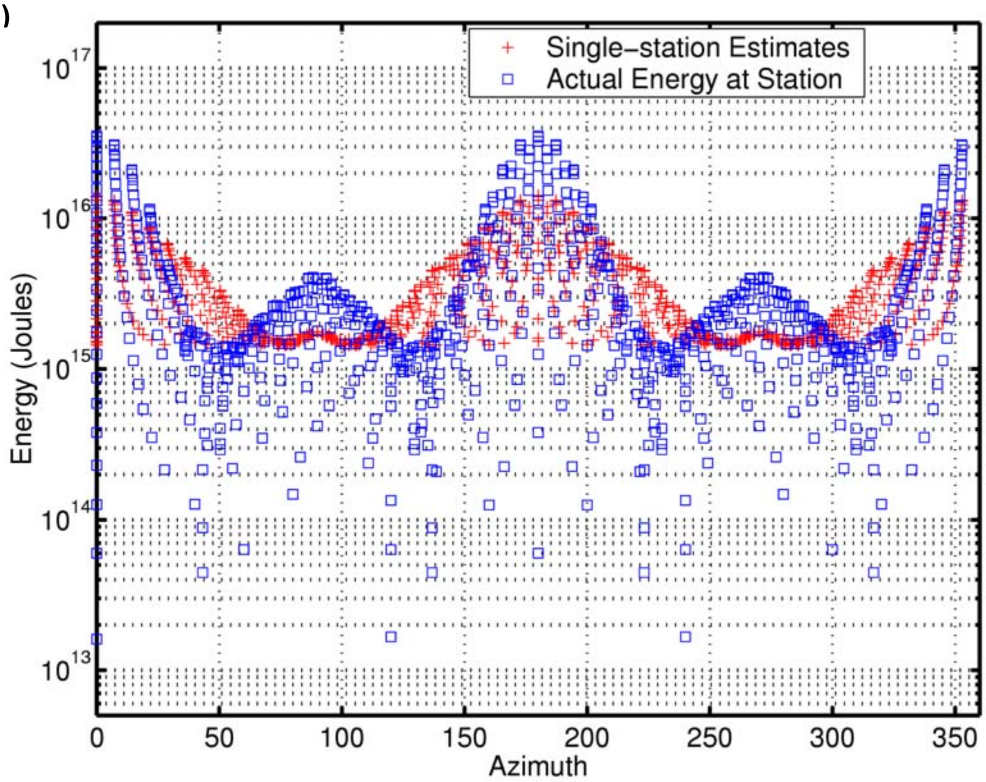

(c)

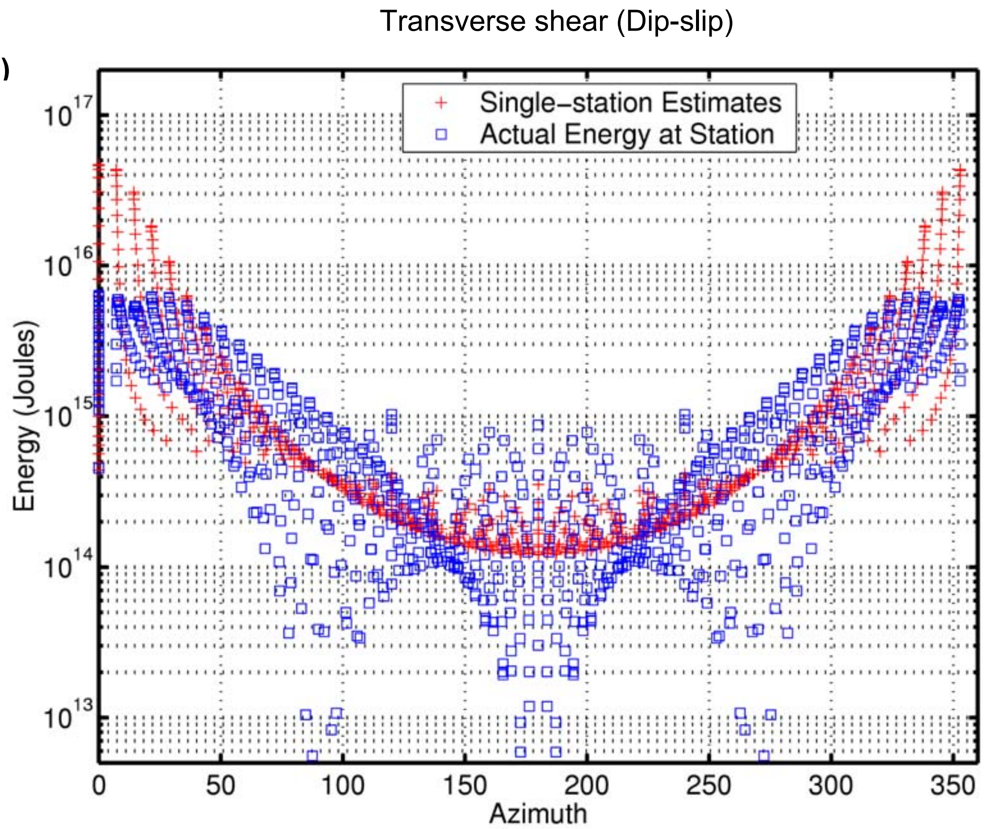

Figure 2.2 (a) Unilateral strike-slip model with rupture propagating north: the blue squares represent the actual energy calculated for different azimuths and take-off angles, whereas the red plus signs represent the single-station energy estimates obtained by using equation (2.12). The azimuthal distribution of the actual energy is a product of the radiation pattern factor (the lobes) and the directivity factor (the curve with maximum in the direction of rupture propagation, i.e., maximum at 0^0), whereas the single-station energy estimates are not a function of radiation pattern; the lines in the plot show the variation in the energy estimates with azimuth for a particular take-off angle. **(b)** Bilateral strike-slip model with the rupture starting at the center and propagating to the north and south. **(c)** Transverse shear model with rupture propagating along strike (to the north). For the bilateral and transverse shear cases, we do not draw lines as this makes the figure too complicated.

We also developed an analytical solution for the energy radiated by a bilateral rupture model and used it to compute the single-station estimates and the actual energy at different stations. Shown in Figure 2.2(b) is an example for a bilateral strike-slip fault of total length L=40 km (all other parameters are the same as those used for the unilateral strike-slip model); the rupture propagates from the center of the fault to the north (azimuth=0^0) and south (azimuth=180^0). From the figure, we observe that the effect of directivity is less pronounced in the case of bilateral rupture. In the case considered in Figure 2.2(b), the ratio:

Actual total energy/ Average single-station estimate = 1.21

The third case plotted in Figure 2.2(c) shows transverse shear faulting (strike=0^0, dip=90^0 and rake=90^0) on a fault of length = 70 km with rupture propagating along strike to the north and all other parameters the same as before. In this case, the average of the single-station estimates is larger than the actual total energy and thus the ratio:

Actual total energy/ Average single-station estimate = 0.51

For these three cases, we also computed the single-station energy estimates for regional (take-off angles close to horizontal) and teleseismic (take-off angles close to vertical) distribution of stations and compared the regional and teleseismic average single-station estimates with the actual total energy. Directivity effects cause regional single-station estimates of energy to be overestimated by a factor of 1.2 to 5 and the teleseismic single-station energy estimates to be underestimated by a factor of 3 to 10. The problem is most severe for teleseismic estimates from unilateral strike-slip faults because in the case of vertical strike-slip faults with rupture propagating along strike (azimuth of 0^0 in the case considered), directivity causes the energy to be focused along the direction of rupture propagation. Additionally, the *S* wave radiation pattern factor is also large in this direction, and due to the combined effect of these two factors, the radiated energy in strike-slip earthquakes is strongly focused in the direction of rupture propagation and very little energy is received at stations away from the direction of rupture propagation. Thus, the actual energy estimates (shown by blue squares in Figure 2.2(a)) at stations in the direction of rupture propagation are larger than would be expected if only directivity is considered (single-station estimates shown as red pluses). For the unilateral strike-slip model considered above, at teleseismic distances, the actual total energy is a factor could be a factor of 10 larger than the average of the single-station estimates. Hence, directivity corrections for teleseismic estimates of energy from unilateral strike-slip faults are very important; moreover, it is essential to have a good azimuthal coverage of stations because if there are no stations at azimuths close to the direction of rupture, the energy estimates will be severely underestimated.

On the other hand, in transverse shear faulting (vertical dip-slip) with the rupture propagating along strike (azimuth of 0^0 in the case considered), directivity would cause a focusing of the energy in the rupture direction; however, the *S* wave radiation pattern factor at take-off angles close to horizontal (i.e., regional distances) is small in this direction. Hence, the actual energy (shown by the blue squares in Figure 2.2(c)) at these stations is not as large as would be expected if only directivity is considered (single-station estimates shown as red pluses). For the case considered, the actual total energy is about a factor of 5 smaller than the average of the regional single-station energy estimates.

Thus, directivity corrections are important when computing teleseismic single-station estimates for vertical strike-slip faults with the rupture propagating along strike, and for regional single-station estimates for vertical dip-slip faults with rupture propagating along strike. However, the models considered so far are simple kinematic models, and though they are useful in understanding the effects of directivity on radiated energy estimates, it is important to study the more complex models of real earthquakes. Consequently, we studied the effects of directivity on radiated energy estimates by using slip models that were determined from inversion of seismic data. We used the rupture model of *Dreger*

[1994] for the 1992 Landers earthquake, the rupture model obtained by *Ji et al.* [2002b] for the 1999 Hector Mine earthquake and the rupture model of *Ji et al.* [2002] for the Taiwan earthquake. For each of these earthquakes, we calculated the single-station estimates as well as the actual energy estimates from the slip models. The following computations were done using a simple algorithm where we divide the focal sphere into surfaces of equal area and use equation 2.1 to calculate the single-station energy flux and the actual total radiated energy for a given slip model. Since the gridding of the focal sphere is simple, there are numerical errors in our solutions; more sophisticated finite-element or finite-difference algorithms would be required to reduce these numerical errors. However, as explained later, the numerical errors do not significantly affect our energy estimates.

The Landers earthquake was a strike-slip earthquake; the rupture was mostly unidirectional and propagated along strike (azimuth~340^0). We used the slip model of *Dreger* [1994] to calculate the single-station energy estimates and the actual energy over a range of azimuths and take-off angles. From Figure 2.3(a), we observe that most of the energy is focused along the fault strike, similar to the unilateral strike-slip model of Figure 2.2(a), but the energy distribution is more complicated than the simple unidirectional Haskell model. The large single-station energy estimates at about 80^0 and 180^0 are due to numerical errors because at these stations the radiation pattern factor becomes very small (nodal stations). Later, when we compare the model energy estimates with the energy estimates from data, we do not use these nodal stations (stations at which the radiation pattern factor is smaller than 0.2) so as to avoid these problems.

(a)

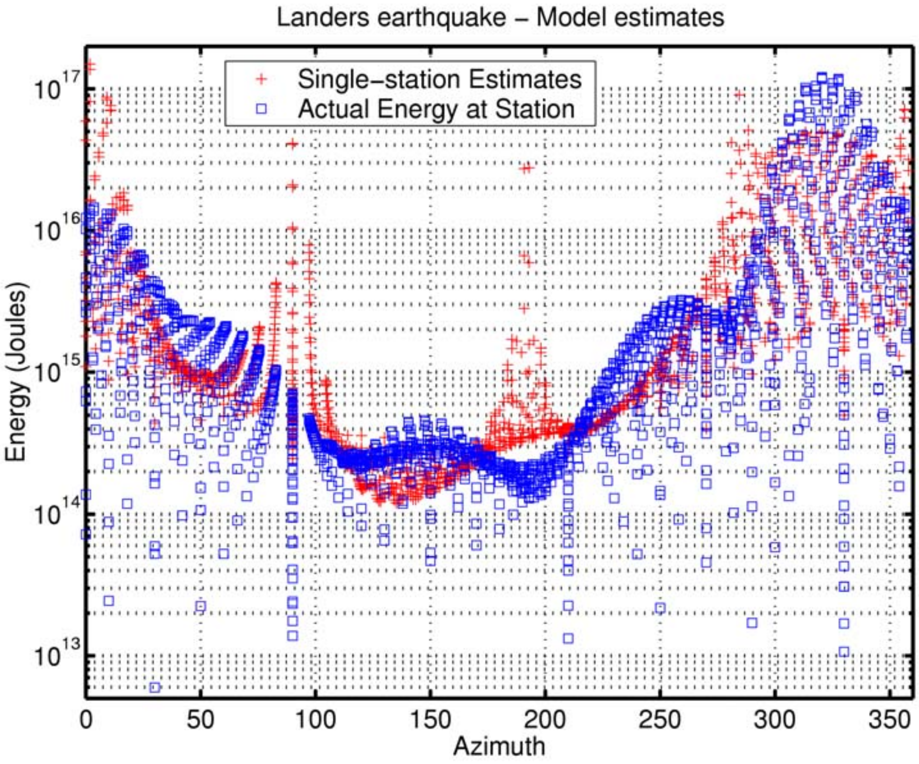
Landers earthquake - Model estimates
Single-station Estimates
Actual Energy at Station
Energy (Joules)
10^{17}
10^{16}
10^{15}
10^{14}
10^{13}
Azimuth
0
50
100
150
200
250
300
350

(b)

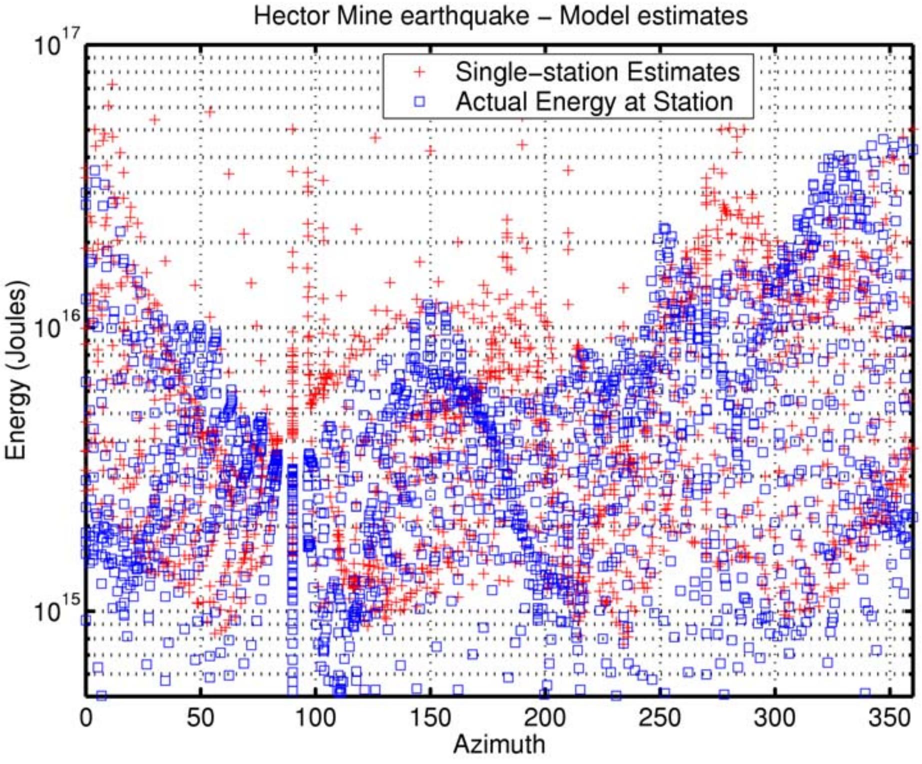
Hector Mine earthquake - Model estimates
Single-station Estimates
Actual Energy at Station
Energy (Joules)
10^{17}
10^{16}
10^{15}
Azimuth
0
50
100
150
200
250
300
350

(c)

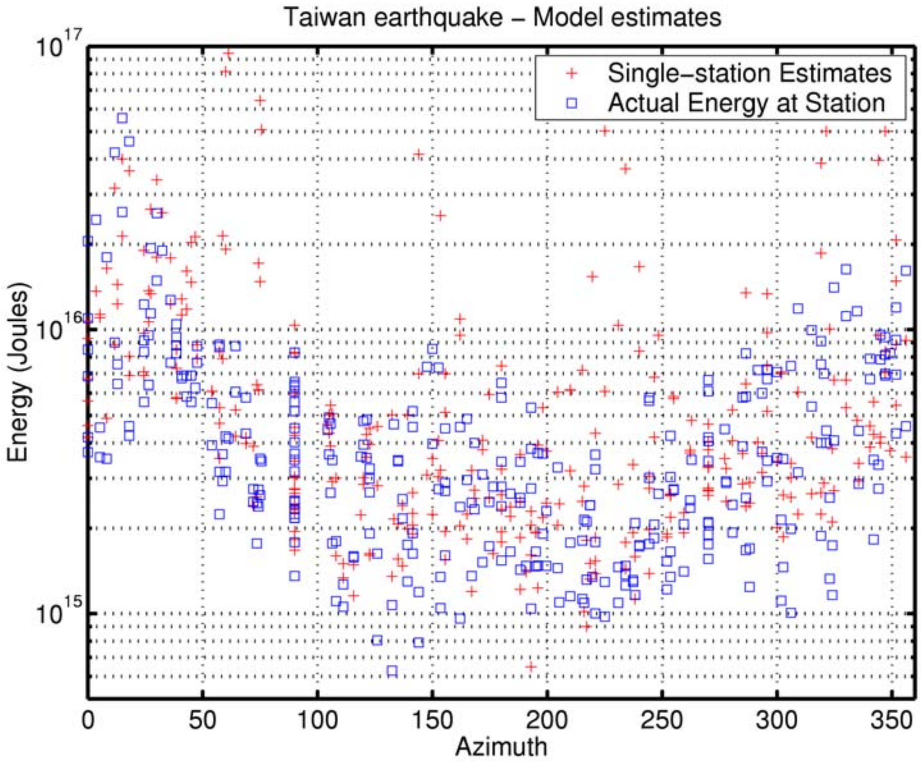

Figure 2.3 (a) Landers earthquake: radiated energy estimates from the slip model of Dreger et al. [1994]; the blue squares represent the actual energy calculated for different azimuths and take-off angles, whereas the red plus signs represent the single-station energy estimates. **(b)** Hector Mine earthquake: radiated energy estimates from the slip model of Ji et al. [2002b]. **(c)** Taiwan earthquake: radiated energy estimates from the slip model of Ji et al. [2002].

Shown in Figure 2.3(b) are the radiated energy estimates for the Hector Mine earthquake determined using the model of *Ji et al.* [2002b]. The Hector Mine earthquake was essentially a bilateral rupture with a fault about 40 km long [*Ji et al.*, 2002b; *Trieman et al.*, 2001]. However, the rupture broke three fault segments and has a complicated slip history [*Ji et al.*, 2002b] probably far more complex than the Landers earthquake. Thus, as seen in Figure 2.3(b), the variation of the single-station estimates as well as the actual energy at stations is quite complicated as compared to the bilateral Haskell model of Figure 2.2(b).

A similar computation for the Taiwan earthquake of September 20, 1999, using the model of *Ji et al.* [2002] is shown in Figure 2.3(c). The Taiwan earthquake was a thrust earthquake with a complicated slip distribution. The earthquake ruptured from south to north along strike (~20^0) and also downdip. But the Taiwan earthquake ruptured a fault with a dip of 30^0, and for this focal mechanism, stations at azimuths close to 180^0 are near the *S* wave node. Thus, the actual energy (blue squares in Figure 2.3(c)) at the stations at these azimuths is small, but since the directivity is away from this azimuth, the single-station estimates of energy (red pluses) are also small at these azimuths. Thus, in the three earthquake models mentioned the slip distribution is more complicated than in the simple kinematic models considered earlier. Variations of fault strike, rake direction, amount of slip and direction of rupture as the rupture propagates along the fault cause additional complications that are captured in the earthquake models.

In the discussion above, we determined estimates of energy from slip models and compared the actual energy at a station to the single-station energy estimate at the same station. Now, we would like to compare the model energy estimates to energy estimates from data. Since we can only determine single-station estimates of energy from the data (i.e., we cannot determine actual total energy from the data due to the limited number of stations), we compare these single-station estimates determined from data to the single-station estimates determined from the slip models and then describe the method we use to correct the directivity effects in the data.

First, we compare the single-station estimates obtained from the slip models to the single-station estimates obtained from data for the Hector Mine and Taiwan earthquakes. Figure 2.4(a) and (b) show the single-station energy estimates obtained at different stations from regional and teleseismic data (details of the method in section 2.2) and the single-station estimates at the same station obtained using the slip model [*Ji et al.*, 2002b] for the Hector Mine earthquake. From the figure, we observe that there are differences between the energy estimates predicted by the model and those determined from data. These differences arise due to the following reasons: the synthetics created by the model do not exactly predict the data at frequencies larger than 0.5 Hz; the model is nonunique and may not be completely representative of the actual slip distribution especially because the Green's functions at higher frequencies are not well determined; the estimation of energy from data may have inaccuracies (though we think this is minimal); and finally, there are numerical errors in the calculation of energy for a given model. Though the energy estimated from the model is significantly different from the energy estimated from data at some stations, the average of the single-station estimates from the model and regional data are almost the same, and the average of the single-station estimates from the model and teleseismic data differ by a factor less than two.

Figure 2.4(c) shows a comparison between single-station estimates for the Taiwan earthquake from the model of Ji et al. [2002] and from teleseismic data. It can be observed from Figure 2.4 that directivity effects can cause significant azimuthal variation in the energy estimates even at teleseismic distances. Thus, in Figure 2.4(c), we observe that the single-station estimates of energy at teleseismic stations can vary by a factor of ten between stations. Hence, it is important to have a good azimuthal distribution of stations, so that the average of the single-station estimates yields in a realistic estimate of the energy of the earthquake. With the azimuthal coverage of stations used (shown in Chapter 4), the average of the single-station estimates from the model and teleseismic data differ by a factor less than two.

(a)

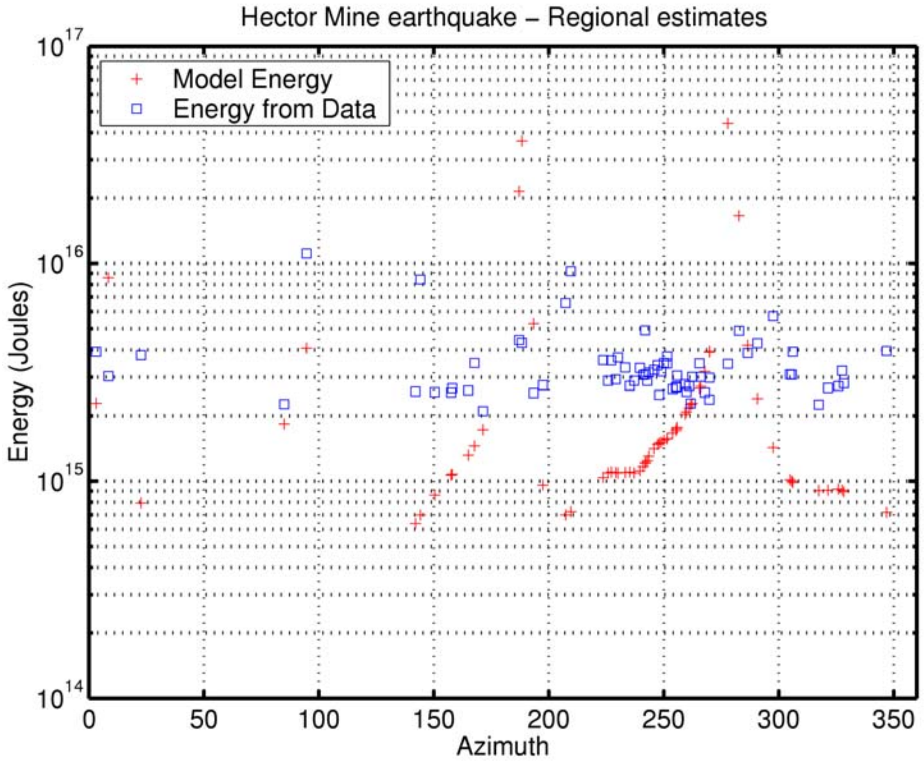
Hector Mine earthquake – Regional estimates
Model Energy
Energy from Data
Energy (Joules)
10^{17}
10^{16}
10^{15}
10^{14}
Azimuth
0
50
100
150
200
250
300
350

(b)

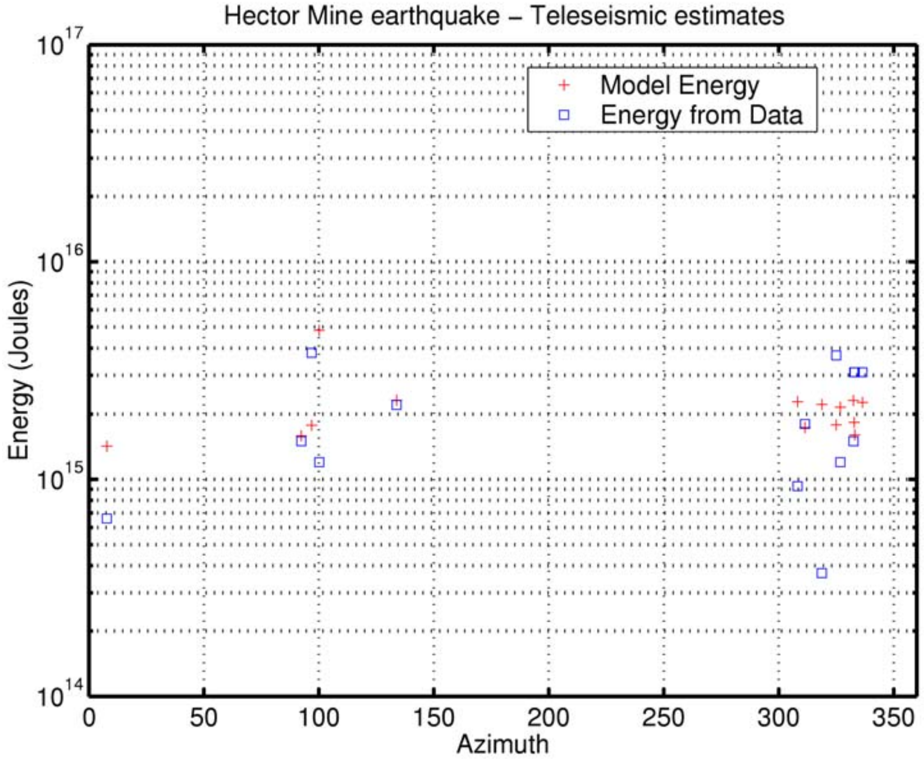
Hector Mine earthquake – Teleseismic estimates
Model Energy
Energy from Data
Energy (Joules)
10^{17}
10^{16}
10^{15}
10^{14}
Azimuth
0
50
100
150
200
250
300
350

(c)

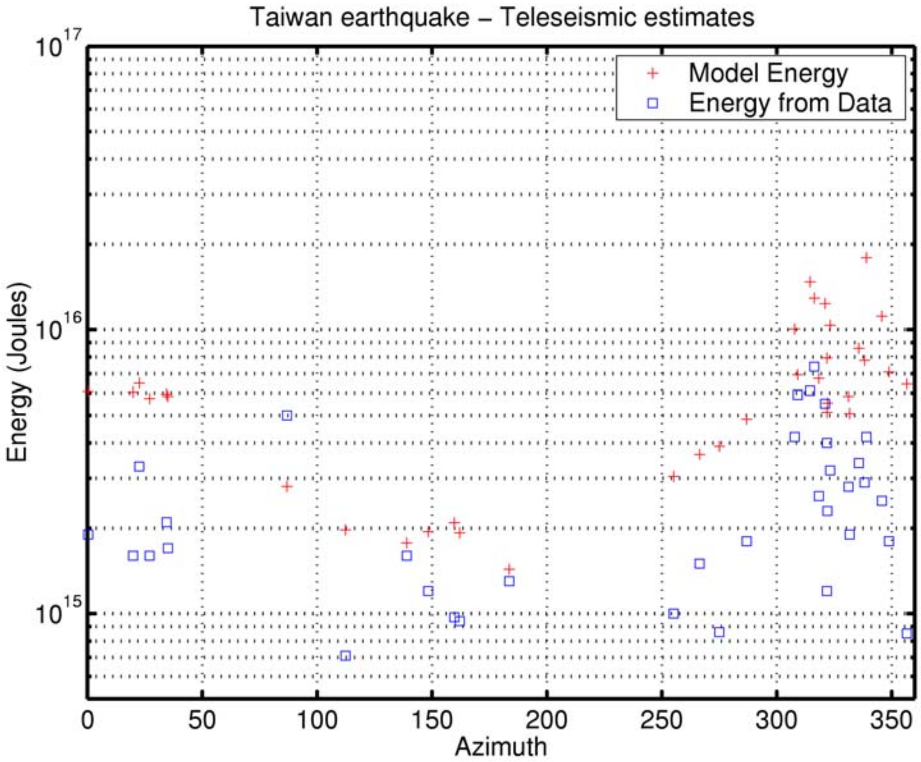

Figure 2.4 Single-station estimates of energy from models (red plus) and from data (blue squares) **(a)** Hector Mine earthquake for regional stations; **(b)** Hector Mine earthquake, teleseismic stations–model of slip distribution used to calculate model energy for Hector Mine earthquake was obtained from Ji et al. [2002b]; **(c)** Taiwan earthquake–model of slip distribution used to calculate model energy obtained from Ji et al. [2002].

To obtain accurate estimates of energy, we have to determine a correction for directivity. From the above discussion, it can be seen that the effect of directivity on radiated energy estimates depends on the slip model and station distribution. We can determine the single-station estimate from data at a particular station, and also determine the single-station estimate from a slip model at the same station. Thus, for a particular distribution of stations, we can compute the average of the single-station estimates from the slip model and the average of the single-station estimates from data. We can also compute the actual total radiated energy of the earthquake for this slip model. The ratio of the actual total radiated energy and the average of the single-station estimates determined from the slip model would be representative of the directivity effect of the earthquake for the given slip model and station distribution. Thus, we could use this ratio to correct the average of the single-station energy estimates determined from data for directivity. By using this method, the actual radiated energy would still be determined from the data and the correction is only a factor that is applied to this observed estimate; also, the actual details of the slip model will not significantly affect the estimate of total radiated energy.

The procedure we adopted is outlined here: we compute the single-station energy estimates at each station from the observed records at the station (E_i^D). We use the best slip distribution model available in the literature and compute the single-station energy estimates from the model at the same stations (E_i^M). We also compute the actual total energy for the model (E^M). The correction factor is given by the ratio of the actual total energy for the model to the average of single-station energy estimates for the model, i.e.,

$$\text{Directivity correction} = \frac{E^M}{\frac{1}{N}\sum_{i=1}^{N} E_i^M}$$

The corrected energy is the product of the directivity correction and the average single-station energy estimate obtained from data.

Thus, the corrected energy $E_R = \dfrac{E^M}{\frac{1}{N}\sum_{i=1}^{N} E_i^M} \times \left[\frac{1}{N}\sum_{i=1}^{N} E_i^D\right]$

Using the above method and slip models from literature (given in the references listed), we calculated the directivity corrections for a few large earthquakes (Table 2.1).

Since the slip models used for the Landers earthquake, the Hector Mine earthquake and Taiwan earthquake were determined by inverting both regional and teleseismic data (and GPS data in some cases), we have better constraints on the slip distribution of these earthquakes. For the other large earthquakes (Shikotan, Kushiro-oki and Bolivia), slip distributions are not as well constrained, so the directivity corrections estimated are less reliable. However, these earthquakes are dip-slip earthquakes and the directivity corrections for vertical dip-slip earthquakes at teleseismic distances are less than a factor of 3; moreover, as mentioned earlier, the actual details of the slip model will not affect the estimate of radiated energy. Thus, we can be confident that radiated energy estimates for large earthquakes are not significantly affected by directivity (except in the case of strike-slip faults).

Table 2.1 Corrections for directivity

Earthquake-id	**Energy (J)**		**Directivity Correction**	**Source for Slip Model**
	Data R/T *	**Directivity Corrected**		
920628 - Landers	8.6×10^{15} (T)	2.6×10^{16}	3.08	Dreger et al., 94
		2.9×10^{16}	3.34	Wald & Heaton, 94
930115 - Kushiro-oki	4.2×10^{16} (T)	2.9×10^{16}	0.68	Takeo et al., 96
941004 - Shikotan	1.5×10^{17} (T)	1.4×10^{17}	0.93	Kikuchi et al., 95
940609 - Bolivia	1.3×10^{17} (T)	1.3×10^{17}	0.98	Kikuchi et al., 94
950730 - Chile	2.6×10^{16} (T)	2.1×10^{16}	0.80	Ruegg et al., 96
990920 - Taiwan	8.8×10^{15} (T)	6.6×10^{15}	0.76	Ji et al., 02
991016 - Hector	2.0×10^{15} (T)	1.0×10^{15}	0.49	Ji et al., 02
	3.0×10^{15} (R)	0.9×10^{15}	0.31	Ji et al., 02

* R – regional data used to compute energy; T – teleseismic data used to compute energy.

2.1.2 Attenuation

Anelastic processes in the earth attenuate seismic waves as they travel from the source to the receiver. Attenuation of seismic waves occurs over a broad range of frequencies and hence attenuation itself is a function of frequency. In the earth, attenuation varies laterally and is also a function of depth, with the highest attenuation occurring in the upper mantle. In body-wave studies, we account for the effects of attenuation by using a parameter $t^*(f) = \int_{path} \frac{dt}{Q(f)}$ (travel time divided by a Q along the path), where Q is the intrinsic attenuation factor. Q is inversely proportional to the fractional loss of energy per cycle of oscillation; thus, a larger Q implies smaller attenuation. If A_0 is the amplitude of the seismic wave at the source, the amplitude of a seismic wave at the receiver is given by $A = A_0 e^{-\pi f t^*(f)}$. To determine radiated energy, we have to correct the observed data for this loss of energy due to attenuation (i.e., we want to recover A_0). However, the attenuation structure of the earth, especially at higher frequencies, is not very well known. The exact relationship that governs the frequency dependence of the attenuation factor is poorly understood but in the most models, attenuation decreases (Q increases, $t^*(f)$ decreases) with frequency.

To compute energy from teleseismic data, we used the best available attenuation model and modified it to include the effects of lateral heterogeneities. The details of the approach are outlined in Appendix B. We also examined the effect of attenuation on energy estimates by performing a simple test. Assuming that the source spectrum can be modeled by a spectrum of the form $\hat{\dot{M}}(\omega) = M_0\, \omega_c^2 / (\omega^2 + \omega_c^2)$, where the corner frequency, $f_c = 0.49\beta(\Delta\sigma_s / M_0)^{1/3}$ [also known as ω^2 model, *Brune*, 1970; *Brune*, 1971],

$\beta = 3.6\ \mathrm{km/s}$ and $\Delta\sigma_s = 30\ \mathrm{bar}$, and using equation (2.2), we calculate the radiated energy for different values of t^* (here t^* is not a function of frequency).

Subsequently, we compute the ratio of energy at a given value of t^* to the energy when t^* = 0, i.e., the fraction of radiated energy that would be received at a station after accounting for the energy lost in attenuation. Since the energy spectral density is strongly peaked at the corner frequency for this model, in large earthquakes (small corner frequencies, ω_c) most of the radiated energy is at lower frequencies and hence an increase in t^* does not cause a significant loss in the radiated energy. This can be observed from Figure 2.5, where the y-axis is the ratio of energy when t^* has the values shown on the plot to the energy when t^*=0, e.g., for the curve labeled t^*=0.1 on the Figure 2.5, Ratio$= E_S(t^* = 0.1) \big/ E_S(t^* = 0)$. Thus, for an earthquake of $M_w = 7.0$ an increase in t^* from 0.1 to 1.0 results in a decrease of a factor of 2.5 in radiated energy and for an earthquake of $M_w = 8.0$, an increase in t^* from 0.1 to 1.0 results in a decrease of a factor of 1.5 in radiated energy. Thus, even an order of magnitude change in t^* values (which is much larger than the changes we would expect in attenuation models of the real earth), does not change the energy estimates of large earthquakes significantly. Though this is a simple case where t^* is not a function of frequency and the source model falls off as ω^2, it illustrates that the energy estimates of large earthquakes are not significantly affected by changes in the attenuation model. If the source spectra are complicated at higher frequencies, for example, if the amplitude increased at some frequency and then decreased, we would need to re-evaluate our results. However, this would require better high-frequency attenuation models of the earth than are currently available.

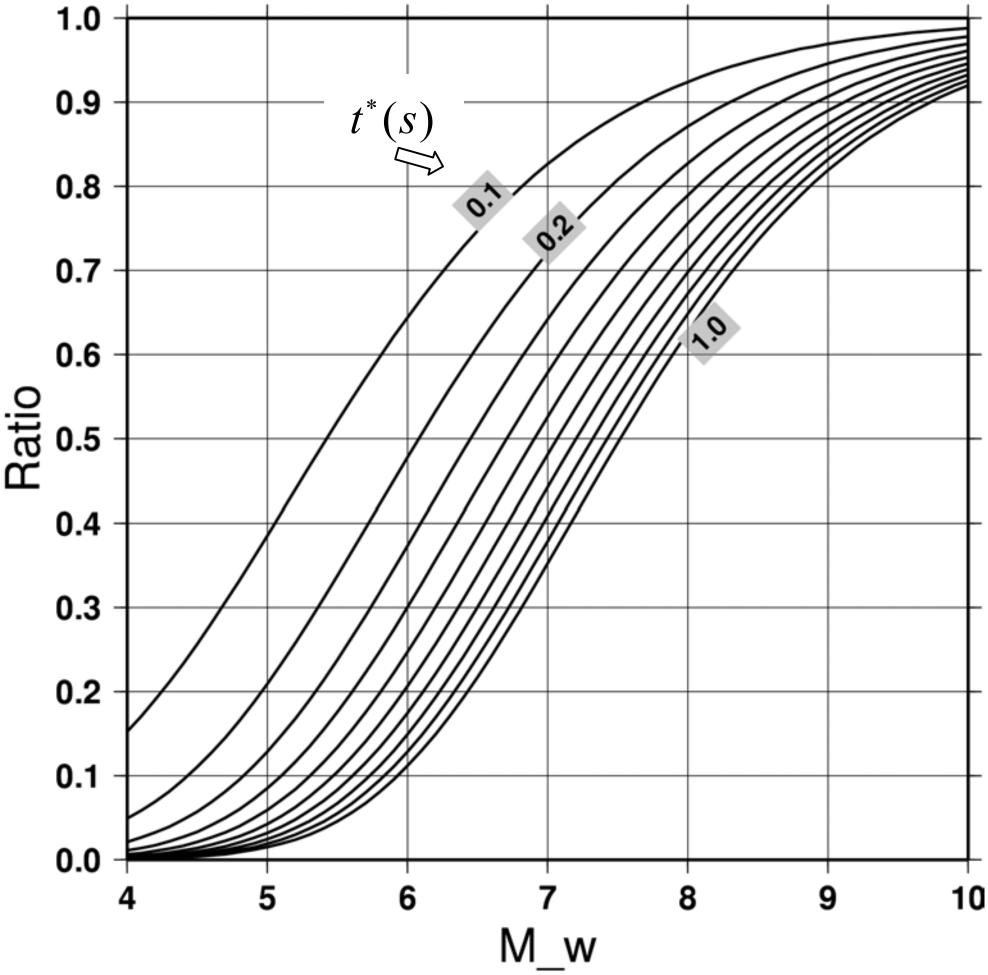

Figure 2.5 Plot to demonstrate the effect of t^* (in seconds) on energy estimates of earthquakes. The y-axis is the ratio of the energy when t^* has different values (0.1-1.0) to the ratio of energy when $t^* = 0$. This plot shows that for model assumed variations in t^* do not affect the energy estimates of large earthquakes by more than a factor of 2 (see text for details).

2.1.3 Radiation Pattern

From equation (2.3), we observe that to compute radiated energy, the displacement spectrum should be corrected for the radiation pattern factor $R(\theta,\phi)$. The radiation pattern factor determines the azimuthal variation in the amplitude of the seismic waves and is a function of the take-off angle of the seismic ray and the azimuth of the station. Thus, radiation pattern depends on the depth and geometry of the source. To backproject the data from the seismic station to the source, we remove the effect of the radiation pattern calculated for the specific source-receiver geometry and apply the average radiation pattern calculated over the focal sphere (4/15 for the *P* wave and 2/5 for the *S* wave as shown in equations 2.9 and 2.11). In this section, we discuss the problems that arise when we apply this correction to obtain energy from teleseismic data.

In shallow earthquakes recorded at teleseismic distances, the direct phases radiated by the earthquake interfere with the reflected phases and we cannot measure the energy flux in a single phase. Thus, the teleseismic waveforms radiated by shallow events are usually modeled as a group of phases [*Kanamori and Stewart*, 1978; *Boatwright and Choy*, 1986]. For example, the *P* wave group comprises the direct *P* phase, and the depth phases, *pP* and *sP*. When the energy carried by these phases is small, the correction for the radiation pattern factor is large. This is especially the case for shallow strike-slip earthquakes, as has been pointed out by several investigators [e.g., *Boore and Boatwright*, 1984; *Boatwright and Choy*, 1986; *Newman and Okal*, 1998]. In strike-slip earthquakes, all three rays contributing to the *P* wave group leave the source close to the null axis, and hence the radiation pattern coefficient for the individual rays as well as for the wave group as a whole is small and, consequently, the correction applied to the energy flux is large. The problem arises when the geometry of the source is not well known, or when the focal mechanism is inaccurate, or in the presence of lateral heterogeneities that scatter the waves. In such cases, the correction used is inappropriate and can yield erroneous estimates of radiated energy. Scattered high-frequency energy can add energy to the observed waveform and result in higher estimates of energy. There is no straightforward correction for these effects, hence the difficulty in obtaining accurate estimates of teleseismic energy for strike-slip earthquakes. In our study, we select a time window such that we minimize the inclusion of scattered arrivals in our energy estimates; also, we use a radiation pattern factor of 0.2 as a cut-off for the *P* wave group, so as to exclude nodal stations in our energy estimates. This value was selected based on observing variation in single-station energy estimates as a function of radiation pattern factor.

2.1.4 Source Structure

In computing radiated energy, we backproject the seismic waves to the source and determine the wave energy that radiates from the focal sphere surrounding the source. The underlying assumption in this formulation is the homogeneity of the medium surrounding the source, but the material surrounding the earthquake source is far from homogenous. For example, in subduction zone earthquakes that occur at the plate interface, energy is radiated into the subducting oceanic plate as well as the overlying continental plate. For a reasonable contrast in density and velocity (two layers), the energy estimates would change by a factor of two or less. Thus, except in the case of sharp density and velocity contrasts, radiated energy estimates would not be significantly affected by heterogeneous source structure if the average values of density and velocity at the source region were used.

2.1.5 Scattering

Scattering of seismic energy is caused when the seismic waves interact with small-scale heterogeneities. Due to scattering, a part of the high-frequency energy arrives after the direct arrivals in waves that are called coda. Scattering can also decrease the amplitude of a seismic phase by shifting energy from the direct arrival into the coda. Thus, scattered energy can add or remove energy from the direct arrivals and affect the estimates of radiated energy. In most cases, by choosing a time window to include all the phases of interest (the *P* wave group for shallow earthquakes or the direct *P* for deep earthquakes), but excluding most of the scattered arrivals, we can limit the amount of scattered energy that is included in the energy estimates. However, at nodal stations, the signal-to-noise ratio is low and hence the scattered energy can be a significant part of the total energy; to avoid this problem, we exclude the nodal stations and only use stations that have radiation pattern factors 0.2 or larger in our energy estimates.

2.2 Energy Estimates from Regional Data: EGF Technique

In this section, we will discuss a method of estimating energy from regional data, its application to the Hector Mine earthquake and the comparison between regional and teleseismic estimates for this earthquake. Regional data, where available, provide a good dataset that can be exploited to obtain accurate estimates of energy. Since, the distance between the source and receiver is small, less energy is lost in attenuation and geometric spreading. Also, dense station networks provide a good azimuthal distribution of stations; detailed slip inversions are possible and the resulting slip models can be used to correct for directivity effects.

With the advent of regional networks, several investigators estimated energy from regional data [*Kanamori et al.*, 1993; *Singh and Ordaz*, 1994]. Earlier estimates of radiated energy from regional data of other earthquakes were obtained by the integration of squared ground-motion velocity records (or integration of ground-motion velocity spectra) and application of empirical distance attenuation and station corrections [*Kanamori et al.*, 1993; *Singh and Ordaz*, 1994]. Another method that uses coda waves to determine radiated energy [*Mayeda and Walter*, 1996] also applies empirical corrections to remove near-site attenuation and amplification effects. However, the method that we use corrects for attenuation and site effects through the use of events smaller than the mainshock as empirical Green’s functions; thus, we have robust estimates of energy from the source spectrum of the regional data. In the following sections, we will discuss the regional estimates of radiated energy obtained using the EGF method for the Hector Mine earthquake. The Hector Mine earthquake is unique in that both the mainshock and aftershock data are very well recorded and hence we can use an empirical Green's function (EGF) method to determine the source spectrum.

2.2.1 Hector Mine Earthquake

The M_w=7.1 October 16, 1999, Hector Mine, California, earthquake provided us with an excellent data set to test the EGF technique. The Hector Mine earthquake and its aftershocks were well recorded at 67 TriNet stations in Southern California. The good signal-to-noise ratio of the mainshock and several aftershocks enabled the use of the empirical Green's function method to determine the source time function. As mentioned earlier, to obtain accurate estimates of energy, we have to correct the seismic wave energy for the propagation path effects. Uncertainty in energy estimates largely is due to uncertainty in the corrections applied to remove these effects. For the Hector Mine earthquake, we overcome this difficulty by using an empirical Green’s function deconvolution to estimate the source moment-rate spectrum of the Hector mainshock for the regional data. The energy estimates computed from these source moment-rate spectra are robust and hence this event can be used as a calibration event to study radiated energy from other events.

2.2.2 Regional Data

The Hector Mine earthquake and its aftershocks occurred within the dense array of TriNet [*Mori et al.*, 1998] stations in Southern California (Figure 2.6). The data are archived at the Southern California Earthquake Center (SCEC) Data Center. In our analysis, we use the tangential components of the integrated acceleration records for the mainshock and broadband velocity records for the aftershocks (empirical Green's functions). Figure 2.7a shows the tangential component of the velocity record of the mainshock and one of the aftershocks (EGF-5) at station PAS. The mainshock velocity record shown in the figure is obtained by integrating the original acceleration record. We use about 150 seconds of the mainshock and aftershock data so that we include almost all the *S* wave energy.

2.2.3 EGF Method Applied to the Hector Mine Earthquake

To determine the source time function, we use five events (one foreshock and four aftershocks with M_w ~ 2.8-4.5, see Figure 2.6 and table 2.2) located close to the hypocenter of the mainshock as empirical Green's functions (EGF) [*Frankel and Kanamori*, 1983; *Hartzell*, 1978; *Mori*, 1993; *Mori and Frankel*, 1990]. We deconvolve the EGF record from the mainshock record to remove the path and site effects from the mainshock.

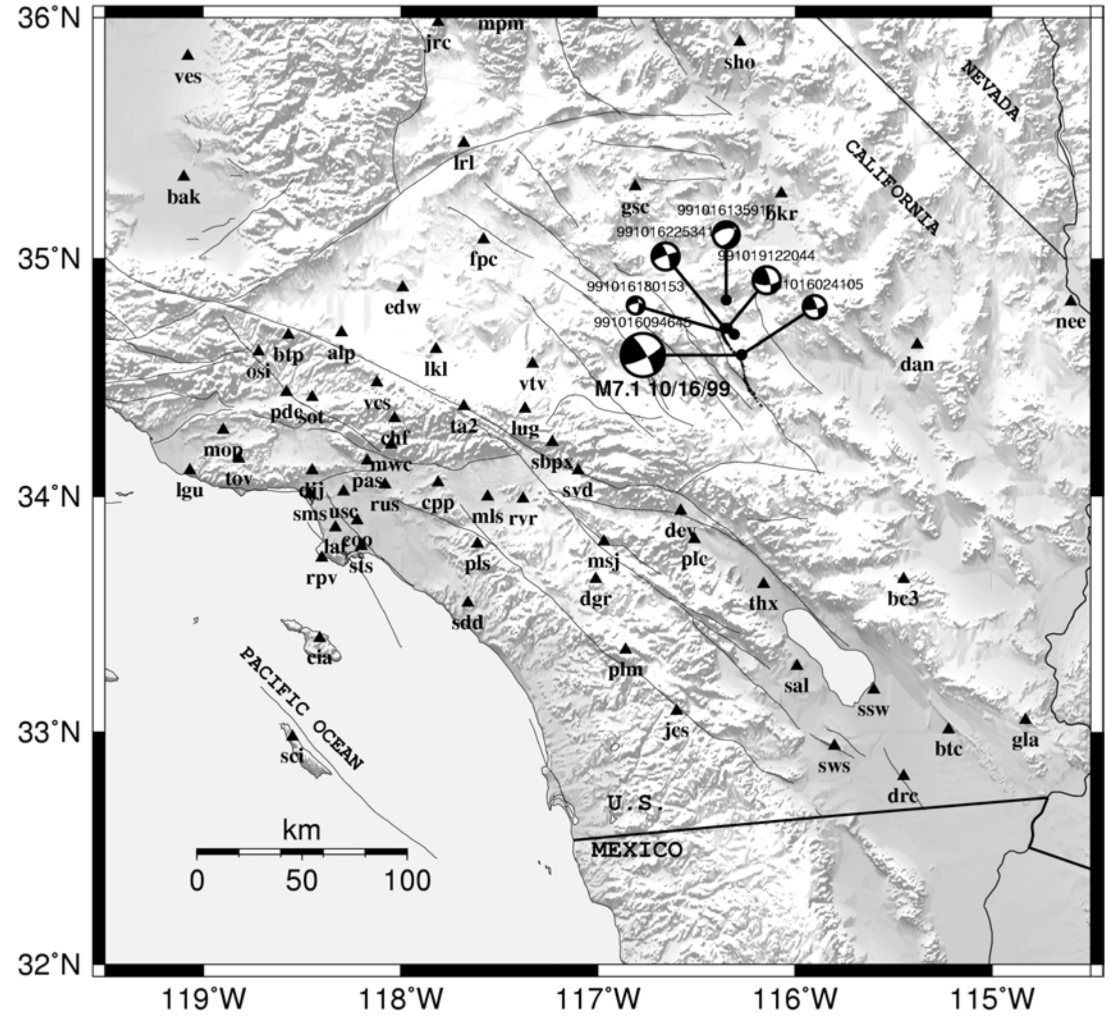

Figure 2.6 Location map of the M_w=7.1, October 16, 1999, Hector Mine, California, earthquake. The focal mechanisms (lower hemisphere) of the mainshock and the five EGFs used in the study are shown. Triangles represent seismic stations.

Table 2.2: Mainshock and aftershock data

Name	Origin Time	Latitude	Longitude	Depth (km)	*M	Strike	Dip	Rake
EGF-1	19991016024105	34.59°N	116.26°W	4.4	3.7	77°	74°	15°
MAIN	19991016094645	34.59°N	116.27°W	6.2	7.1	330°	78°	165°
EGF-2	19991016135917	34.83°N	116.35°W	4.1	4.4	257°	53°	-59°
EGF-3	19991016180153	34.68°N	116.31°W	5.1	2.8	260°	68°	-32°
EGF-4	19991016225341	34.71°N	116.36°W	3.1	4.5	250°	83°	-15°
EGF-5	19991019122044	34.71°N	116.34°W	3.0	4.1	86°	62°	20°

*M represents the local magnitude, M_L, of the empirical Green's functions events, and the moment magnitude, M_w, of the mainshock.

Figure 2.7(a) shows the mainshock record, the aftershock record and the result of the deconvolution at station Pasadena (PAS). The source spectrum is obtained by dividing the mainshock amplitude spectrum by the aftershock amplitude spectrum. The raw spectra occasionally have isolated spectral holes that probably are due to interference effects. To prevent these spectral holes from unduly influencing the estimates of the moment-rate spectrum, we smooth both the mainshock and aftershock spectra before spectral division. The smoothing is accomplished by computing a running average over a moving window of width 2 percent of the total frequency range. The deconvolved spectrum is scaled by the scalar moment of the EGF to give the source spectrum of the mainshock. Figure 2.7(b) shows the smoothed mainshock velocity spectrum, aftershock (EGF-5) velocity spectrum, and the source spectrum obtained by the spectral division at station PAS.

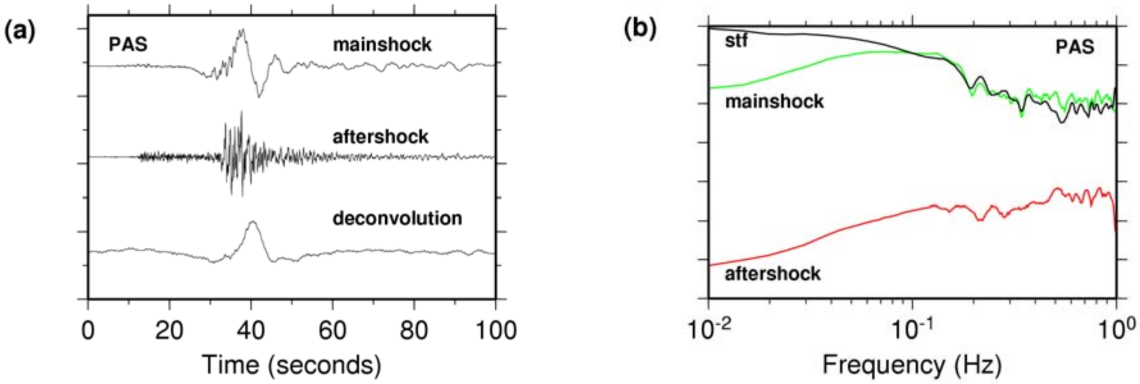

Figure 2.7 Results of EGF deconvolution: **(a)** the figure shows the velocity records of the mainshock and aftershock (19991019122044) and the source time function (STF) obtained by deconvolution at station PAS, **(b)** the velocity spectra of the mainshock and aftershock and the source spectrum obtained by spectral division are shown.

The deconvolution assumes that the mainshock and EGF are located such that the path effects are almost the same for both events. However, for a large event like the Hector Mine earthquake, we have to account for the finite depth extent of the mainshock and for the uncertainty in the exact depth of the EGF events. To consider this effect, we computed synthetic spectra for a finite fault [*Hisada*, 1994] and for point sources at different depths using the eastern California velocity model [*Jones and Helmberger*, 1998]. The source spectrum is scaled by the ratio of the spectrum of the finite fault to the spectrum of a point source at a given depth. Thus, we obtain depth-corrected source spectra at each depth of the point source. However, the depth correction does not change the source spectrum significantly.

Due to the finite duration of the records used in the analysis and the poor signal-to-noise ratio of the aftershock data at long periods, the absolute value of the spectral amplitude at long periods is difficult to determine. We observe that the regional moment-rate spectra become unreliable below 0.05 Hz. To remedy this, we use a theoretical spectrum in the form $\hat{\dot{M}}(\omega) = M_0\omega_c^n/(\omega^n + \omega_c^n)$ that fits the teleseismic moment-rate spectrum (obtained from Ji et. al., [2002b]; thin dark line shown in Figure 2.7b), and determine the amplitude of the theoretical spectrum at 0.05 Hz. We then adjust the amplitude of the regional moment-rate spectrum so that its absolute amplitude at 0.05 Hz is the same as that of the theoretical spectrum.

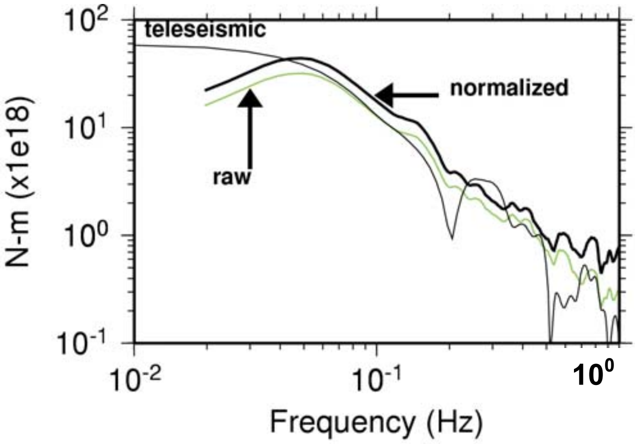

Figure 2.8 The average normalized source spectrum obtained by using event EGF-5 is shown by the thick dark line. The gray curve shows the raw source spectrum. The thin dark line represents the teleseismic moment rate spectrum obtained from Ji et al. [2002b].

Figure 2.8 shows the raw source spectrum and average normalized source spectrum obtained by using EGF-5. There is some ambiguity in this process, but the energy mainly is determined from the regional moment-rate spectrum at each station, and teleseismic data are used only for minor adjustment. From the source spectrum determined above, the radiated energy for a point source can be calculated using equation (2.2). The first and the second terms in parentheses on the right-hand side of the equation represent contributions from *P* and *S* waves, respectively; the *P* wave contribution is about 5 percent of the *S* wave contribution and is ignored here.

2.2.4 Results

We calculate the energy using equation (2.2) for $\rho = 2.7$ g/cm^3, and $\beta = 3.3$ km/s for each depth of the EGF. Figure 2.9 shows the energy estimated from all the stations for each EGF. The aftershock records at nodal stations and at stations more than 200 km away from the source have poorer signal-to-noise ratios. The open circles represent the energy at these stations and show a larger scatter than the closed circles. The mean estimate of radiated energy computed using the values at the selected stations (open circles in Figure 2.9) is 3.0 x 10^{15} J and the standard deviation is 0.9 x 10^{15} J.

Of the five EGFs, two aftershocks (EGF-4 and EGF-5) have mechanisms that are most similar to the mainshock and are located close to the fault trace. The energy estimates obtained using these aftershocks as EGFs have the smallest scatter. The deconvolution does not work as well for the foreshock (EGF-1) because of its small size and hence low amplitude. Despite the differences in focal mechanisms of the mainshock and EGF events, the energy estimates are still clustered between 2 x 10^{15} J and 4 x 10^{15} J.

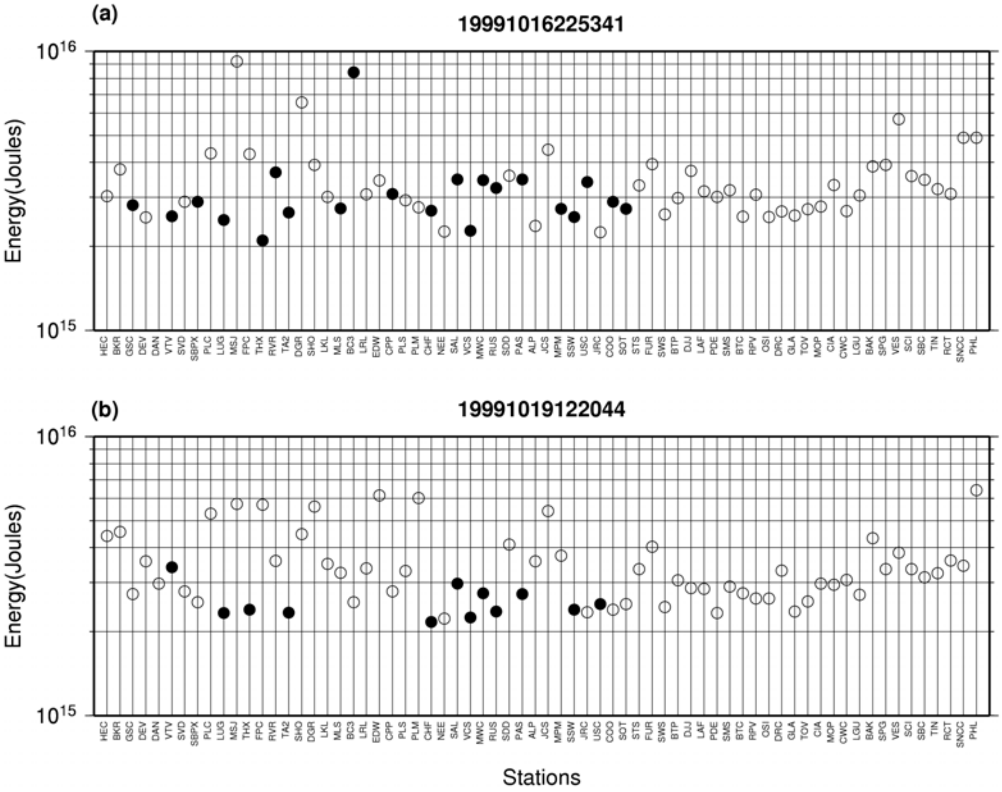

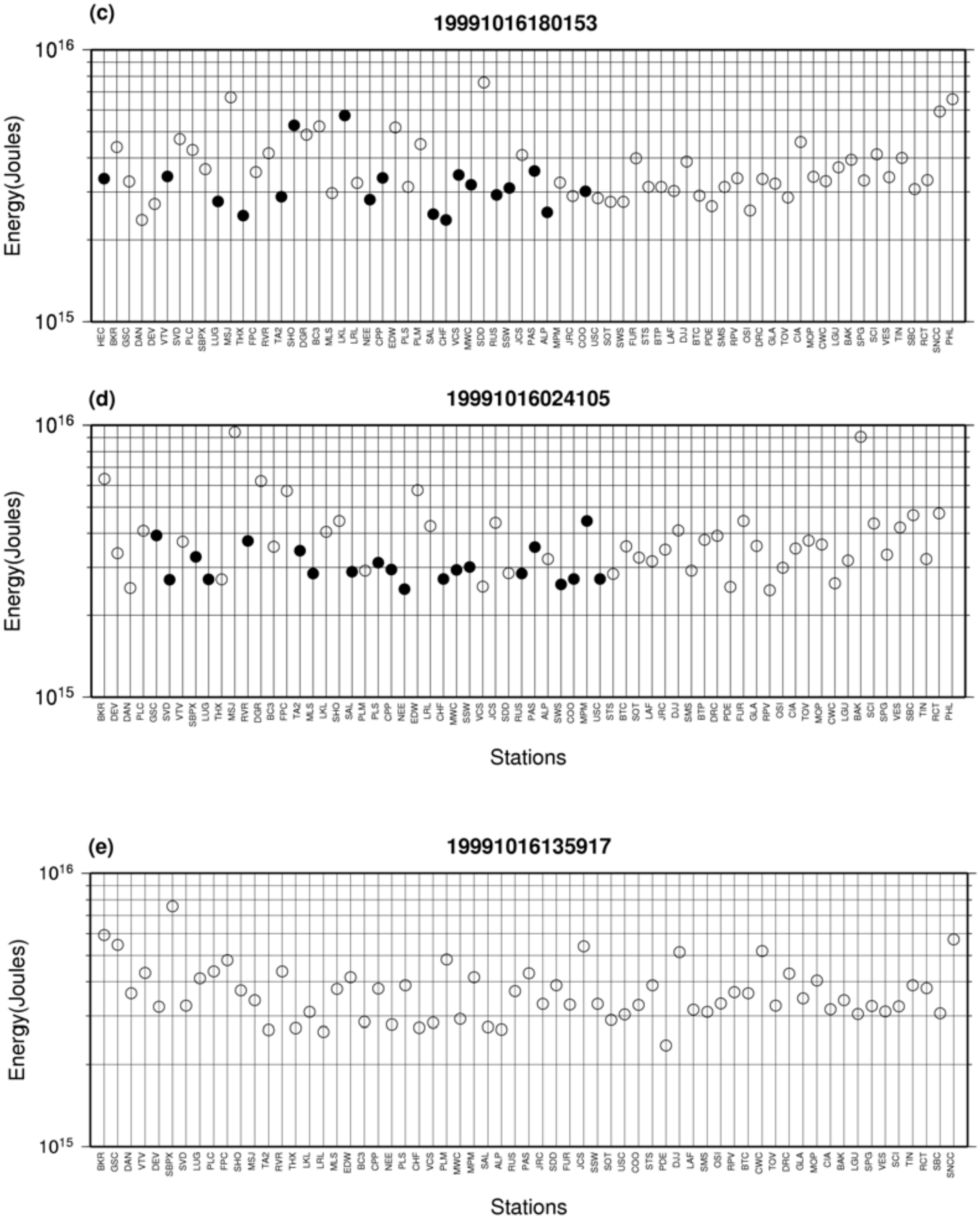

Figure 2.9 Regional estimates of radiated energy: each figure is a plot of the radiated energy at different stations obtained by using different events as EGFs. **(a)** EGF-1; **(b)** EGF-2; **(c)** EGF-3; **(d)** EGF-4; **(e)** EGF-5. The closed circles represent stations that are within 200 km of the mainshock and away from the nodal planes.

As mentioned earlier, the regional source spectrum below 0.05 Hz is noisy. Thus, we calculate the integral of the adjusted regional source spectrum between 0.05 Hz and 1 Hz. To compute energy between 0 and 0.05 Hz, we use a theoretical spectrum in the form $\hat{\dot{M}}(\omega) = M_0\omega_c^n/(\omega^n + \omega_c^n)$ that fits the teleseismic moment-rate spectrum (the fit results in ω_c = 0.37 radians/s, and n = 1.8), and determine that the energy in this frequency range is only about 8 percent of the total energy. Using this theoretical source spectrum, we also determine that the energy at frequencies above 1 Hz is about 20 percent of the energy from the frequency band below 1 Hz.

Equation (2.2) gives the radiated energy for a point source. For a finite source, the directivity effect should be removed. The Hector Mine earthquake is essentially a bi-lateral rupture with a total fault length of about 40 km [*Ji et al.*, 2002b; *Trieman et al.*, 2001]. From the directivity corrections computed earlier (section 2.1.1), the energy after correction for the directivity effect is 1 x 10^{15} J.

The deconvolution assumes that the EGF amplitude spectra are flat in the frequency range of interest (i.e., at frequencies less than 1 Hz). The EGF events used in this study are at least 2.6 magnitude units smaller than the mainshock, so their theoretical corner frequencies (using the relation $f_c = 0.49\beta(\Delta\sigma_s/M_0)^{1/3}$, where β = 3.7 km/s, $\Delta\sigma_s$ = 3 MPa and M_0 is the moment) are larger than 1 Hz. Also, our calculations show that the corner frequency effect does not affect the energy estimates significantly.

2.2 Calibration of Teleseismic Methods of Estimating Radiated Energy

2.2.1 Data and Method

The teleseismic data for the Hector Mine earthquake were obtained from the IRIS Data Management Center. We use vertical component data (BHZ channel) of stations at distances between 30° and 90° in the teleseismic study. *P* waves carry only 5 percent of the total seismic energy. However, as *S* waves are more attenuated than *P* waves, we use *P* waves in our analysis. The energy obtained from the *P* waves is used to estimate the total energy, using equation (2.2).

For a shallow event like the Hector Mine earthquake (depth ~ 7 km; *Hauksson et al.*, [2001]), it is difficult to separate the *P*, *pP* and *sP* phases. So, when we study such events, we have to consider the *P* wave group as a whole. A closer look at teleseismic displacement records (*e.g.*, station SJG shown in Figure 2.10) reveals reverberation following *sP*, which is probably caused by near-source scattering. To avoid the inclusion of these scattered waves in the analysis, we use about 30 seconds of data (shown in Figure 2.10).

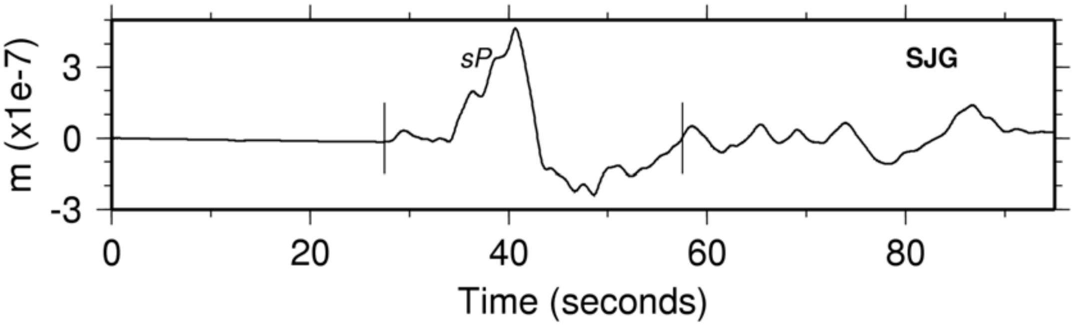

Figure 2.10 The P group displacement record for the station SJG is shown here. The largest phase, sP, is marked. The tick marks bound the 30 seconds of data used in the actual energy computation. Scattered arrivals can be clearly observed after the arrival of sP phase.

It is difficult to use the EGF technique to determine energy from teleseismic data except in the case of large earthquakes ($M_W \geq 8.0$) because the data quality of aftershocks recorded at teleseismic distances is not good. For example, for an earthquake of magnitude M_W=7.5, the EGF has to be an aftershock at least two units in magnitude smaller than the mainshock, and teleseismic recordings of earthquakes of this magnitude do not have sufficient signal-to-noise ratio to be used as an EGF for reliable estimates of energy.

Thus, we compute the radiated energy from teleseismic data using two different methods. The first method is the conventional (NEIC) method, where the energy is computed by applying corrections to the integrated velocity spectrum [*Boatwright and Choy*, 1986]. The amplitude of the moment-rate spectrum is determined using equation (2.3), where $R(\theta,\phi)$ is the effective radiation pattern for the *P* wave group. $R(\theta,\phi)$ is obtained by computing the amplitudes of the *P*, *pP* and *sP* phases at each station and then taking the root-mean-square value (for a strike-slip earthquake this factor is dominated by the *sP* radiation pattern). This method does not account for the effect of the phase differences between the *P*, *pP* and *sP* phases [*Houston*, 1990b].

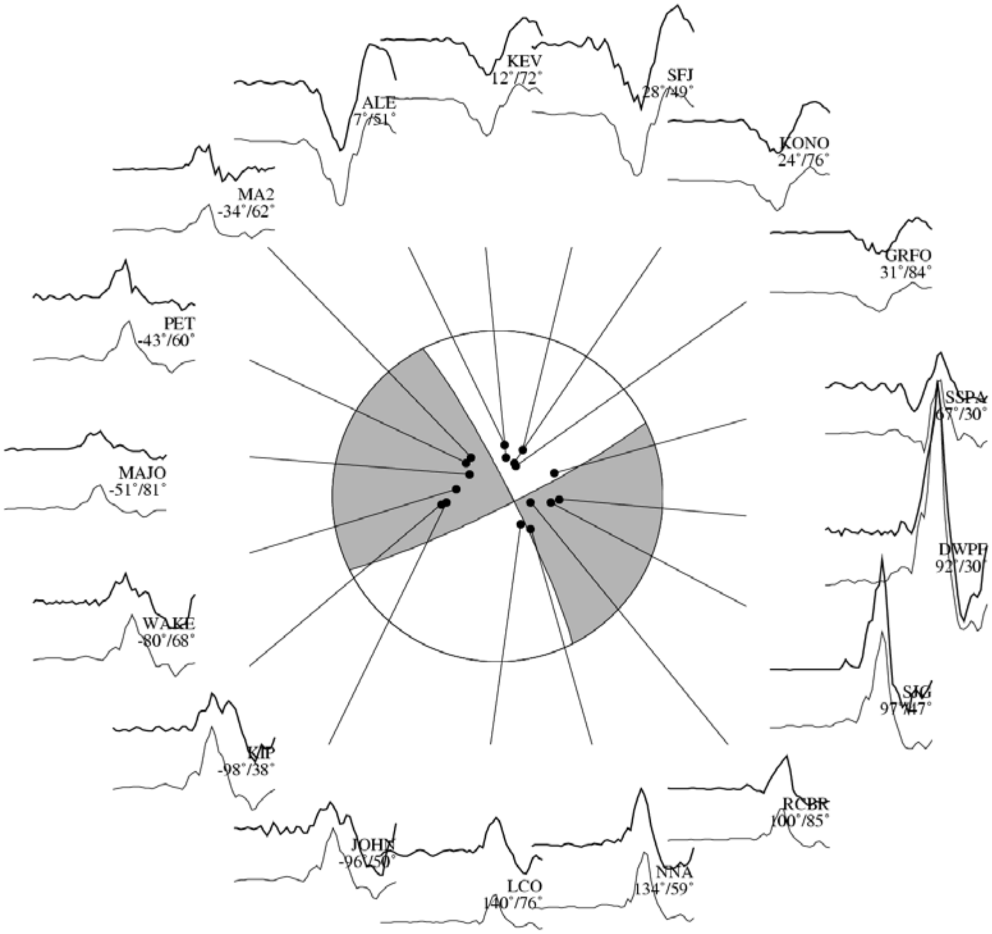

Figure 2.11 *P* wave focal mechanism (lower hemisphere projection) of the Hector Mine earthquake. The figure shows the displacement data and synthetics at teleseismic stations. The station name, its azimuth and distance from the epicenter are shown. The synthetics are obtained by a waveform inversion [Kikuchi and Kanamori, 1991].

In the second method, we compute Green's functions for the appropriate near-source structure (the eastern California velocity model, *Jones and Helmberger*, [1998]) and deconvolve the Green's function from the mainshock data to obtain the source spectrum at each station. As the Green's functions vary with depth and the fault ruptures over a finite-depth extent, we decided to use a Green's function averaged over depth (1-7 km). Uncertainty in the near-source structure could result in inaccurate Green's functions and hence inaccurate estimates of energy. To ensure that the structure that we use is appropriate, we perform a teleseismic inversion of the data at 37 stations using the method of Kikuchi and Kanamori [1991]. Figure 2.11 shows the *P* wave focal mechanism, the displacement data (top trace) and synthetics (bottom trace) at 18 of the stations used in the study; the synthetics match the data reasonably well. The teleseismic moment-rate function obtained from this inversion is very similar to that obtained by *Ji et al.*, [2002b].

We estimate the attenuation correction using frequency dependent t^* models that are derived from the models described in *Der* [1998] (see Appendix for details). As the radiation pattern for a strike-slip event is small, small changes in the mechanism can have a significant effect on the estimates of radiated energy. The radiation pattern is particularly sensitive to changes in the dip angle of the fault plane. We observe that by changing the dip from 78° (the value obtained from the inversion of regional data) to 84° (the value obtained from the teleseismic inversion described above), the average teleseismic estimates of radiated energy vary from 2×10^{15} J to 7×10^{15} J. Synthetics computed using these different values of dip do not differ significantly from each other.

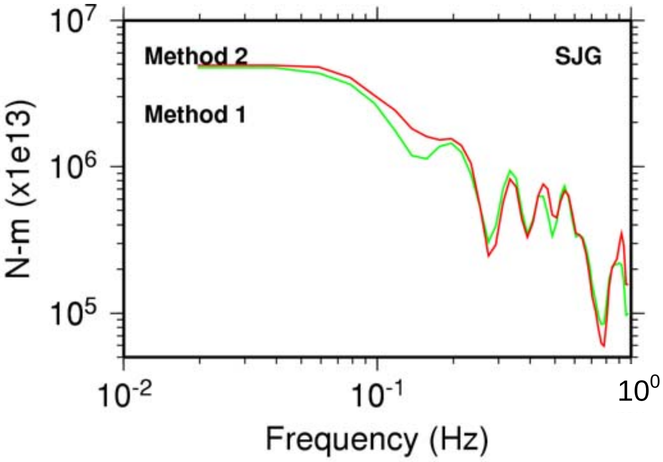

Figure 2.12 The teleseismic moment-rate spectrum obtained at station SJG using methods 1 and 2 (see text) for the Hector Mine earthquake.

2.2.2 Results

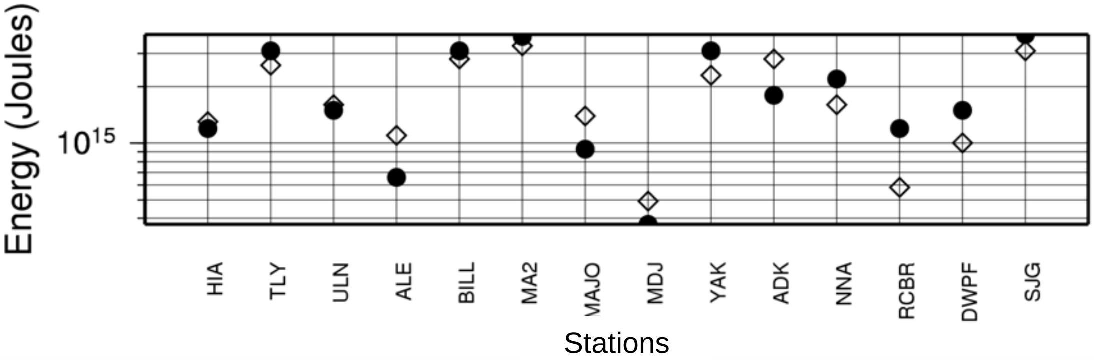

Figure 2.13 Radiated energy at teleseismic stations for the Hector Mine earthquake. The open diamonds represent the energy estimates obtained using method 1 and the closed circles represent the estimates obtained using method 2. There is a large scatter in the energy estimates from teleseismic data.

Figure 2.12 shows the source spectra at station SJG corrected using method 1 and method 2. The average value of the energy estimated using the first method is 1.8 x 10^{15} J while the average estimate of energy from the second method is 2.0 x 10^{15} J (the mechanism we use is given in Table 2.1).

Figure 2.13 shows the energy estimates at 14 stations using method 1 (open diamonds) and method 2 (closed circles). In this study, we obtain a mean estimate of energy from teleseismic data of 1.8 x 10^{15} J and 2.0 x 10^{15} J using two different teleseismic methods; these estimates are almost the same as that obtained from regional data (3 x 10^{15} J). These estimates of radiated energy for the Hector Mine earthquake are in agreement with the values obtained by *Boatwright* [2001]. After correcting for directivity, the regional and teleseismic estimates of energy are 1 x 10^{15} J.

2.3 Energy Estimates for Small Earthquakes

Estimating energy for small earthquakes is extremely challenging because smaller events have most of their energy at higher frequencies where the signal-to-noise ratio is very poor because of the strong attenuation of high-frequency waves and the complex free-surface effects. One of the solutions to this problem is to measure energy from seismic data recorded by borehole instruments. The Cajon Pass drill hole experiment was one such study where seismic instruments, installed at depths of 2.5 km inside a drill hole, recorded several small earthquakes ($M_L < 4.0$) [*Abercrombie and Leary*, 1993]. These data were used to calculate radiated energy [*Abercrombie*, 1995] and it was observed that radiated energy-to-moment ratios from these small earthquakes were smaller than expected (see Figure 2.14). Subsequent studies in Japan have also observed small energy-to-moment ratios for small earthquakes [*Matsuzawa*, 2001]. However, the results of these experiments are still not widely accepted; high-quality borehole data that is now becoming available may provide us with better energy estimates to validate these studies. Additionally, if we have high-quality data, the empirical Green's function method can be used to constrain the energy estimates for these small events better.

2.3 Discussion and Conclusions

From the regional estimates of radiated energy (1 x 10^{15} J) and teleseismic inversions for the moment (6 x 10^{19} Nm), the energy-to-moment ratio, (E_R / M_0), for the Hector Mine earthquake is 2 x 10^{-5}. Figure 2.14 shows the results from several regional studies. The energy-to-moment ratio is shown as a function of moment magnitude, M_w. The black circle represents the E_R / M_0 ratio of the Hector Mine earthquake. The difference in the ratio between large and small earthquakes has been used by *Kanamori and Heaton* [2000] and *Brodsky and Kanamori* [2001] to argue that, when the slip exceeds a threshold of 10 cm to 1 m, the frictional characteristics on the fault plane undergo a significant change because of processes such as melting, thermal pressurization or elastohydrodynamic lubrication. These hypotheses can be validated if the estimates of E_R / M_0 can be determined accurately.

The current estimates of E_R / M_0 are scattered over a large range (Figure 2.14) possibly due to inaccurate estimates of radiated energy. As we have demonstrated above, the regional estimates of radiated energy for the Hector Mine earthquake are robust and constitute an important data point for studies involving the radiated energy. Also, this event could serve as a calibration for future studies of radiated energy using teleseismic data. We think we have a better handle on the energy estimates of larger events and with better data quality, the EGF method can be extended to study smaller events; thus, with the increasing number of downhole stations, better instrumentation and greater knowledge of the earth's structure, it will become possible to improve the estimates of radiated energy from smaller earthquakes and understand the differences between the rupture mechanics of small and large earthquakes. Moreover, as will be shown in the subsequent Chapters, estimates of E_R / M_0 alone cannot be used to understand earthquake mechanics; we have to go one step further and determine static stress drop and then we can use both these parameters to interpret differences in rupture mechanics of earthquakes.

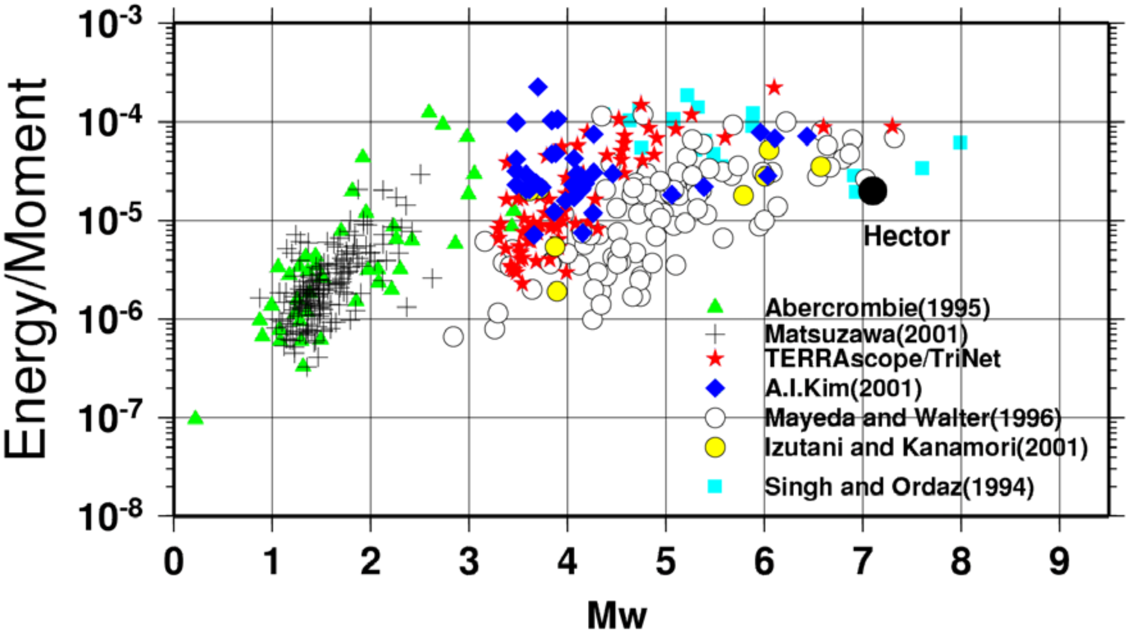

Figure 2.14 Energy-to-moment ratio (E_s/M_0) as a function of M_w. The plot shows the results of regional studies conducted for different earthquakes by several investigators. The triangles represent a study by Abercrombie et al. [1995], the pluses are from the study of Matsuzawa, [2001], the stars represent the study using TERRAscope/TriNet data [Kanamori et al., 1993], the diamonds represent the study of Kim [2001], the open circles are from Mayeda and Walter [1996], and the squares show the results of a study by Singh and Ordaz [1991]. The black circle shows our result for the Hector Mine earthquake.

CHAPTER 3

Relating Seismological Parameters to the Dynamics of Faulting

To understand the physics of earthquake process, we have to relate seismologically observable macroscopic parameters such as radiated energy, moment, rupture area and rupture velocity to the dynamics of faulting. To achieve this objective, we use tools developed in fracture mechanics. This chapter covers some background material in fracture mechanics and elaborates on how it can be used to understand earthquake rupture mechanics. In the framework of fracture mechanics, an earthquake may be considered as a dynamically propagating shear fracture, i.e., a crack that radiates seismic waves. The resulting motion (slip history) on the fault is related to the drop in shear stress. Several failure criteria and constitutive laws have been developed to relate the evolution of slip on the fault to the change in shear stress on the fault [*Scholz*, 1989]. In our study, we want to use a rupture model that captures the important physical processes that occur during fracture propagation.

To interpret seismological data, crack models are often used mainly because crack theories have been developed well. On the other hand, it is more intuitive to view seismic faulting as sliding on a frictional surface, where the physics of sliding friction, especially stick slip, plays an important role. Using frictional sliding models, earthquakes can be described as a result of stick slip frictional instabilities–the earthquake is the ‘slip’ and the ‘stick’ is the interseismic period of elastic strain accumulation. Seismic faulting in the earth is a complex process that may require a combination of crack models and frictional sliding models, or some other models for interpretation. Despite this complexity, crack models and frictional sliding models provide a useful framework for the interpretation of earthquake processes.

In the following discussion, we briefly describe the crack model and the frictional sliding model and show how the two models can be used to understand the dynamics of faulting. We discuss both models in the context of the processes that occur during stress drop on the fault and then use these models to understand the partitioning of energy in earthquakes.

3.1 Using Fracture Mechanics to Understand the Earthquake Problem

The discussion presented below will serve as a background to understand the dynamic processes that occur during stress relaxation in an earthquake. The crack model has been dealt with exhaustively in books on fracture mechanics [e.g., *Lawn*, 1993; *Scholz*, 1989] and we only give a brief introduction to the concepts that we will be using in our study. Frictional sliding models have also been studied by several investigators [e.g., *Rabinowicz*, 1965; *Scholz*, 1989]. Both models are complementary and can be used to understand earthquake dynamics [*Li*, 1987; *Scholz*, 1989].

3.1.1 Crack Model

Cracks, which are surface defects or flaws in a material, result in brittle failure of material by separation into parts. In the real earth, however, tectonic earthquakes seldom occur by the sudden appearance and propagation of a new shear crack. Instead, they occur by sudden slippage along a pre-existing fault plane or plate interface. Thus, in terms of crack theory, we are concerned with the extension of a pre-existing crack.

To understand the stress relaxation process in the crack model, we consider a crack of width $2a$ extending to infinity in the Z direction as shown in Figure 3.1. From linear elastic analysis of the crack tip field, for the crack to be in static equilibrium under a remote loading stress $\sigma_{zy} = \sigma_0$ when the uniform shear resistance of the crack is σ_f, the stress field near the crack tip, at $x = a + \varepsilon$, for a longitudinal shear crack (Mode III) can be given as [*Lawn*, 1993]

$$\sigma_{zy} = (\sigma_0 - \sigma_f)\sqrt{\frac{a}{2}}\varepsilon^{-1/2} = \frac{1}{\sqrt{2\pi}} K \varepsilon^{-1/2}, \qquad \textbf{(3.1)}$$

where $K = \sqrt{\pi\, a}\, \Delta\sigma$ is known as the stress intensity factor. Here a is the half width of the crack for a Mode III crack, but for other types of cracks we can qualitatively interpret it as $S^{1/2}$ and, $\Delta\sigma = (\sigma_0 - \sigma_f)$. The stress intensity factor gives the intensity of stress near the crack tip. If the material has no strength, the crack will keep growing, whereas if the material has some strength the crack will stop expanding. The stress intensity factor when the crack stops growing is called the critical stress intensity factor, K_c, and is also known as fracture toughness.

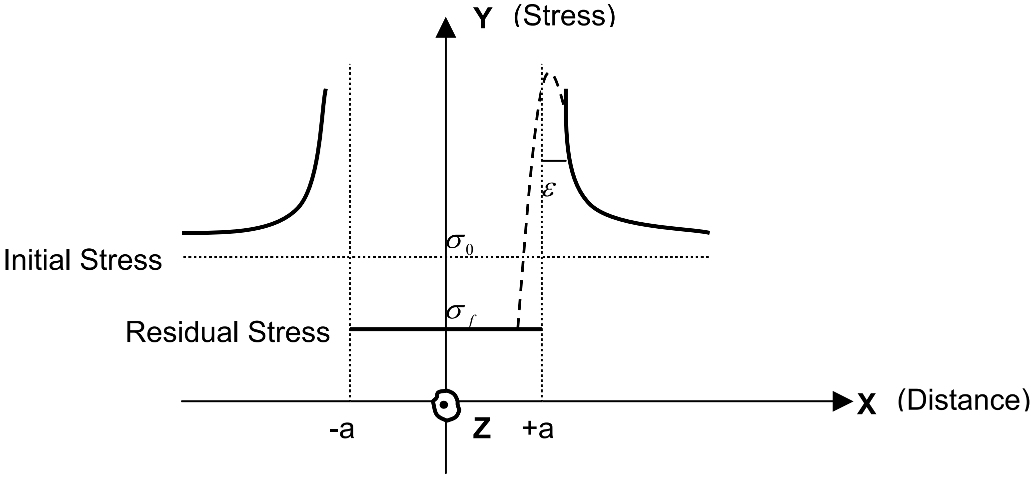

Figure 3.1 When stress, σ_0, is applied remotely on a crack of width 2a, which has a residual frictional stress of σ_f, the stress field near the crack tip, σ_{zy}, is given by the dark curve, and is singular at the crack tip. Physically such a singularity cannot exist and the material will yield, resulting in a breakdown zone at the crack tip so that the stress at the crack tip will be as shown by the dashed line.

The shear crack faces are at a residual frictional stress state (σ_f), which may be regarded as a reference stress level. The base friction, which determines the frictional strength on the fault, does not concern us in this discussion because the only parameter that matters is the stress difference. However, frictional strength does play a role in frictional heating during rupture propagation; but this frictional heating cannot be determined from seismology.

If we consider the energy involved in this crack problem, the potential energy release (per unit length in Z direction) is

$$\Delta W = (\sigma_0 + \sigma_f)\overline{D}S/2 = (\sigma_0 - \sigma_f)\overline{D}S/2 + \sigma_f \overline{D}S = \Delta W_0 + \sigma_f \overline{D}S \qquad \textbf{(3.2)}$$

where $\overline{D}$ is the average slip of the crack and S is the crack area. In the above equation, the second term on the right-hand side is the frictional energy and the first term is the strain energy release associated with crack extension. Substituting for $\overline{D} = C\Delta\sigma\, S^{1/2}/\mu$, where *C* is a constant of order unity, and $\Delta\sigma = (\sigma_0 - \sigma_f)$, we get

$$\Delta W_0 = (\sigma_0 - \sigma_f)\,\overline{D}\,S/2 = C(\Delta\sigma)^2 S^{3/2}/2\mu \qquad \textbf{(3.3)}$$

If there is no resistance to the crack tip, the crack will grow indefinitely. For a crack with an area S to stay in equilibrium (this is quasi-static equilibrium), the increment in ΔW_0, due to virtual crack extension, must be balanced by the surface energy required to create new crack surfaces at both crack tips (Griffith criterion). The surface energy is then given as

$$\delta(\Delta W_0) = G^* \delta\, S\ , \qquad \textbf{(3.4)}$$

where G^* is the energy release rate ('rate' stands for 'per unit area') for a crack in quasi-static equilibrium, also called the crack extension force or specific fracture energy.

From equations (3.4), (3.3), and (3.1), we can write

$$G^* = \frac{3C}{4\mu}(\Delta\sigma)^2 S^{1/2} = \frac{3C}{4\pi\mu}K^2 \tag{3.5}$$

This equation relates K to G. If the material has a finite strength, the crack will stop expanding, and the critical surface energy can then be defined as

$$G^*{}_c = \frac{3C}{4\pi\mu}K_c^2 \tag{3.6}$$

The expressions for K and G^* are different for different crack modes, but these differences are small compared to the gross approximations used in seismological applications.

From equation (3.1), we observe that there is a stress singularity at the crack tip where σ_{yz} approaches infinity as ε approaches zero. This is physically unrealistic as no material can withstand infinite shear stress. When the stress exceeds a certain level, the material will yield and behave inelastically at the crack tip; thus, the stress singularity at the crack tip is an artifact of the assumption of elastic behavior at the crack tip. The actual stress field at the crack tip will be smeared out as shown by the dashed curve in Figure 3.1.

Physically this would result in a zone of inelastic deformation, called the breakdown zone (Figure 3.2), around the crack tip. In this zone, energy is dissipated as the crack propagates and this energy can be interpreted as the specific fracture energy, G^*. If there is no breakdown zone (i.e., $G^* = 0$), the stress at a point that is very close to the crack tip will fall from σ_0 to σ_f immediately (as shown by curve (1) in Figure 3.2), whereas if there is a breakdown zone then the stress drops to the residual frictional value over a slip D_0 as shown by curve (2) in Figure 3.2. This parameter, D_0, is called the critical slip. With this model, the surface energy, G^*, can be approximately written as

$$G^* = \int_0^{D_0} \sigma \, dS \approx (\sigma_0 - \sigma_f) D_0 / 2 \qquad \textbf{(3.7)}$$

Thus, in terms of crack theory, the development of earthquake rupture can be understood as follows: consider a point just ahead of the crack tip (point P in figure 3.2).

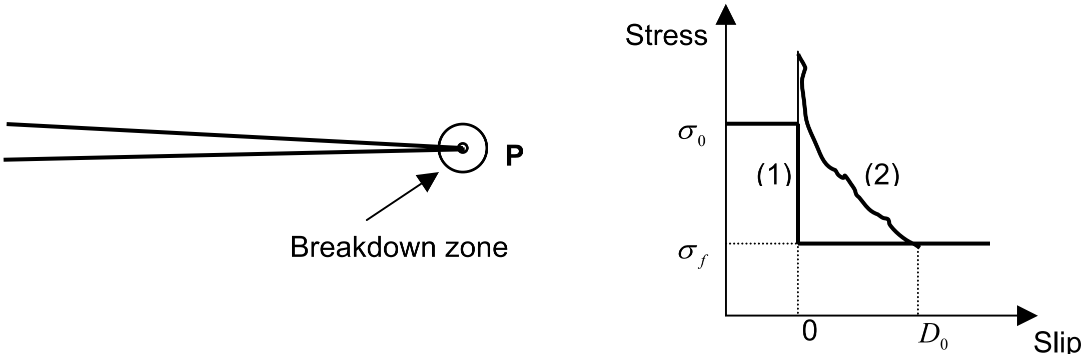

(a)

(b)

Figure 3.2 (a) Breakdown zone around the crack tip; **(b)** Stress relaxation representation of the breakdown zone: stress as a function of slip for a crack when there is no breakdown zone (curve 1) and for a crack when there is a breakdown zone (curve 2).

The applied stress at the point P is σ_0, and the static strength of the point is σ_y [*Scholz*, 1989]. As the rupture approaches the point, the stress at P rises due to the dynamic stress concentration ahead of the crack, and it reaches σ_y at the time the crack tip reaches P. When the crack tip reaches P, stress at P drops from the initial level to the residual frictional level over a critical slip, D_0, creating a deformed zone called the breakdown zone in this process. The stress history during slip depends on some prescribed constitutive friction law at P.

3.1.2 Frictional Sliding Model

In classical friction theory, the coefficient of static friction, μ_s and the coefficient of dynamic (also known as kinetic) friction, μ_k, are the two important parameters. If $\mu_k < \mu_s$, an instability occurs. Thus, variation in frictional resistance during sliding can produce a dynamic instability resulting in very sudden slip with an associated stress drop. In any physical system, the static friction cannot drop to dynamic friction instantly. A slip, D_c, is required before the static friction drops to dynamic friction, and steady sliding begins, as shown in Figure 3.3. As a fault surface is not smooth and friction on the surface is not uniform, sliding does not occur smoothly; it occurs in a stop-and-go fashion. This frictional behavior is called stick slip. The energy dissipated in relaxing static friction to dynamic friction is given as [*Li*, 1987; *Scholz*, 1989]

$$G_{sliding} = \int_0^{D_c} \sigma \, dS \approx (\sigma_0 - \sigma_f) D_c / 2 \qquad \textbf{(3.8)}$$

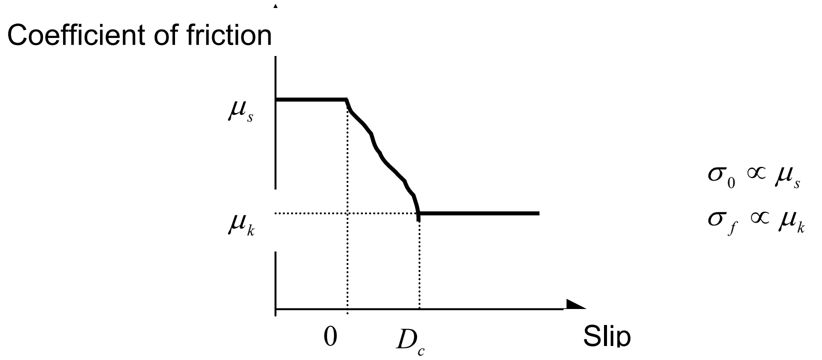

Figure 3.3 The stress falls from σ_0 to σ_f (from the static to dynamic friction levels) but for a physically realistic system, this transition from static to dynamic friction should occur over a finite slip distance, which is called the critical slip, D_c.

3.1.3 Relating the Crack Model to the Frictional Sliding Model

Both models described above relate the fault slip to the frictional stress on the fault and are hence equivalent [*Scholz*, 1989; *Li*, 1987]. They are different in the way in which they view the rupture process–in the crack model, a characteristic surface energy per unit area is required for crack extension, while in the frictional sliding model, the fault has to slip a critical slip, D_c, before unstable sliding begins at a constant friction. Thus, equation (3.7) for a crack model with D_0 replaced by D_c is equivalent to equation (3.8) for the frictional sliding model. From the two models, the fracture energy during stress drop can, thus, be written as

$$G^* = \int_0^{D_c} \sigma \, dS \approx (\sigma_0 - \sigma_f) D_c / 2 \qquad \mathbf{(3.9)}$$

Both models can be used to understand the earthquake process; the frictional sliding model probably gives us a greater intuition into the earthquake process, and hence it provides us with a useful framework to view earthquakes.

The exact variation of stress as a function of slip is not known. In the slip-weakening model (where the slip weakens the stress on the fault) [*Ida*, 1972; 1973], the stress is some function of slip, whereas in the velocity-weakening model (where the velocity or slip rate changes the stress on the fault), the stress is some function of slip rate. The weakening of the stress in the above models can be caused by changes in material property, dynamic effects, asperities, etc. The actual variation of stress as a function of slip is not important in our analysis; the only requirement is that the stress should drop as the slip increases. Since earthquakes involve a stress drop and physically this stress drop cannot be instantaneous, we can expect earthquake behavior to be governed by either of the two models, henceforth referred to as the stress relaxation models.

3.2 Energy Budget of Earthquakes

We can use either of the two models described above to understand the earthquake process and the energy budget of earthquakes. Figure 3.4 is a schematic representation of the partitioning of energy in earthquakes. Here, the earthquake is viewed as a stress-release process where the shear stress on the fault drops from an initial stress before the earthquake, σ_0, to a final stress after the earthquake, σ_1, over a critical slip of D_c. During the stress relaxation, the stress on the fault varies as a function of slip as given by σ_f and is shown by the dark curve in figure 3.4. When the fault slip exceeds the critical slip, the frictional stress remains constant and is equal to the final stress. Since this is a macroscopic representation of the earthquake process, the critical slip is an average value over the fault plane. The average slip (displacement) on the fault plane is given as $\overline{D}$. The difference $\Delta\sigma_s = (\sigma_0 - \sigma_1)$ is the static stress drop (mentioned earlier) and the dynamic stress drop is defined as $\Delta\sigma_d = (\sigma_0 - \overline{\sigma}_f)$, where $\overline{\sigma}_f = \frac{1}{\overline{D}}\int_0^{\overline{D}} \sigma_f(u)\,du$ is the average frictional stress on the fault [*Kanamori and Heaton*, 2000].

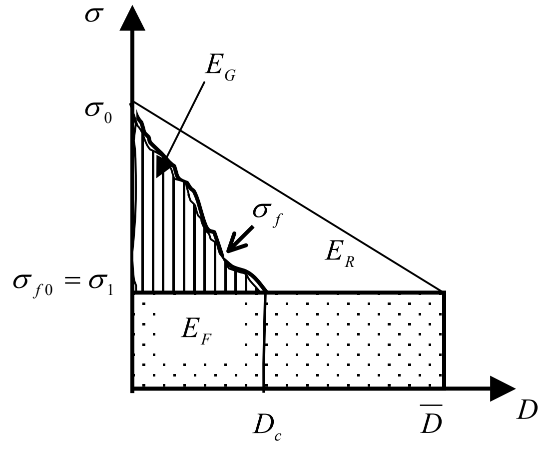

Figure 3.4 Schematic representation of the partitioning of energy in earthquakes. The dark line shows the variation of frictional stress on the fault as a function of slip. The striped region represents the fracture energy, while the stippled region represents the frictional energy for the model. Other symbols are explained in the text.

During this stress relaxation process, the total potential energy (strain energy + gravitational energy) drops from W to $W - \Delta W$, and the total potential energy change in an earthquake is given as $\Delta W = \overline{\sigma}\,\overline{D}\,S$ [*Knopoff*, 1958; *Dahlen*, 1977; *Kostrov*, 1974], where the average stress during faulting, $\overline{\sigma} = (\sigma_0 + \sigma_1)/2$, $\overline{D}$ is the average displacement during the earthquake and S is the rupture area. A part of the total potential energy is dissipated on the fault plane and is given as $\overline{\sigma_f}\,\overline{D}\,S$, where $\overline{\sigma_f}$ is the frictional stress on the fault plane. The remaining part is radiated as seismic waves and the wave energy is known as radiated energy (E_R). Using the specific stress relaxation model shown in Figure 3.4, the dissipated energy on the fault plane can be separated into fracture energy (E_G) and frictional energy (E_F), i.e., $\overline{\sigma_f}\,\overline{D}\,S = E_G + E_F$. Thus, the total potential energy change can be written as

$$\Delta W = E_R + E_G + E_F \ , \qquad \textbf{(3.10)}$$

while the radiated energy, can be written as

$$E_R = \frac{(\sigma_0 + \sigma_1)}{2}\overline{D}S - \overline{\sigma}_f\,\overline{D}S \qquad \textbf{(3.11)}$$

Thus, the area under the trapezium in Figure 3.4 represents the total potential energy released in an earthquake, ΔW. The radiated energy, as given by equation (3.11), is the unshaded area. The frictional energy represented by the stippled area is given as:

$$E_F = \sigma_{f0}\overline{D}\,S \qquad \textbf{(3.12)}$$

The fracture energy given by equation (3.9) (with the residual frictional stress $\sigma_f = \sigma_{f0}$) is thus the area of the striped region. While fracture energy is the energy that is used in mechanical processes (other than frictional heating) on the fault zone as the rupture propagates, frictional energy is the energy dissipated as heat on the fault plane. Thus, Figure 3.4 is a schematic representation of the partitioning of energy in earthquakes.

This model, though simple at first glance, is general enough and includes all the essential features of partitioning of energy in earthquakes.

3.3 Radiation Efficiency

Since $M_0 = \mu \overline{D} S$, we can write the energy-to-moment ratio of an earthquake as

$$\frac{E_R}{M_0} = \frac{E_R}{\mu \overline{D} S} = \widetilde{e} \qquad \textbf{(3.13)}$$

The efficiency of an earthquake is defined as ratio of the radiated seismic energy to the total potential energy released in the earthquake, i.e., $\eta = E_R / (E_R + E_G + E_F)$. From seismology alone, we cannot determine the absolute level of stress ($\sigma_0 \text{ or } \sigma_1$) [*Orowan*, 1960] on the fault because earthquakes are only related to the change in stress. Since frictional energy depends on the absolute level of frictional stress on the fault, we cannot determine frictional energy from seismic data alone. Consequently, the efficiency of an earthquake cannot be determined from seismology. However, we can use seismic waves to estimate radiated seismic energy and use the radiated energy-to-moment ratio as shown below to determine the radiation efficiency, which is the ratio of radiated seismic energy to the sum of radiated energy and fracture energy. Here, we are only concerned with the triangle in Figure 3.4, and the frictional energy, which is the area of the rectangle, is not part of this discussion. From Figure (3.4), we can write radiation efficiency, η_R, as [*Husseini*, 1977]

$$\eta_R = \frac{E_R}{E_R + E_G} = \frac{E_R}{(\sigma_0 - \sigma_1) DS/2} \qquad \textbf{(3.14)}$$

From (3.2), and (3.3), we obtain

$$\eta_R = \frac{2\mu \widetilde{e}}{\Delta\sigma_s}, \qquad \textbf{(3.15)}$$

where $\Delta\sigma_S = (\sigma_0 - \sigma_1)$ is the static stress drop and is the difference between the initial and final stresses on the fault. Hence, η_R, the radiation efficiency, gives the maximum efficiency of an earthquake. *Husseini* [1977] used this formulation to determine radiation efficiency, but due to the poor data quality available at the time, robust estimates of radiated energy were not possible and the study did not progress further.

In the actual earthquake process, we cannot distinguish between fracture energy and frictional energy; they both contribute to the energy dissipated in the fault zone. A part of the fracture energy may eventually be dissipated as heat on the fault. Also, the variation of stress during faulting can be quite complex; stress could increase after rupture or there could be overshoot where stress decreases to a level below the residual frictional level ($\sigma_1 < \sigma_{f0}$). The effect of these models will be considered in Chapter 4. However, the simple model shown above captures the essence of the problem and can be used to obtain insights into the earthquake mechanism.

3.4 Rupture Speed and Fracture Energy

Fracture energy, E_G, as described in the partitioning of energy in earthquakes is an integrated parameter that can be determined from the macroscopic seismic parameters, radiated energy, seismic moment and static stress drop (as shown above). Also, E_G can be determined from rupture speed, V, since the energy release rate, G, for a crack growing with a rupture speed, V, can be given as [*Kostrov*, 1966; *Eshelby*, 1969; *Freund*, 1972b]:

$$G = G^* g(V), \qquad \textbf{(3.16)}$$

where $g(V)$ is the universal function of the rupture speed for a given mode of crack propagation. Thus, fracture energy can be written as

$$\begin{aligned} E_G &= \int_S G dS = \int_S G^* g(V) dS \\ &= g(V) \int d(\Delta W_0) = g(V)(E_G + E_R) \end{aligned}$$

Here, $\Delta W_0 = (\sigma_0 - \sigma_f)\overline{D}S/2 = E_G + E_R$. Thus, we can write

$$E_G = \frac{g(V)}{1 - g(V)} E_R \qquad \textbf{(3.17)}$$

For a Mode I (tensile) crack [*Freund*, 1972a]

$$g(V) = 1 - V / c_R \,, \qquad \textbf{(3.18a)}$$

for a Mode II (longitudinal shear) crack [*Fossum and Freund*, 1975]

$$g(V) = (1 - V / c_R) / \sqrt{1 - V / c_S} \,, \qquad \textbf{(3.18b)}$$

and for Mode III (transverse shear) crack [*Kostrov*, 1966; *Eshelby*, 1969],

$$g(V) = \sqrt{\frac{1 - (V / c_S)}{1 + (V / c_S)}} \qquad \textbf{(3.18c)}$$

c_R is the Rayleigh wave speed and c_S is the shear wave speed.

The relationship between rupture speed and fracture energy can also be understood in terms of the energy budget. From the energy budget, the fracture energy is

$$E_G = \Delta W_0 - E_R \qquad \textbf{(3.19)}$$

The radiated energy scales as [*Mott*, 1948, *Lawn*, 1993]

$$E_R = k\left(\frac{V}{c_L}\right)^2 \Delta W_0 \,, \qquad \textbf{(3.20)}$$

where c_L is the limiting rupture speed (Rayleigh wave or shear wave speed).

Combining (3.19) and (3.20), we obtain

$$\left(\frac{V}{c_L}\right)^2 = \frac{1}{k}\left(1 - \frac{E_G}{\Delta W_0}\right) \qquad \textbf{(3.21)}$$

Thus, $\left(\frac{V}{c_L}\right)$ can be still used as a measure of $\left(1-\frac{E_G}{\Delta W_0}\right)$. Here, E_G is not necessarily the crack tip energy loss; it is just the energy that is not radiated and not dissipated in frictional heating on the fault. Equation (3.21) is similar to the following equation for Mode III cracks,

$$1-g(V)=\left(1-\frac{E_G}{\Delta W_0}\right), \tag{3.22}$$

in which E_G is the energy needed to create new crack surfaces. Thus, even from simple energy considerations, we can see that fracture energy and rupture speed are related.

If we use equation (3.17) and equation (3.18), we can determine the radiation efficiency as a function of the ratio of rupture speed to the limiting rupture speed (V/c_L). Thus,

$$\eta_R=\frac{E_R}{E_R+E_G}=1-g(V) \tag{3.24}$$

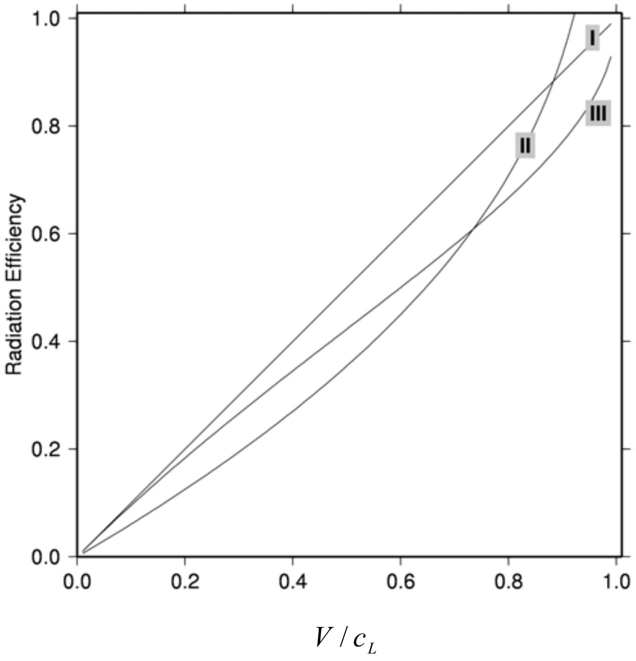

Figure 3.5 A plot of radiation efficiency as a function of the ratio of rupture speed to the limiting rupture speed for Mode I, Mode II and Mode III cracks.

Thus, both crack theory and simple energy considerations can be used to relate fracture energy to rupture speed.

3.5 Conclusions

The crack model as well as the frictional sliding model relate the fault slip to the frictional stress on the fault and are hence equivalent. They are different in the way in which they view the rupture process–in the crack model, a characteristic surface energy per unit area is required for crack extension, while in the frictional sliding model, the fault has to slip a critical slip, D_c, before unstable sliding begins at a constant friction. Both models can be used to understand the earthquake process; the frictional sliding model probably gives us a greater intuition into the earthquake process, and hence it provides us with a useful framework to view earthquakes.

By using either of these stress relaxation models we can understand the partitioning of energy in earthquakes and hence relate the macroscopic parameters such as radiated energy, seismic moment, and static stress drop to radiation efficiency and fracture energy. Since fracture energy is directly related to the physical processes on the fault zone, this parameter can be used to understand the dynamics of faulting. Moreover, both crack theory and simple energy considerations can be used to relate fracture energy to rupture speed. As rupture speed is macroscopic parameter that can be determined independently from seismic data, this parameter can also be used to understand rupture dynamics. Additionally, the comparison between the estimates of radiation efficiency and rupture velocity determined from data and the theoretically expected values of these parameters for different modes of crack propagation would be indicative of the overall validity of the proposed stress relaxation models. We will discuss this in greater detail in Chapter 4.

CHAPTER 4

Macroscopic Seismological Parameters of Subduction Zone Earthquakes

4.1 Introduction

Subduction zones, regions on the earth where one plate slides beneath another, host a whole suite of earthquakes–interplate, tsunami, intraplate, and deep earthquakes. The different types of subduction zone earthquakes have differences in the frequency content of the seismic energy released. For example, tsunami earthquakes [*Kanamori*, 1972; *Polet and Kanamori*, 2000] occur in the shallow portions of the subduction zone. They produce relatively minor shaking, but are followed by destructive tsunamis that are much larger than expected from the seismic moment magnitude of the earthquakes. Compared to ordinary subduction zone earthquakes, tsunami earthquakes are deficient in high-frequency energy; however, they have a significant amount of energy at long periods. Are these differences between tsunami earthquakes and regular plate-interface earthquakes due to differences in the rupture mechanisms of these earthquakes? To investigate this and to understand the rupture mechanics of the different types of subduction zone earthquakes, we use macroscopic source parameters–radiated seismic energy, seismic moment, rupture area and rupture velocity. The advantage of using such macroscopic parameters is that they reflect the overall frictional conditions on the fault [*Kanamori and Heaton*, 2000]; we do not have to determine the details of the rupture processes on the fault plane.

In this chapter, we compute teleseismic estimates of radiated energy for 23 large subduction zone earthquakes; most of these earthquakes have $M_w > 7.5$, but we also included some smaller well-studied subduction zone earthquakes. For comparison, we include 6 crustal earthquakes. We also compiled the static stress drop estimates for these 29 earthquakes from literature. From the seismic moment, radiated energy and static stress drop values, we calculate the radiation efficiency for these earthquakes and interpret our results in the light of differences in rupture mechanisms.

4.2 Different Types of Subduction Zone Earthquakes

Depending on the location of the earthquakes relative to the subducting slab, we classified subduction zone earthquakes as shown in Figure 4.1: 1) Plate interface (interplate) earthquakes, which occur at the interface between the overlying plate and the subducting plate (i.e., typical subduction zone earthquakes); 2) Tsunami earthquakes, which occur at shallow depths in the slab and produce tsunamis much larger than are expected from their seismic moment magnitude; 3) Crustal earthquakes (not shown in the figure), which occur in continental crust (included because many of them are well studied using regional arrays and hence serve as useful and important comparisons); 4) Downdip earthquakes–in this category we group earthquakes that rupture downwards along the dip of the subducting slab (such as the 1994 Sanriku earthquake) and also earthquakes that rupture the bottom portion of the known seismogenic zone (like the 1997 Kamchatka earthquake); 5) Intraplate earthquakes, which occur within the subducting slab at depths less than 250 km [*Gutenberg and Richter*, 1938, 1939]; 6) Deep earthquakes, which occur within the subducting slab at depths greater than 500 km [*Gutenberg and Richter*, 1938, 1939].

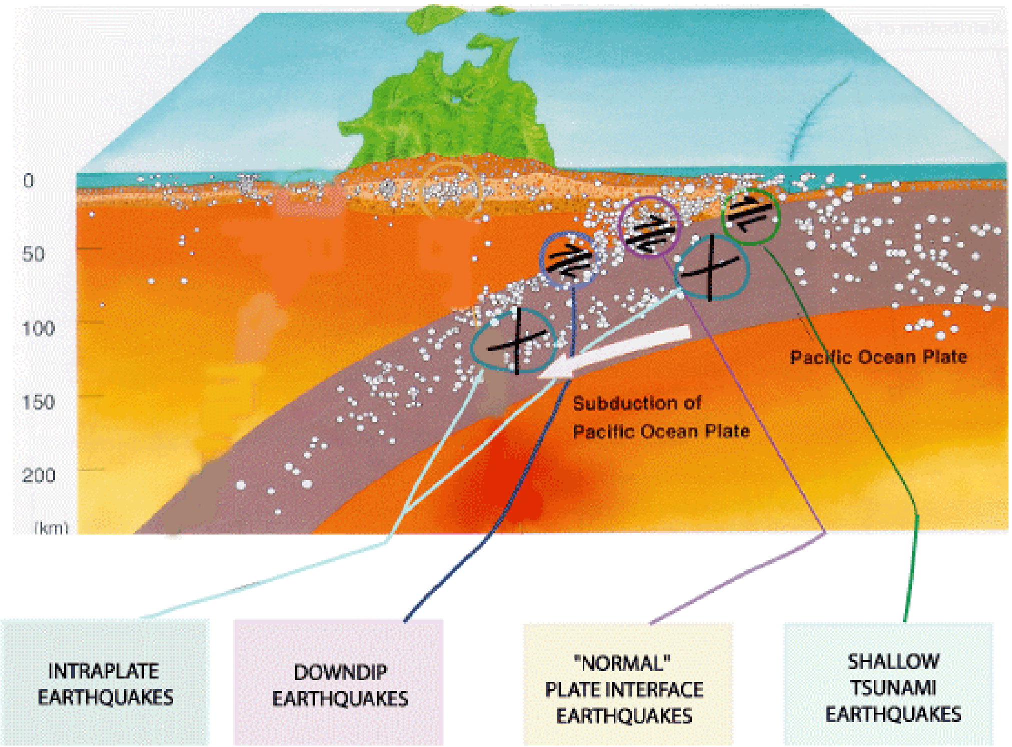

Figure 4.1 Cartoon showing the location of the different types of subduction zone earthquakes relative to the subducting slab (*Science and Technology Agency, Japan,* written permission, 2002).

4.3 Radiated Energy of Subduction Zone Earthquakes

To estimate the radiated seismic energy from 23 well-recorded subduction zone earthquakes that occurred between 1992 and 2001 (shown on the location map in Figure 4.2), we used *P* wave teleseismic data recorded at broadband stations around the world and archived at the IRIS Data Management Center. Only the vertical component data (BHZ channel) of stations at distances between 30^0 and 90^0 were used in this study. We applied corrections to the integrated velocity squared spectrum to determine the moment rate spectra [*Boatwright and Choy*, 1986]. The details of the corrections are described in section 2.1, but we briefly mention a few important points here. Since we are interested in understanding the differences between different types of subduction zone earthquakes, we included shallow as well as deep events in our study. For shallow events, the depth phases cannot be separated from the direct phase, so the

P wave group as a whole is used to compute radiated energy; for deeper events, only the direct *P* wave is used.

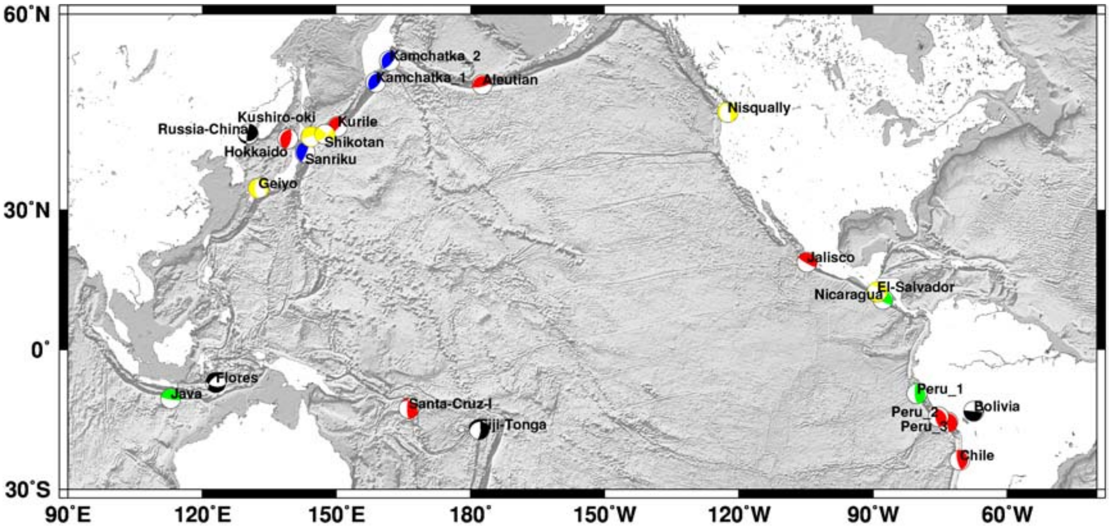

Figure 4.2 Map showing the location and focal mechanism of 23 large (mostly $M_w > 7.5$) subduction zone earthquakes studied here. Plate interface earthquakes, i.e., interplate earthquakes are shown in red; tsunami earthquakes are shown in green; downdip earthquakes are shown in blue; in yellow are shown intraplate earthquakes and deep earthquakes are in black.

The effect of directivity on radiated energy estimates depends on the slip model and station distribution (see Chapter 2). Given a slip model of an earthquake, we can calculate the actual total radiated energy and the average single-station energy estimates for a particular station distribution; the ratio of these two estimates would be representative of the directivity effect of the earthquake for the given slip model and station distribution. Thus, we can use this ratio to correct the average of the single-station energy estimates determined from data for directivity. By using this method, the actual radiated energy would still be determined from the data and the correction is only a factor that is applied to this observed estimate; thus, the actual details of the slip model will not significantly affect the estimate of radiated energy. Using the above method and slip models from literature, we calculated the directivity corrections for a few large earthquakes (Table 2.1). For example, for the January 15, 1993, Kushiro-oki earthquake, the actual total energy from the slip model is 4.47 x 10^{16} J and the average of the single-station estimates for this slip model and for a particular station distribution (similar to the one used to compute single-station energy estimates from data) is 6.55 x 10^{16} J, hence, the directivity correction is only 0.68. From our computations, we observe that the directivity corrections for dip-slip earthquakes with rupture along strike, alter the teleseismic energy estimates by less than a factor of two, hence, we do not include these corrections in our final estimates of teleseismic energy from subduction zone earthquakes. For comparison, we also include some well-studied crustal earthquakes in our study. As directivity could have a significant effect on the teleseismic radiated energy estimates of crustal strike-slip earthquakes, for these earthquakes we include corrections for directivity obtained using slip models when such models are available.

Figure 4.3 shows the single-station teleseismic estimates of radiated energy for 23 subduction zone earthquakes and 4 crustal earthquakes. The radiated energy for the January 17, 1994, Northridge earthquake is the regional estimate obtained from *Hiroo Kanamori* [written communication, 2002], and the radiated energy for the October 16, 1999, Hector Mine earthquake was determined as shown in the Chapter 2. The first plot for each earthquake shows the single-station energy estimates at the individual stations where the stations are arranged in order of increasing radiation pattern. For each earthquake, we used only those stations that had good data quality (high signal-to-noise ratio); some subjective judgement was used to evaluate data quality. We also eliminated stations where the radiation pattern coefficient is less than 0.2 as the small amplitude of the *P* wave at these nodal stations results in low signal-to-noise ratios; moreover, the arrival of scattered energy at these stations could potentially bias the energy estimates. The second plot for each earthquake shows the azimuthal distribution of the selected stations. Below each plot, we include a brief description of the earthquake highlighting the important characteristics. From Figure 4.3 we observe that several earthquakes in the Southern hemisphere and a few earthquakes in other regions of the world have poor azimuthal station distribution; however, since most the earthquakes have a dip-slip mechanism with rupture propagating along strike, the directivity effects are small and hence the poor station distribution should not significantly affect the average of the single-station energy estimates.

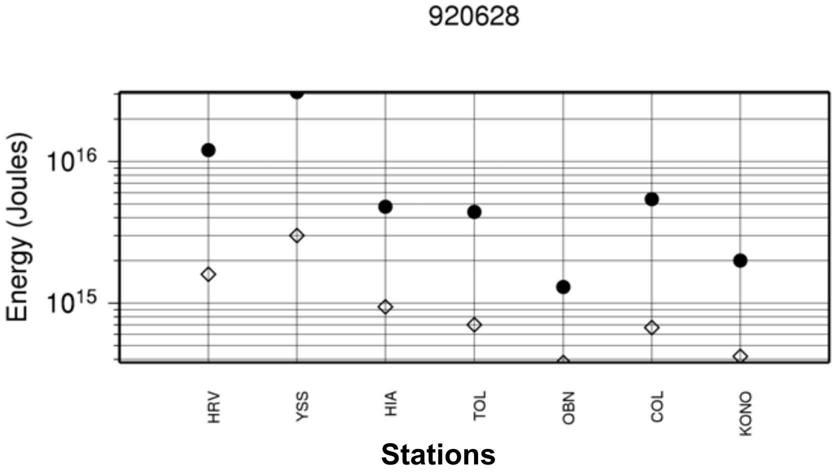

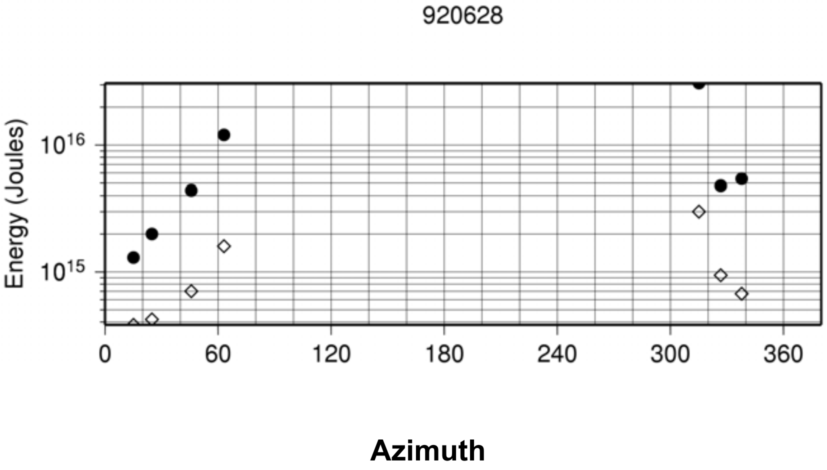

920628, Landers (Type 3): depth=7 km, mean E_R = 0.86 x 10^{16} J, directivity corrected E_R = 0.26 x 10^{17} J, V = 2.9 km/s (0.8 β) [Dreger, 1994]. The Landers, California earthquake, M_0=1.1 x 10^{20} Nm, was vertical strike-slip earthquake with a unilateral rupture propagating mostly from south to north along strike. Since this is among the oldest strike-slip events we studied, the station coverage is poor. Thus, we have a limited number of non-nodal stations with good signal-to-noise ratio; we could use only these stations to estimate the energy from teleseismic data. However, slip models for the earthquake determined by inversion of regional data result in energy estimates that are less than a factor of two smaller than the estimates from teleseismic data. Since the slip models do not account for high-frequency energy beyond 0.5 Hz, this difference between the model and data estimates is expected and also indicates that the estimates from the data are reasonable.

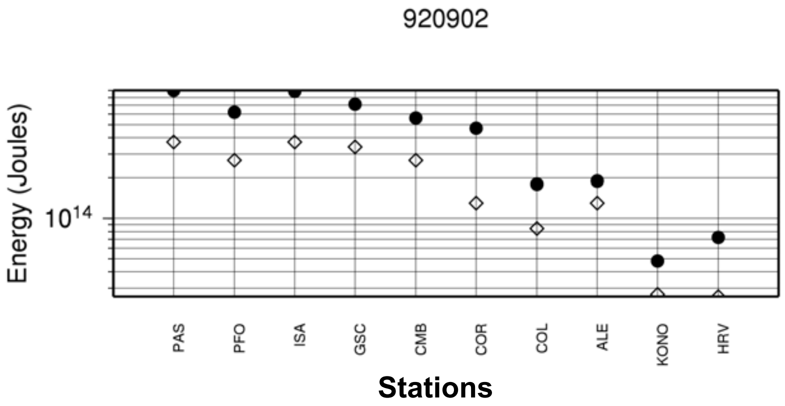

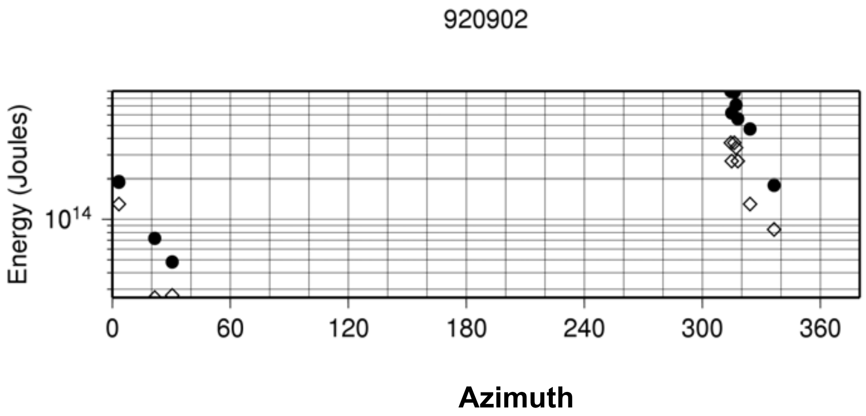

920902, Nicaragua (Type 2): depth=20 km, mean E_R = 0.43 x 10^{15} J, V = 1.0-1.5 km/s (0.34 β -0.5 β) [Kikuchi and Kanamori, 1995b]. The Nicaragua earthquake, M_0=3.1 x 10^{20} Nm, was the first tsunami earthquake to be recorded by modern broadband instruments. The observed variation in energy with station location could be due to directivity and is consistent with the observations of Kikuchi and Kanamori, [1995b], who suggest that the earthquake ruptured bilaterally to the NW and SE; moreover the rupture was faster to the NW, thus stations at azimuths close to 300^0 receive a larger amount of radiated energy. However, since the rupture velocity is small, directivity is not significant. The earthquake ruptured a shallow-dipping fault plane and the slip propagated to the ocean floor.

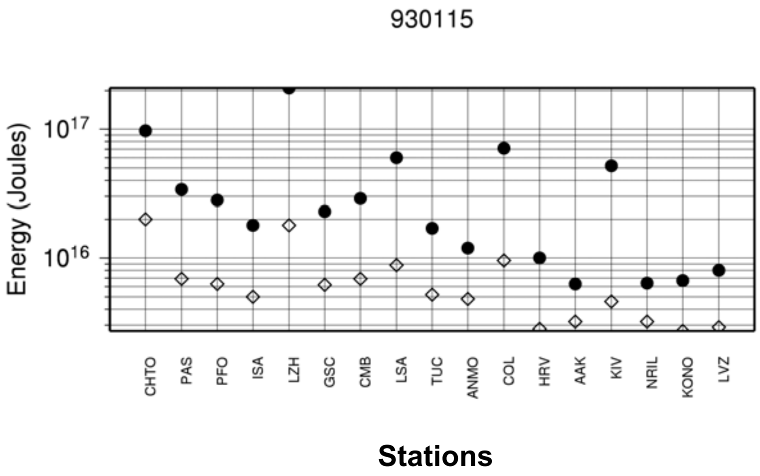

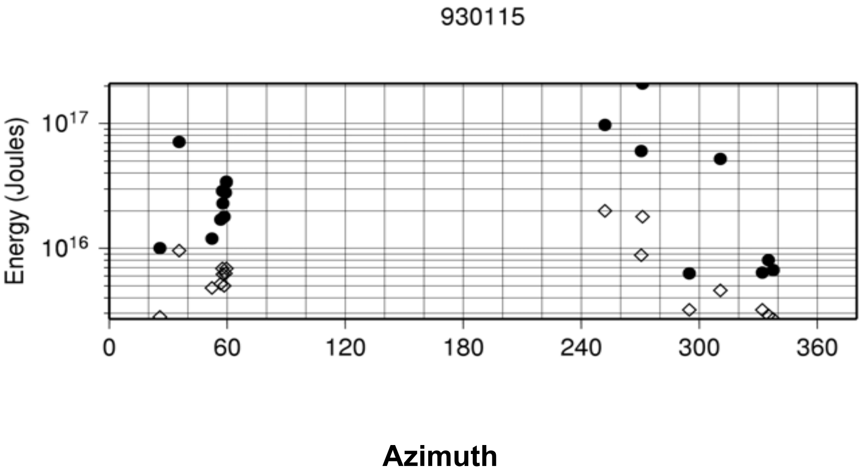

930115, Kushiro-oki (Type 5): depth=107 km, mean E_R = 0.43 x 10^{17} J, V = 3.3 km/s (0.7 β) [Kikuchi and Kanamori, 1995b; Takeo et al., 1993]. The Kushiro-oki earthquake, M_0=3.1 x 10^{20} Nm, was an intraplate earthquake that occurred off the east coast of Hokkaido, Japan (along the Kuril trench). The mechanism of the earthquake is consistent with downdip extension in the subducting slab. The earthquake ruptured a shallow-dipping plane and the rupture propagated westward [Takeo et al., 1993]. The larger estimates of energy at stations located at azimuths close to 270^0 is an effect of this directivity. Of the subduction zone earthquakes studied in this thesis, this earthquake has the largest energy-to-moment ratio.

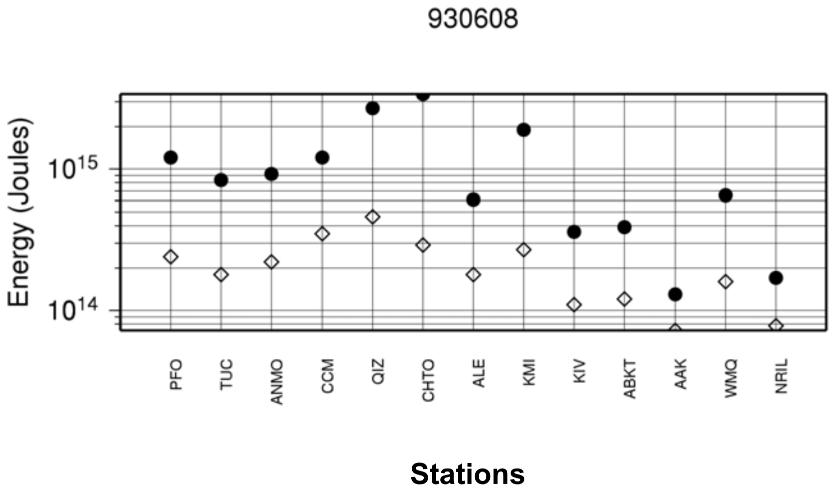

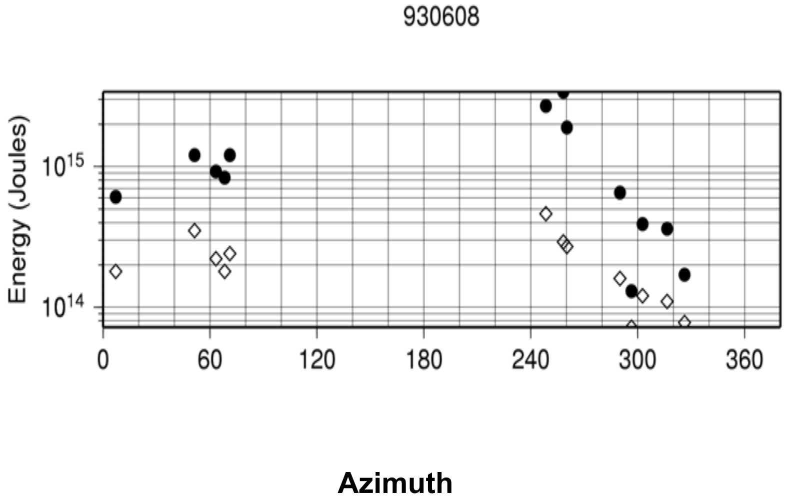

930608, Kamchatka_1 (Type 4): depth=46 km, mean E_R = 0.11 x 10^{16} J, V = 3.0 km/s–assumed not estimated (0.7 β) [Johnson et al., 1995]. The Kamchatka earthquake, M_0=2.2 x 10^{20} Nm, occurred at the downdip edge of the subduction zone off the east coast of southern Kamchatka (Kuril trench). The rupture propagated updip [Johnson et al., 1995]. The authors further suggest that the earthquake ruptured a part of the subduction zone has few moderate size earthquakes, and also that the earthquake generated a moderate tsunami despite a rupture depth of 40km. It is not clear if the event broke the ocean floor.

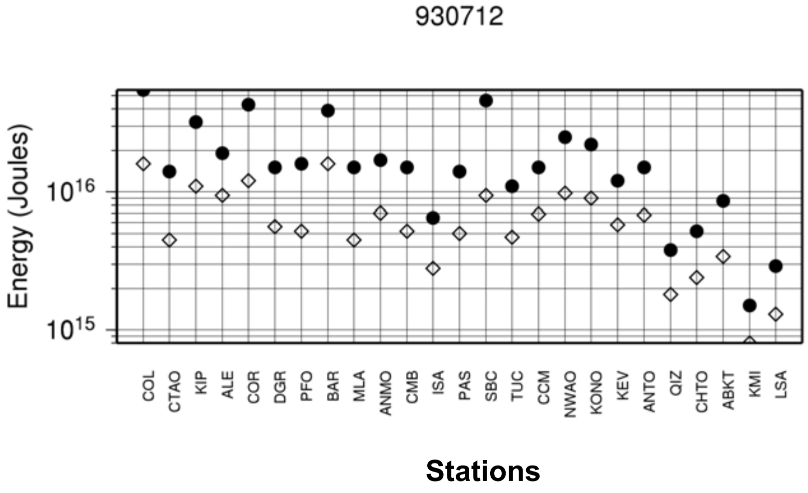

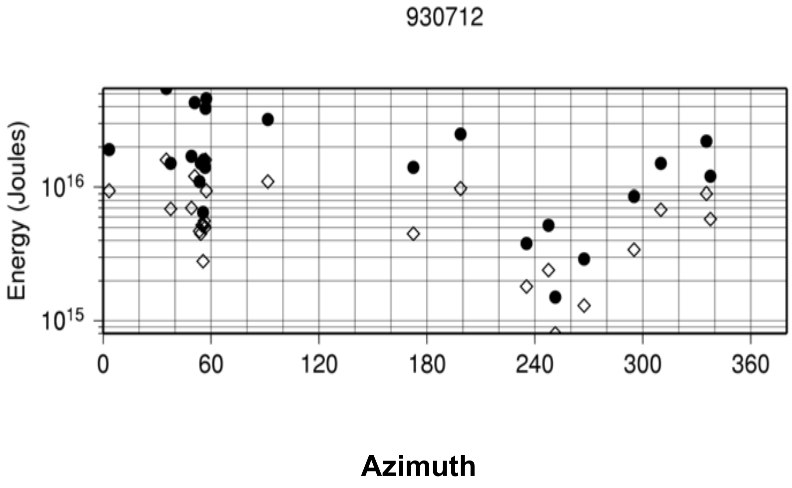

930712, Hokkaido (Type 1): depth=15 km, mean E_R = 0.18 x 10^{17} J E17 J, V = 3.0 km/s – assumed (0.8 β) [Mendoza and Fukuyama, 1996]. The Hokkaido earthquake, M_0=5.5 x 10^{20} Nm, was an interplate earthquake that occurred off the southwest coast of Hokkaido, Japan (in the sea of Japan). The rupture was complex and the focal mechanism varied over the length of the fault. The variation between the single-station estimates at the different stations could be due to directivity; however, since the rupture is complicated, a rupture direction cannot be inferred.

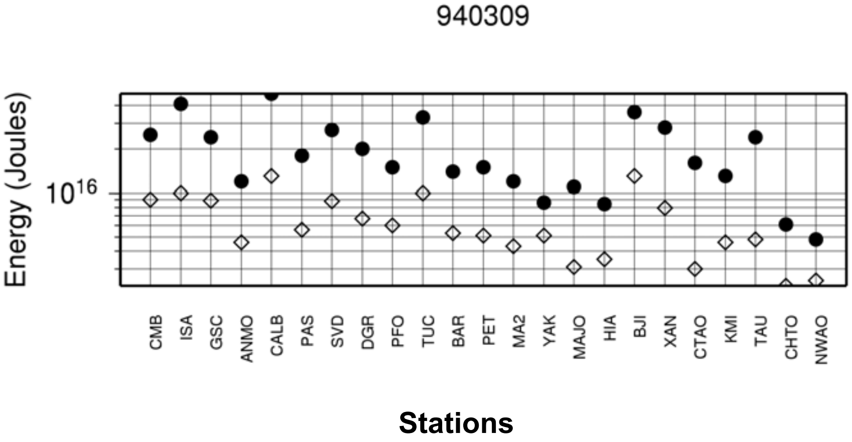

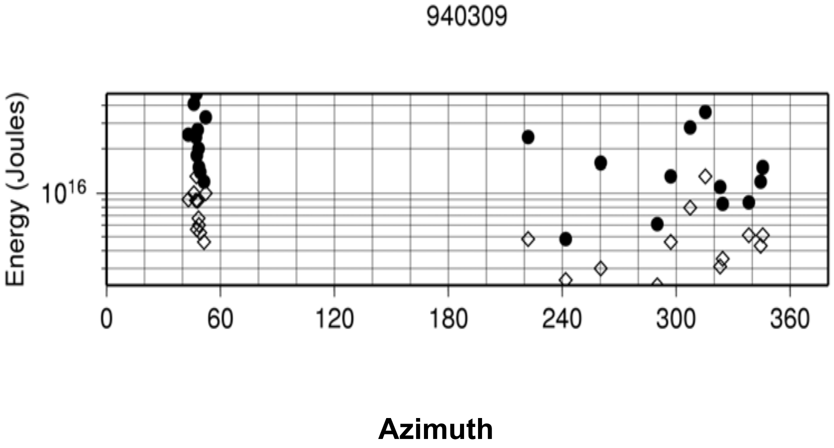

940309, Fiji-Tonga (Type 6): depth=569 km, mean E_R = 0.20 x 10^{17} J, V = 4.0-5 km/s (0.74 β -0.93 β) [Goes and Ritsema, 1995]. The Fiji-Tonga earthquake, M_0=2.8 x 10^{20} Nm, was a deep earthquake that occurred in the Fiji-Tonga subduction zone. In teleseismic recordings of deep earthquakes, the earthquake is almost like a point source; thus, the directivity is difficult to determine at teleseismic distances and the effect of directivity on energy estimates is small.

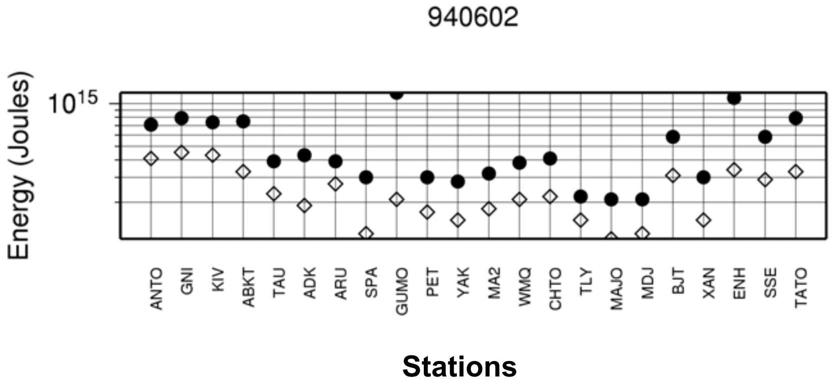

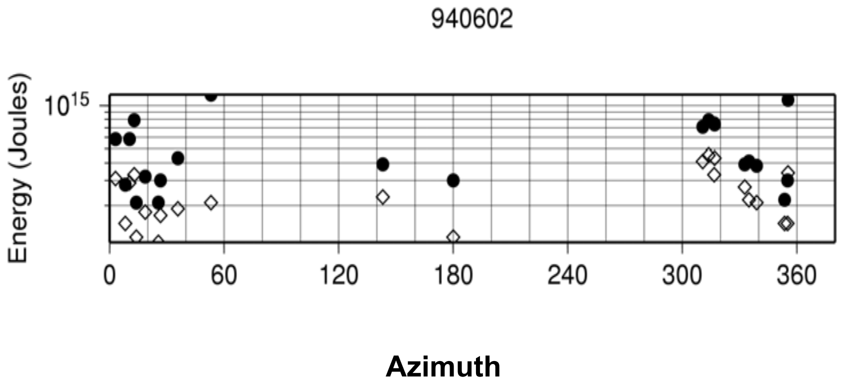

940602, Java (Type 2): depth=15 km, mean E_R = 0.51 x 10^{15} J, V < 2.0 km/s (0.6 β) [Abercrombie et al., 2001]. The Java earthquake, M_0 =6.2 x 10^{20} Nm, was a tsunami earthquake, but the details of the source process are not clear. While some studies suggest that the earthquake ruptured downdip [Abercrombie et al., 2001], because of the poor station coverage to the south and shallow slip, the rupture direction and rupture area are not well resolved. As can be observed from the above plots, we do not observe any significant directivity.

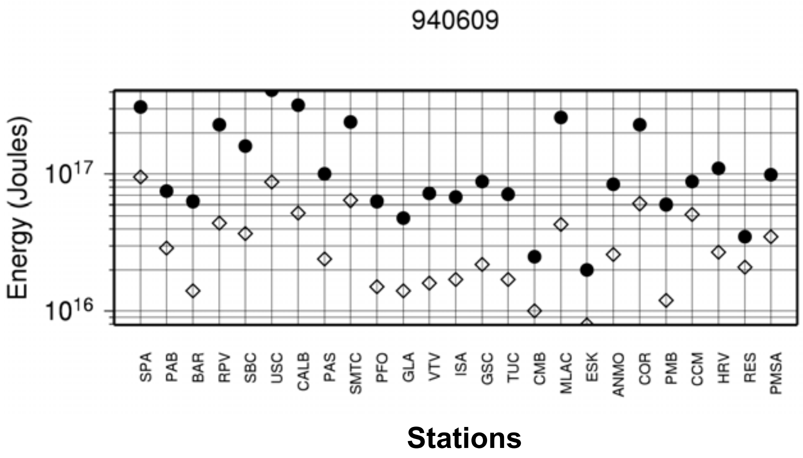

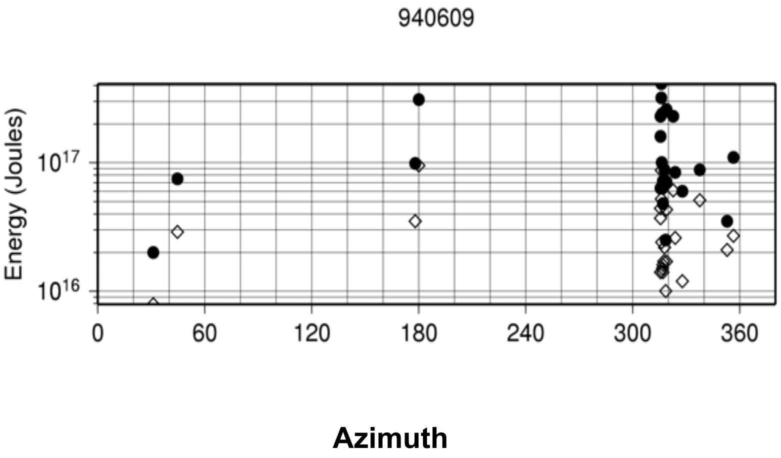

940609, Bolivia (Type 6): depth=647 km, mean E_R = 0.13 x 10^{18} J, V = 1-2 km/s (0.18 β -0.36 β) [Kikuchi and Kanamori, 1994; Goes and Ritsema, 1995]. The Bolivia earthquake, M_0=2.9 x 10^{21} Nm, was the largest deep earthquake to be recorded by modern broadband seismometers. There are few stations to the south of the earthquake and hence the azimuthal distribution of stations is poor, however, as mentioned earlier, in teleseismic recordings of deep earthquakes, the earthquake is almost like a point source and hence the effect of directivity on energy estimates is negligible. All the stations at azimuth of ~320^0 are stations in California, and the variation in the single-station energy estimates for these stations is due to site effects; however, this will not affect the average single-station estimate by more than a factor of two.

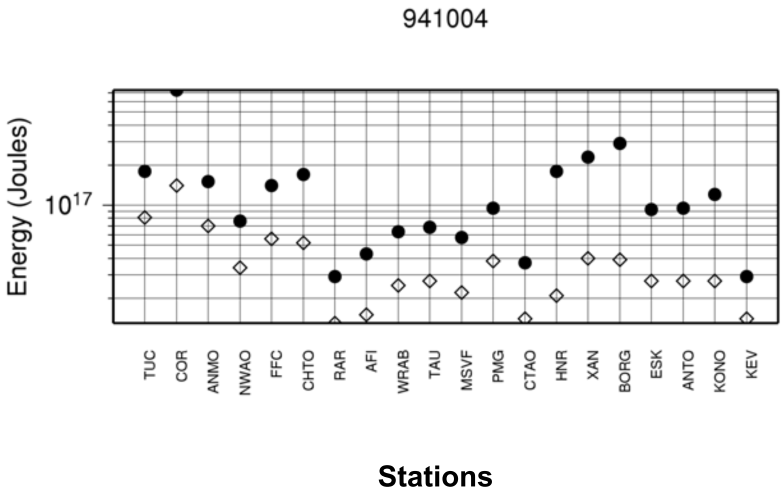

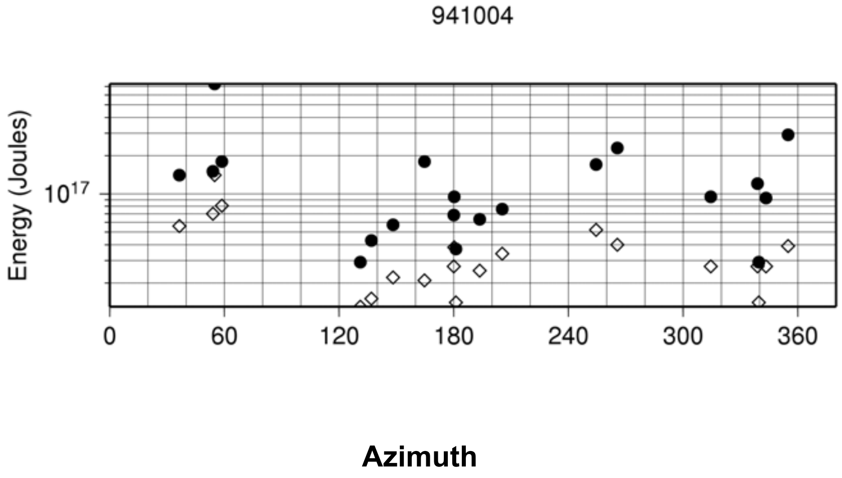

941004, Shikotan (Type 5): depth=56 km, mean E_R = 0.15 x 10^{18} J, V = 2.5 km/s (0.67 β) [Kikuchi and Kanamori, 1995a]. The Shikotan earthquake, M_0 =2.6 x 10^{21} Nm, was an intraplate earthquake that occurred off the coast of Shikotan Island, one of the Kurile Islands. The mechanism of the earthquake is consistent with downdip extension in the subducting Kurile slab. No significant directivity was observed.

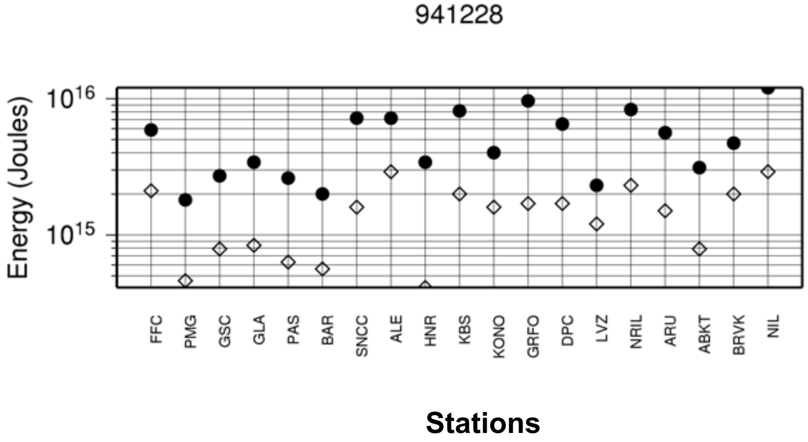

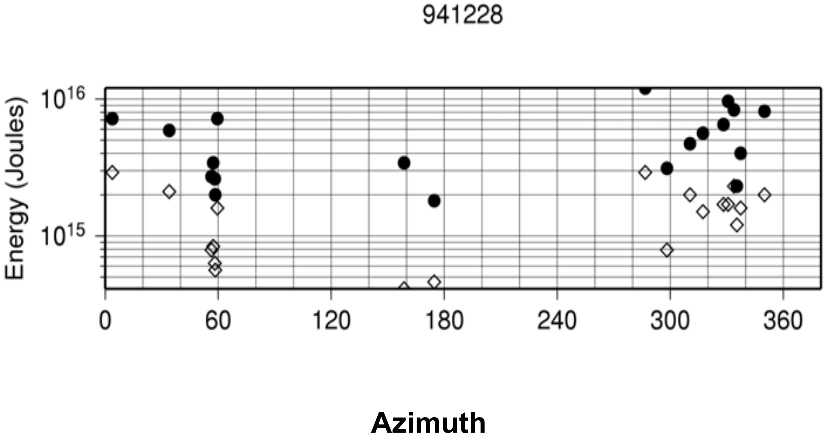

941228, Sanriku (Type 4): depth=27 km, mean E_R = 0.51 x 10^{16} J, V = 1.8-3 km/s (0.45 β -0.75 β) [Nakayama and Takeo, 1997]. The Sanriku earthquake, M_0=4.4 x 10^{20} Nm, occurred off Sanriku, Honshu, along the Japan trench. The earthquake was a thrust that ruptured the subduction interface. An unusual feature of this earthquake is that the rupture initiated at shallow depths of relatively weaker coupling and propagated downdip (to the west-northwest) [Hartog and Schwartz, 1996] and was followed by a year of after-slip [Heki et al., 1997]. Usually, large plate interface thrust earthquakes initiate at the downdip edge of the fault zone and rupture updip [Scholz, 1990].

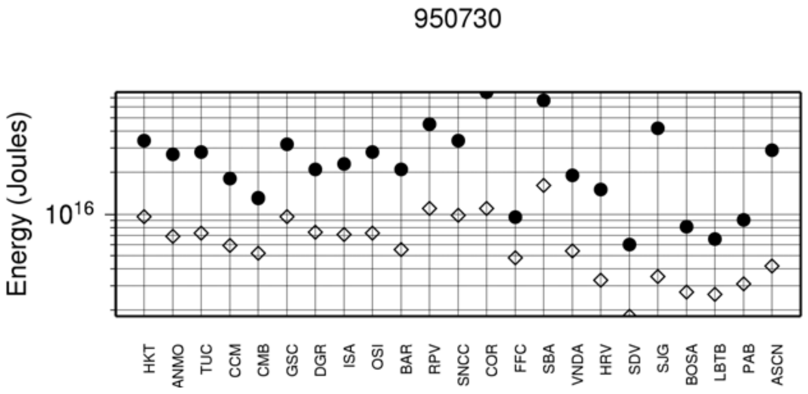

Stations

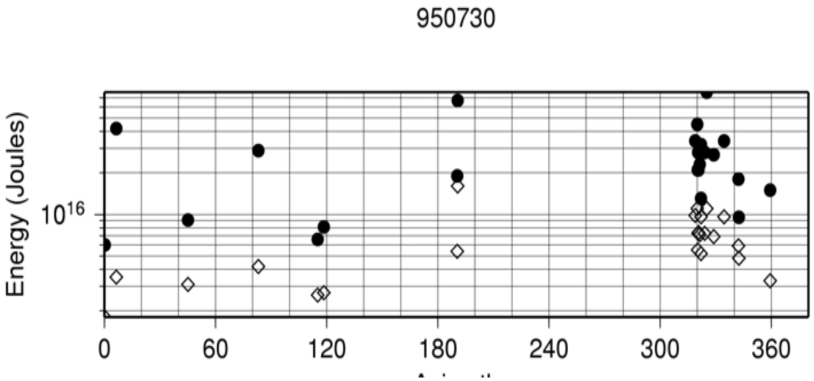

Azimuth

950730, Chile (Type 1): depth=32 km, mean E_R = 0.26 x 10^{17} J, V = 3.3 km/s (0.85 β) [Ruegg et al., 1996]. The Chile earthquake, M_0 =1.8 x 10^{21} Nm, was an interplate event that occurred along the Peru-Chile trench close to Antofagasta in Chile. The station coverage to the south of the earthquake is poor; thus, although the rupture propagated to the south, the single-station estimates of energy do not show significant directivity.

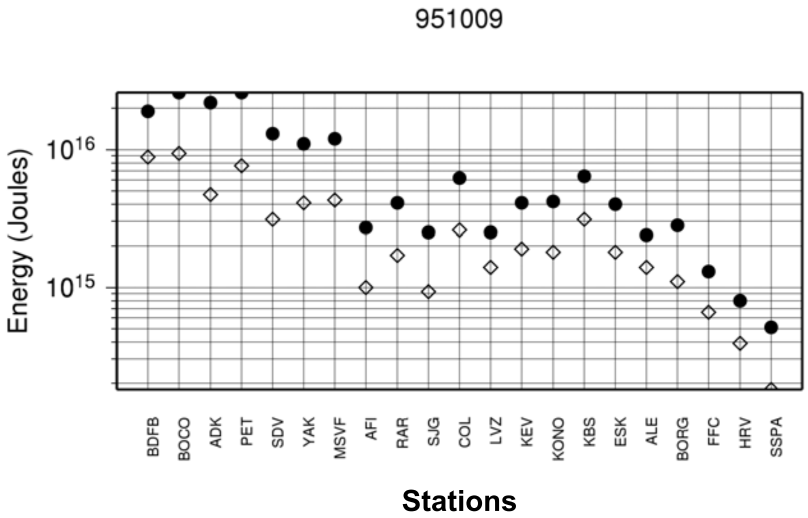

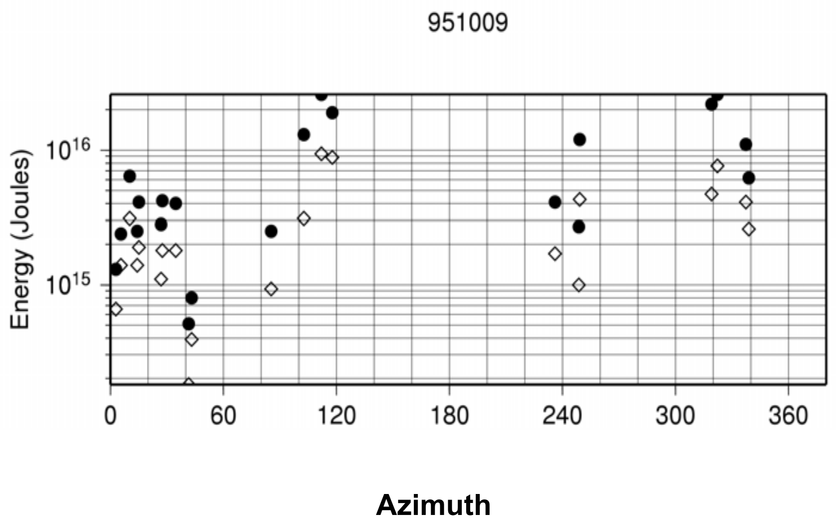

951009, Jalisco (Type 1): depth=15 km, mean E_R = 0.82 x 10^{16} J, V = 2.2-2.8 km/s (0.63β-0.8β) [Courboulex et al., 1997; Mendoza and Hartzell, 1999]. The Jalisco earthquake, M_0=1.2 x 10^{21} Nm, occurred off the coast of Jalisco, Mexico. The rupture propagated to the NW [Courboulex et al., 1997; Pacheco et al., 1997] and thus the stations at azimuths of ~300^0 have larger energy estimates due to directivity. From the figure on the left, it appears that the effect of the radiation pattern factor has not been removed. However, the strong directivity effect at these azimuths causes the energy estimates at these stations to be large. Also, the rupture is more complicated with shallow slip at depths of 8-15 km [Melbourne et al., 1997; Mendoza and Hartzell, 1999] and thus the directivity is probably more complicated. GPS studies observed post-seismic slow slip that migrated downdip to about 16 to 35 km [Hutton et al., 2001].

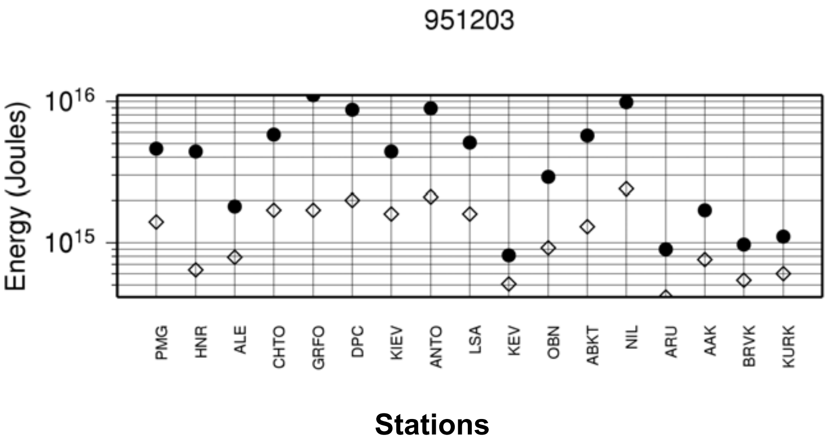

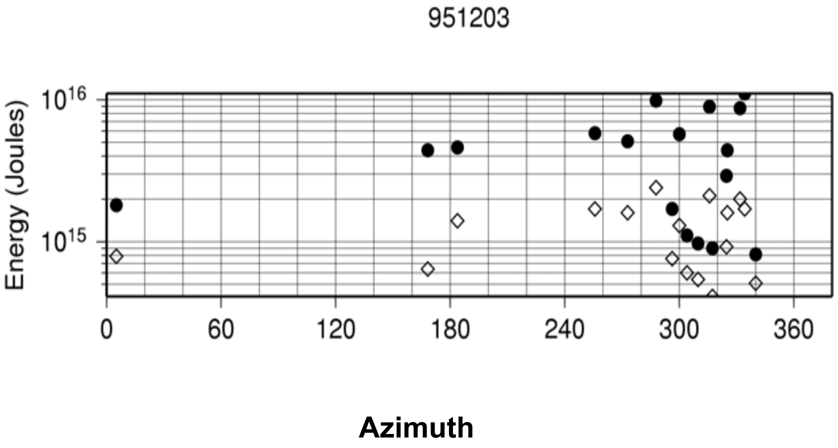

951203, Kurile (Type 1): depth=26 km, mean E_R = 0.49 x 10^{16} J, V ~ 2.5 km/s (0.7 β)[Masayuki Kikuchi, written communication, 2002]. The Kurile earthquake, M_0 =8.8 x 10^{20} Nm, occurred off Etorofu island in the western Kurile Islands. The earthquake ruptured northeast, but due to poor station coverage, we do not observe the directivity effects on the single-station energy estimates. However, since the earthquake is a thrust and the directivity is along strike, the effect of directivity would not affect the average of the single-station energy estimates by more than a factor of two (see section 2.1.1).

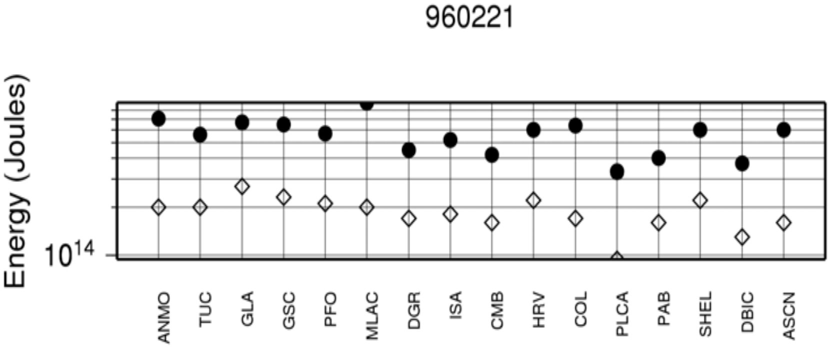

Stations

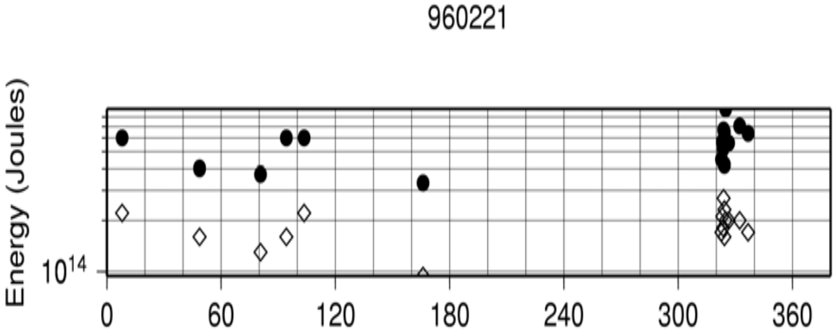

Azimuth

960221, Peru_1 (Type 2): depth=15 km, mean E_R = 0.55 x 10^{15} J, V =1.5-2 km/s (0.38 β -0.52 β)[Ihmle et al., 1998]. The Peru earthquake, M_0 =2.2 x 10^{20} Nm, occurred at a shallow depth at the interface between the Nazca and South American plates. The rupture was bilateral (along strike), hence the directivity is not significant.

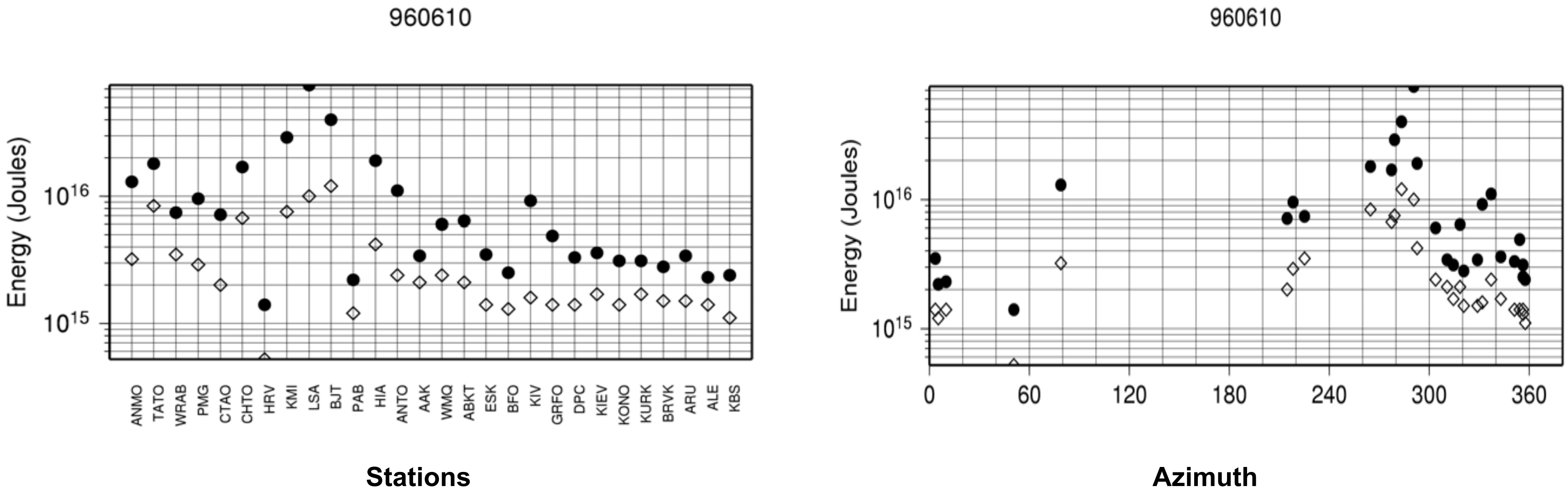

960610, Aleutian (Type 1): depth=29 km, mean E_R = 0.11 x 10^{17} J, V >2.2 km/s (0.5 β)[Kikuchi, written communication, 2002]. The Aleutian earthquake, M_0=8.8 x 10^{20} Nm, was an interplate earthquake that ruptured the western part of the Aleutian subduction zone. Some studies suggest that the rupture is bilateral [Schwartz, 1999], while others suggest a large amount of slip in the western segment of the fault [Kisslinger and Kikuchi, 1997]. The single-station estimates of energy shown in the figures above suggest some directivity at azimuths of $\sim 280^0$, but there is no clear evidence for this in the inversion results. Excluding the three stations (LSA, BJT and KMI), however, changes the average single-station energy estimates by less than a factor of two.

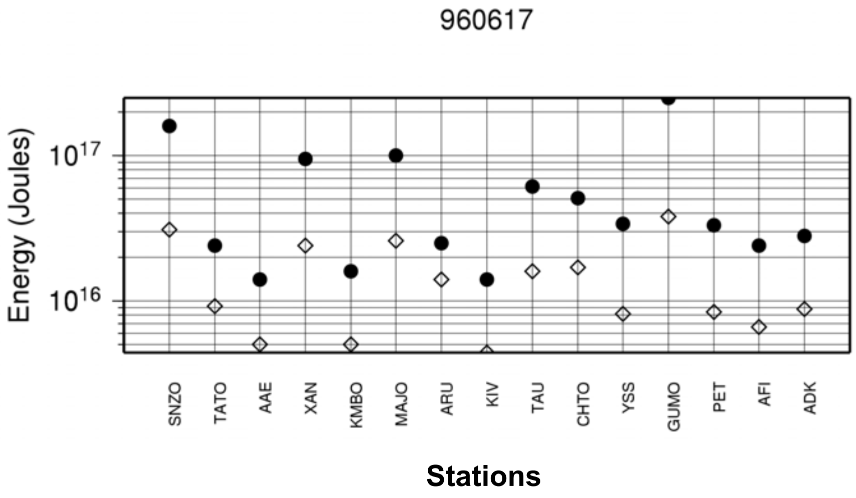

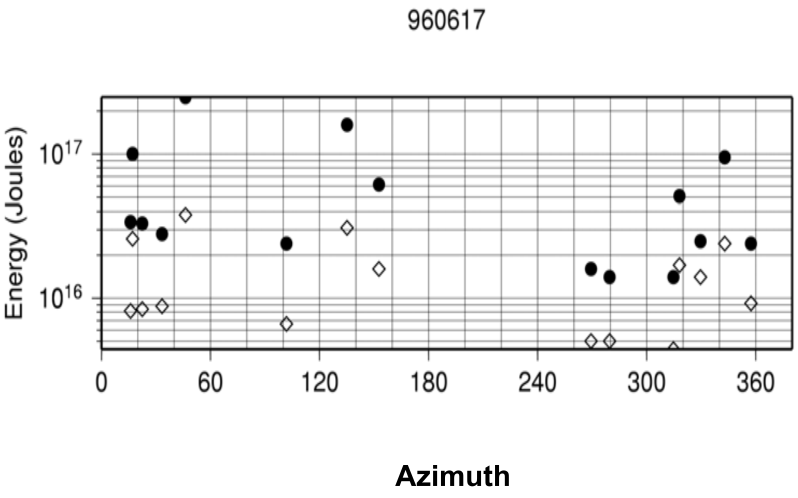

960617, Flores (Type 6): depth=588 km, mean E_R = 0.62 x 10^{17} J, V =2-4 km/s (0.37 β -0.74 β) [Goes et al., 1997]. The Flores earthquake, M_0 =7.3 x 10^{20} Nm, was a deep earthquake that occurred in the Flores Sea, located between the islands of Sulawesi and Flores; the earthquake occurred within the Indo-Australian plate that is subducting beneath the Eurasian plate. No significant directivity is observed.

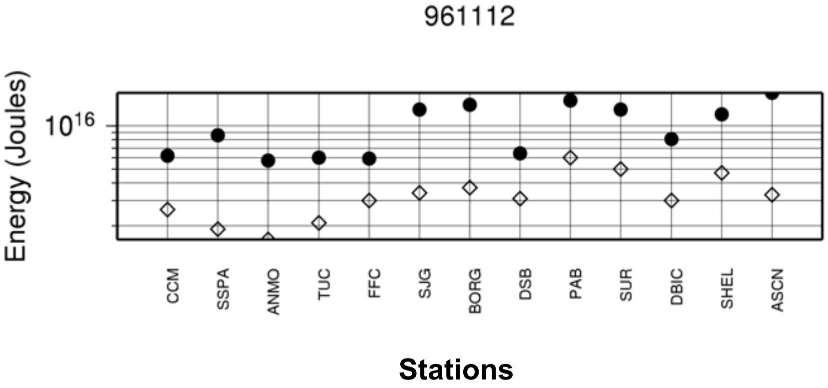

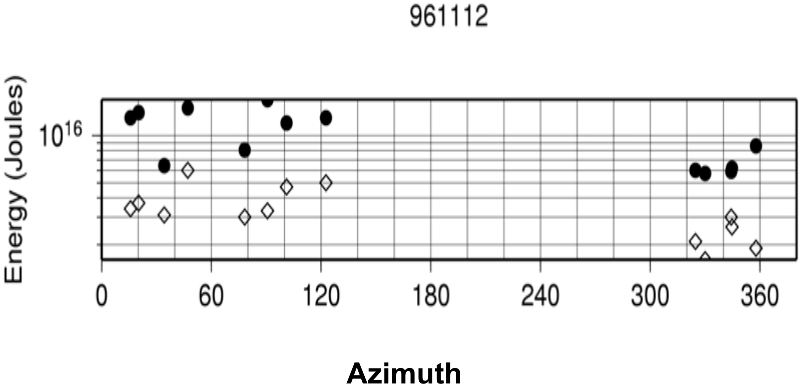

961112, Peru_2 (Type 1): depth=25 km, mean E_R = 0.10 x 10^{17} J, V =2.25 km/s (0.63 β) [Swenson and Bilek, 1999]. The Peru earthquake, M_0 =3.5 x 10^{20} Nm, is an interplate thrust that occurred in the Peru subduction zone, where the Nazca plate subducts beneath the North American plate. The rupture propagated to the southeast along strike, but it is not well observed in the single-station energy estimates plotted above.

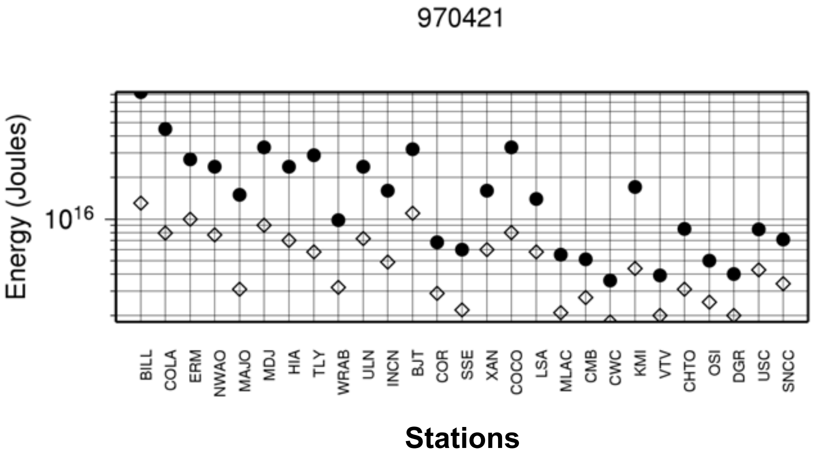

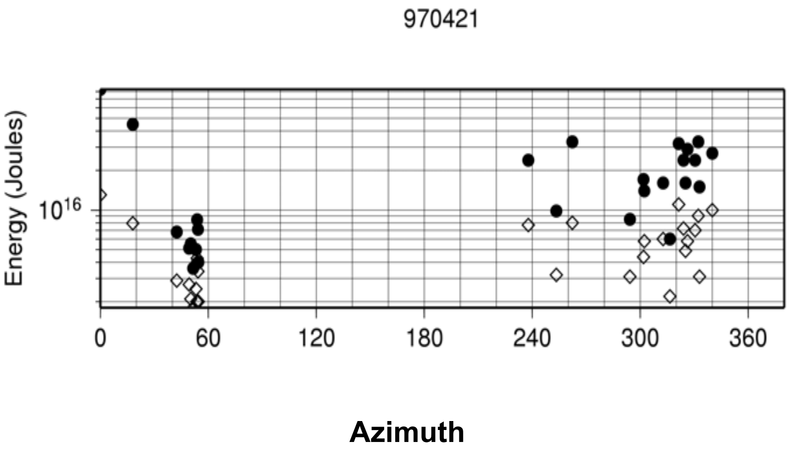

970421, Santa Cruz (Type 1): depth=30 km, mean E_R = 0.19 x 10^{17} J, V =1.9 km/s (0.48 β) [Kaverina et al., 1998]. The Santa Cruz Island earthquake, M_0=5.7 x 10^{20} Nm, was an interplate thrust in the shallow part of the New Hebrides subduction zone. The single-station energy estimates do not show strong directivity, but Kaverina et al. [1998] suggest that the rupture propagated southwest (updip). Station BILL has a large single-station energy estimate, but that is probably because the station is close to the S node and includes some scattered energy; removing this station alters the average of the single-station estimates by a very small amount (~11%).

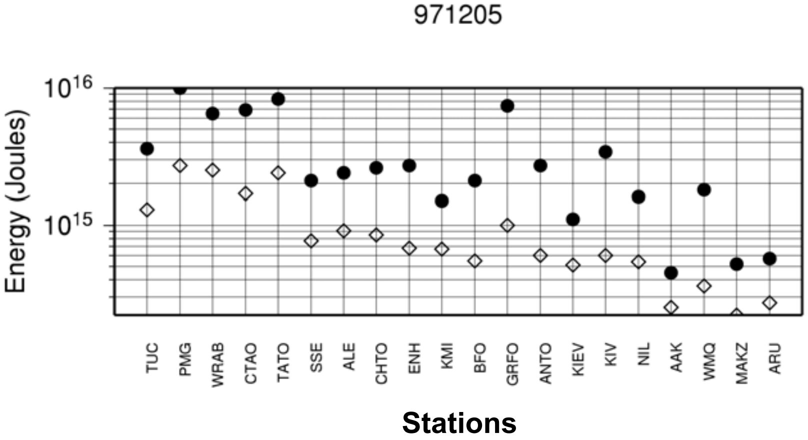

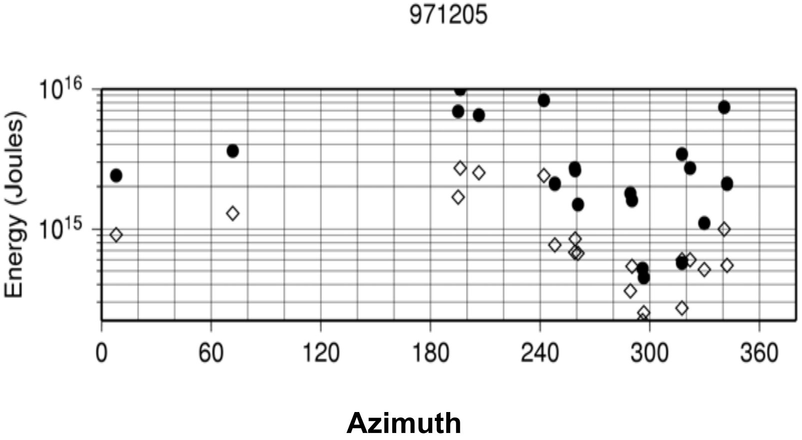

971205, Kamchatka_2 (Type 4): depth=34 km, mean E_R = 0.33 x 10^{16} J, V =2 km/s (0.45 β) [Wha, 1998]. The Kamchatka_2 earthquake, M_0 =6.2 x 10^{20} Nm, ruptured further north and at a shallower depth as compared to the 930608 Kamchakta_1 earthquake off the east coast of Kamchatka; this earthquake too ruptured the deeper portion of the seismogenic zone. The rupture propagated southwest [Wha, 1998], and hence the stations at azimuths close to 200^0 have higher single-station energy estimates.

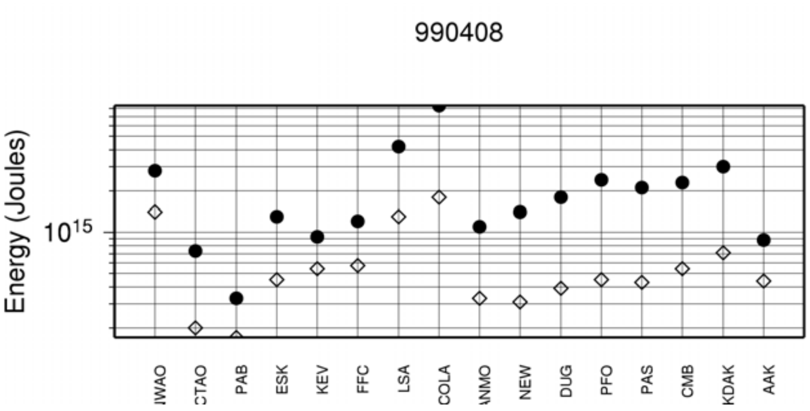

Stations

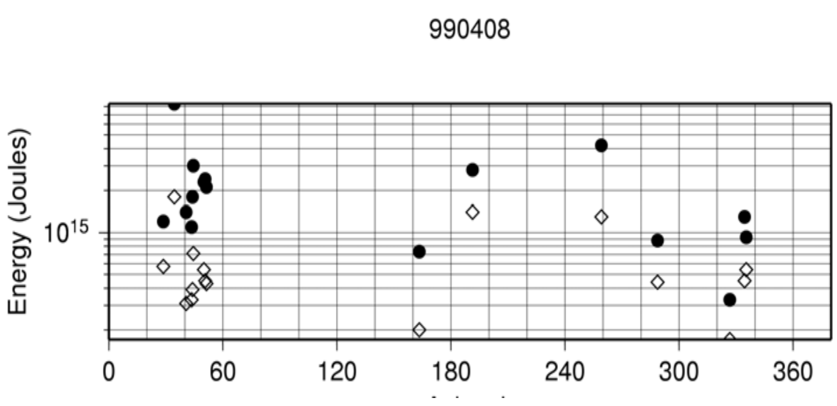

Azimuth

990408, Russia-China (Type 6): depth=564 km, mean E_R = 0.21 x 10^{16} J, V =2 km/s (0.37 β) [Martin Griffiths, written communication, 2002]. The M_0 =5.5 x 10^{19} Nm earthquake was a deep earthquake that occurred at the Russia-China border. The earthquake is like a point source and the directivity is difficult to resolve from teleseismic data [Martin Griffiths, written communication].

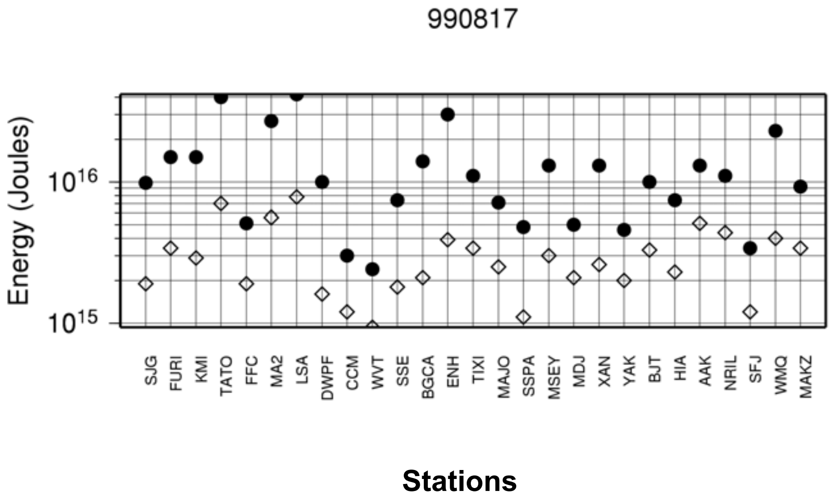

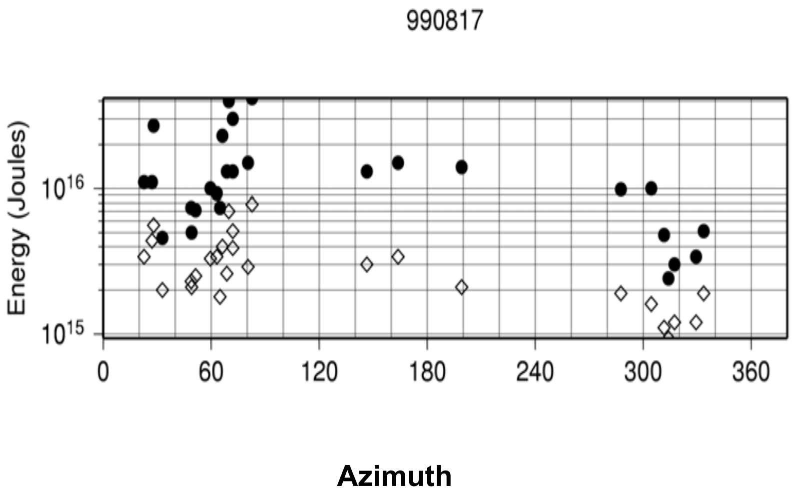

990817, Izmit (Type 3): depth=15 km, mean E_R = 0.14 x 10^{17} J, V =3 km/s (0.78 β) [Yagi and Kikuchi, 2000]. The Izmit earthquake, M_0=3.1 x 10^{20} Nm, was a strike-slip earthquake that ruptured a segment of the North Anatolian fault in northwestern Turkey. The rupture process is characterized by asymmetric bilateral rupture [Yagi and Kikuchi, 2000] and thus the effect of directivity at teleseismic stations would not significantly affect the energy estimates. Some studies suggest that the rupture propagated at super-shear velocities [Tibi et al., 2001], but this cannot be currently resolved.

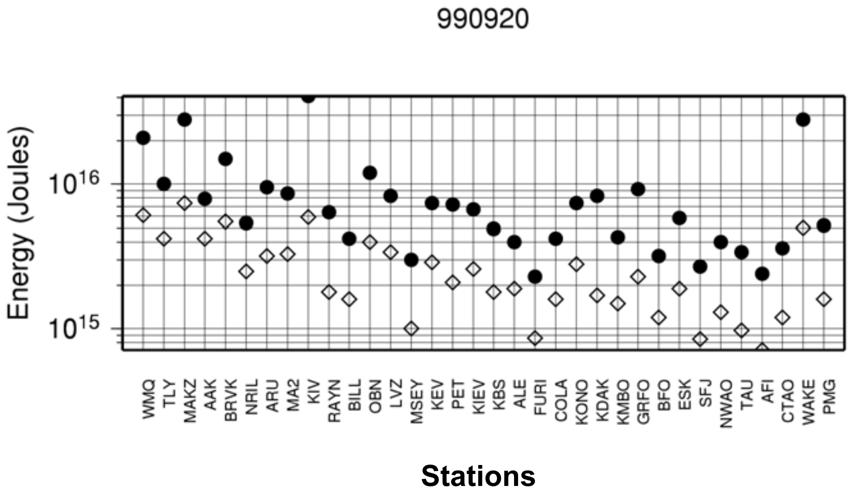

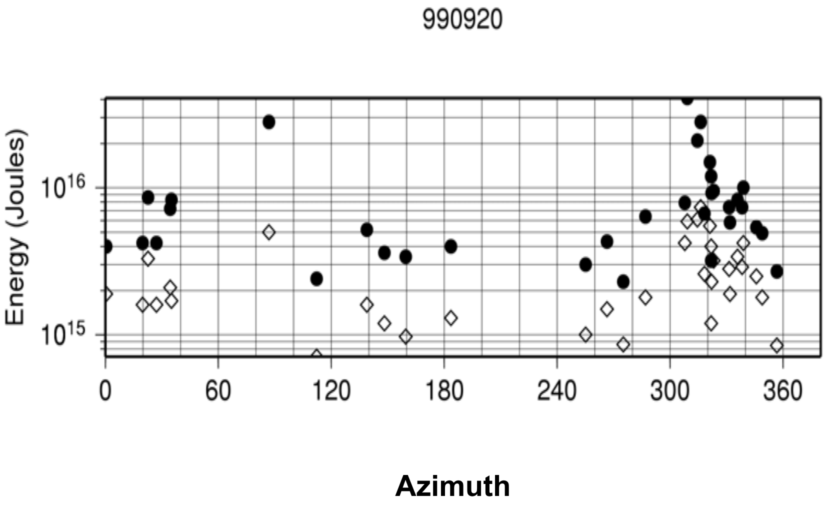

990920, Chi-Chi (Type 3): depth=7 km, mean E_R = 0.88 x 10^{16} J, directivity corrected E_R =0.66 x 10^{15} J, V =2 km/s (0.55 β) [Ji et al., 2002]. The Chi-Chi earthquake, M_0 =3.1 x 10^{20} Nm, was a thrust earthquake that ruptured the Chelungpu fault in western Taiwan [Ma et al., 2000]. The earthquake ruptured from south to north along strike and also downdip. A correction for directivity based on the slip model of Ji et al. [2002] changes the average single-station estimate by about 25% (discussed in Chapter 2).

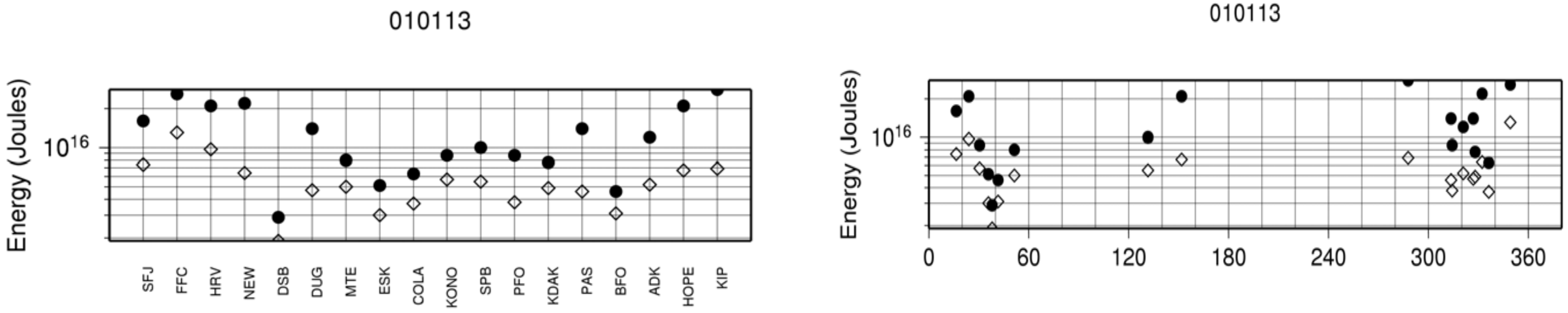

Stations **Azimuth**

010113, El Salvador (Type 5): depth=51 km, mean E_R = 0.13 x 10^{17} J, V =3.5 km/s (0.78 β) [Masayuki Kikuchi, written communication, 2002]. The El Salvador earthquake, M_0=4.4 x 10^{20} Nm, was an intraplate earthquake that ruptured the Cocos slab off the coast of El Salvador. The source is quite compact and shows no significant directivity.

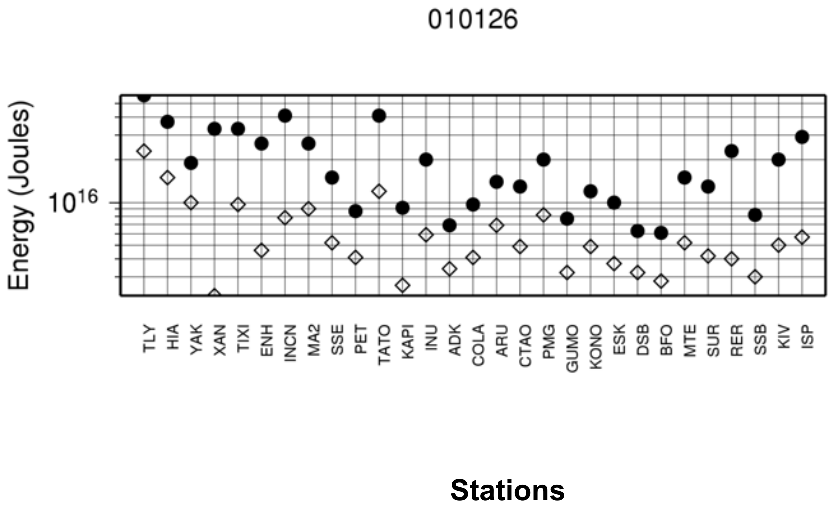

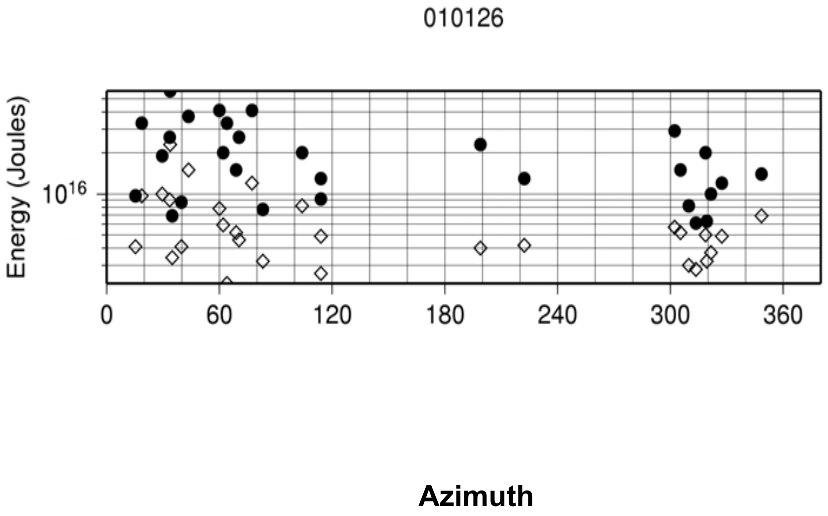

010126, India (Type 3): depth=24 km, mean E_R = 0.20 x 10^{17} J, V=2.5 km/s (0.64β) [Masayuki Kikuchi, written communication, 2002]. The India earthquake, M_0=3.1 x 10^{20} Nm, occurred in Bhuj in northwestern India. The earthquake occurred on a thrust fault with the rupture propagating along strike to the west [Masayuki Kikuchi, written communication, 2002], and thus the directivity effect on teleseismic estimates of energy is not significant (refer to section 2.1.1 in Chapter 2). Moreover, the source dimensions are small (40 x 40 km^2) indicating a compact source with little directivity.

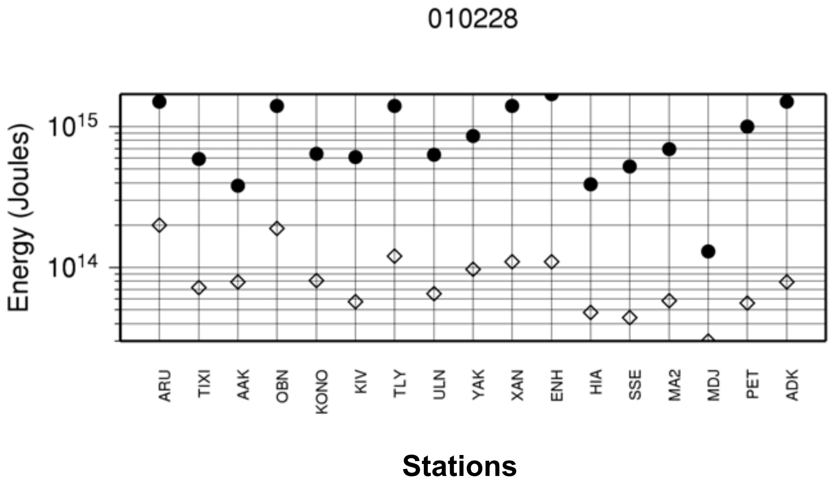

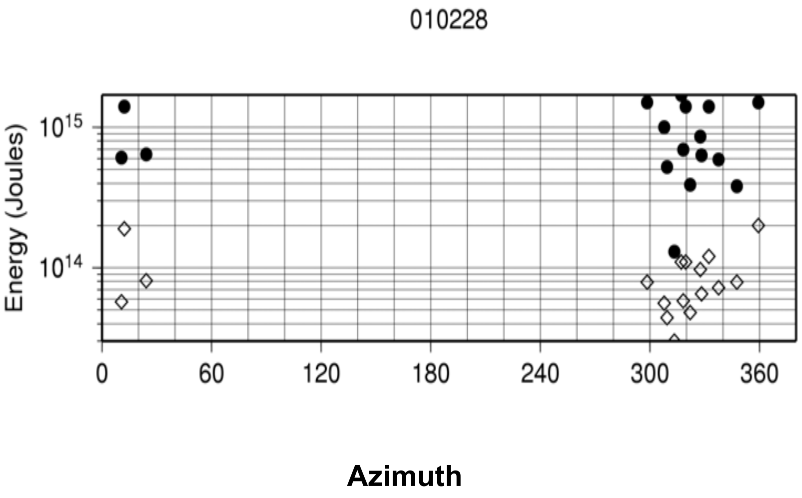

010228, Nisqually (Type 5): depth=52 km, mean E_R = 0.96 x 10^{15} J, V =2.5 km/s (0.64 β) [Masayuki Kikuchi, written communication, 2002]. The Nisqually earthquake, M_0 =1.9 x 10^{19} Nm, was an intraplate earthquake that occurred within the subducting Juan de Fuca slab beneath Seattle, Washington. The earthquake rupture is quite compact [Masayuki Kikuchi, written communication, 2002], and hence we do not see any significant directivity effects in the single-station energy estimates.

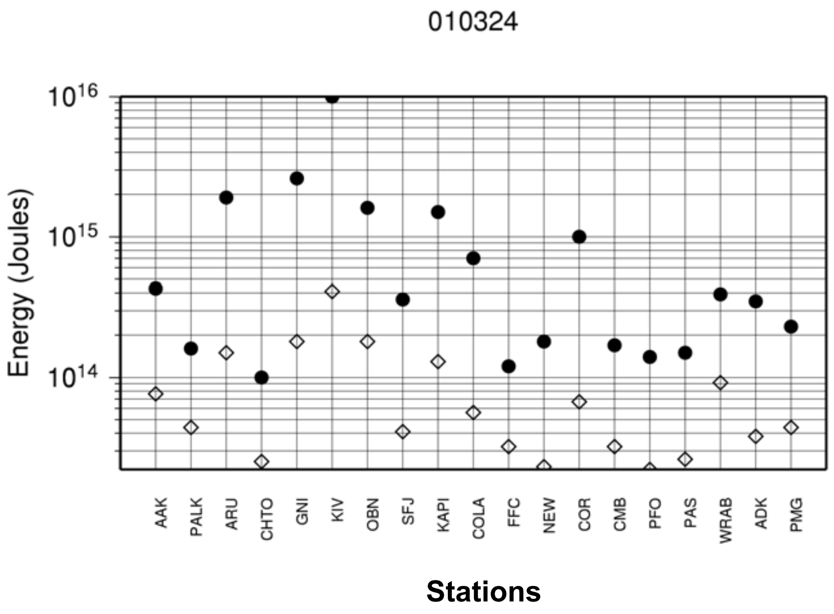

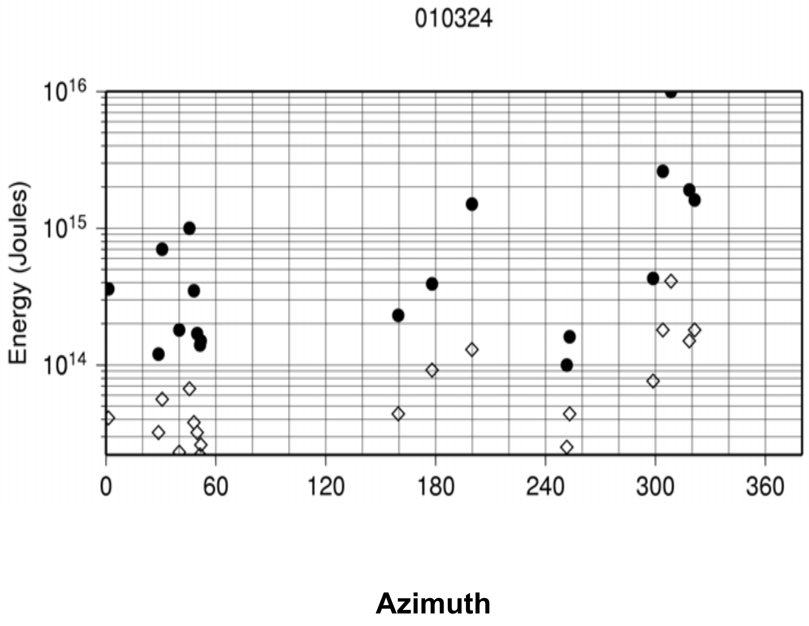

010324, Geiyo (Type 5): depth=50 km, mean E_R = 0.12 x 10^{16} J, V=2.9 km/s (0.65β) [Masayuki Kikuchi, written communication, 2002]. The Geiyo earthquake, M_0=1.9 x 10^{19} Nm, was an intraplate earthquake that occurred close to Hiroshima in southwestern Honshu, Japan. Masayuki Kikuchi [written communication, 2002] suggests that the earthquake propagated mostly to the south, but the directivity effects cannot be seen in the teleseismic single-station energy estimates shown above. Since the earthquake is small, the signal-to-noise ratio is poor at teleseismic stations causing a scatter of a factor of 100 in the single-station estimates. However, if we remove station KIV, the scatter is reduced, but the average of the single-station energy estimates changes by less than 5%. Thus, the average radiated energy estimate is quite robust.

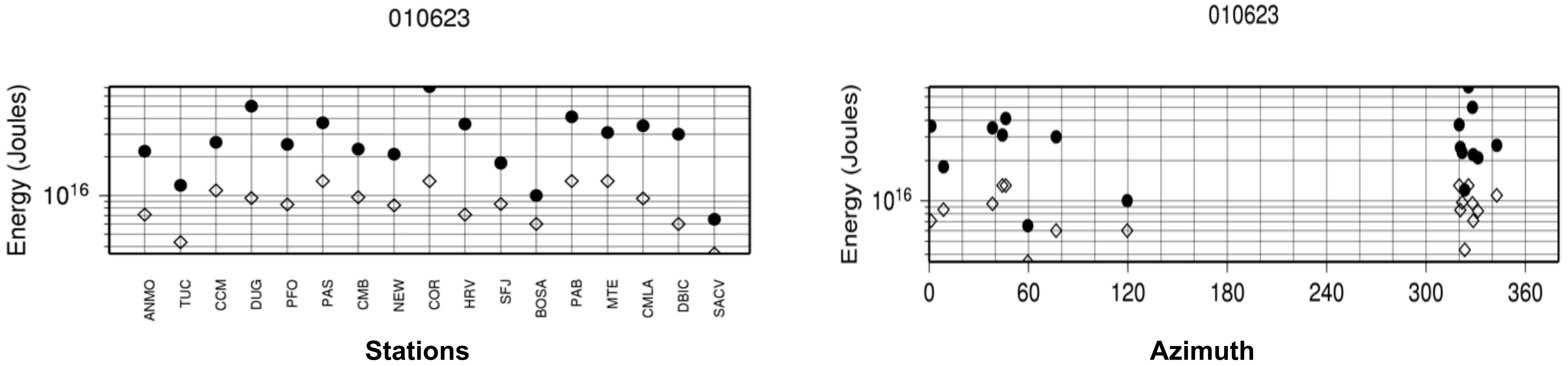

010623, Peru_3 (Type 1): depth=17 km, mean E_R = 0.29 x 10^{17} J, V ~ 2.2 km/s (0.5 β) [Masayuki Kikuchi, written communication, 2002]. The Peru earthquake, M_0 =3.5 x 10^{21} Nm, was an interplate earthquake that occurred close to the Peru_2 earthquake mentioned earlier. A large asperity is located to the southeast of the hypocenter [Masayuki Kikuchi, written communication, 2002], however, we do not see any significant directivity in the single-station energy estimates.

Figure 4.3 Teleseismic energy estimates for 27 events obtained using the single-station method. The event origin time is given above each subplot in yy-mm-dd format. The first subplot for each earthquake shows the energy estimates at each of the teleseismic where the stations are plotted in order of increasing rms radiation pattern factor; the second subplot for each earthquake is a plot of the energy estimates as function of station azimuth to show the azimuthal distribution of stations used to calculate energy. The open diamonds are the energy estimates obtained by integration of the squared velocity records in the time domain (no attenuation correction), while the closed circles are the energy estimates obtained by integration in the frequency domain with an attenuation correction that is modified from Der, [1998] (details in Appendix).

The open diamonds in Figure 4.3 represent the radiated energy estimates obtained by time domain integration of the squared velocity records. The time domain estimates include corrections for radiation pattern and geometric spreading effects, but do not include the attenuation correction, while the estimates of energy in the frequency domain (closed circle) include corrections for attenuation. The time domain estimates are useful to determine the appropriate time window of the record to be used such that most of the *P* wave group energy arrives within this window, and the effect of scattered energy on the energy estimates is minimized. Thus, the time domain estimates represent the lower limit of the radiated energy for each earthquake and the difference between the time domain and frequency domain estimates reflects the effect of the attenuation correction on the radiated energy estimates. The frequency domain estimates include all the energy in frequencies up to 1Hz; in most of the earthquakes studied here, there is less than 25% energy at frequencies beyond 1Hz and hence this was not included in the final energy estimates.

The average (mean) of the single-station energy estimates of energy in the frequency domain is shown in Figure 4.4. In Table 4.1, the mean and median of the single-station estimates of energy in the frequency domain are listed. The mean estimate is probably closer to the actual total energy because if there are several stations at azimuths close to the direction of rupture and very few stations at other azimuths, the median will be much larger that the actual total energy, whereas the mean would be closer to the actual total energy. Similarly, when the station distribution is such that there are a large number of stations away from the rupture direction, the median will be much smaller that the actual total energy whereas the mean would be closer to the actual total energy. In most of the earthquakes listed in Table 4.1, the mean is within a factor of two of the median.

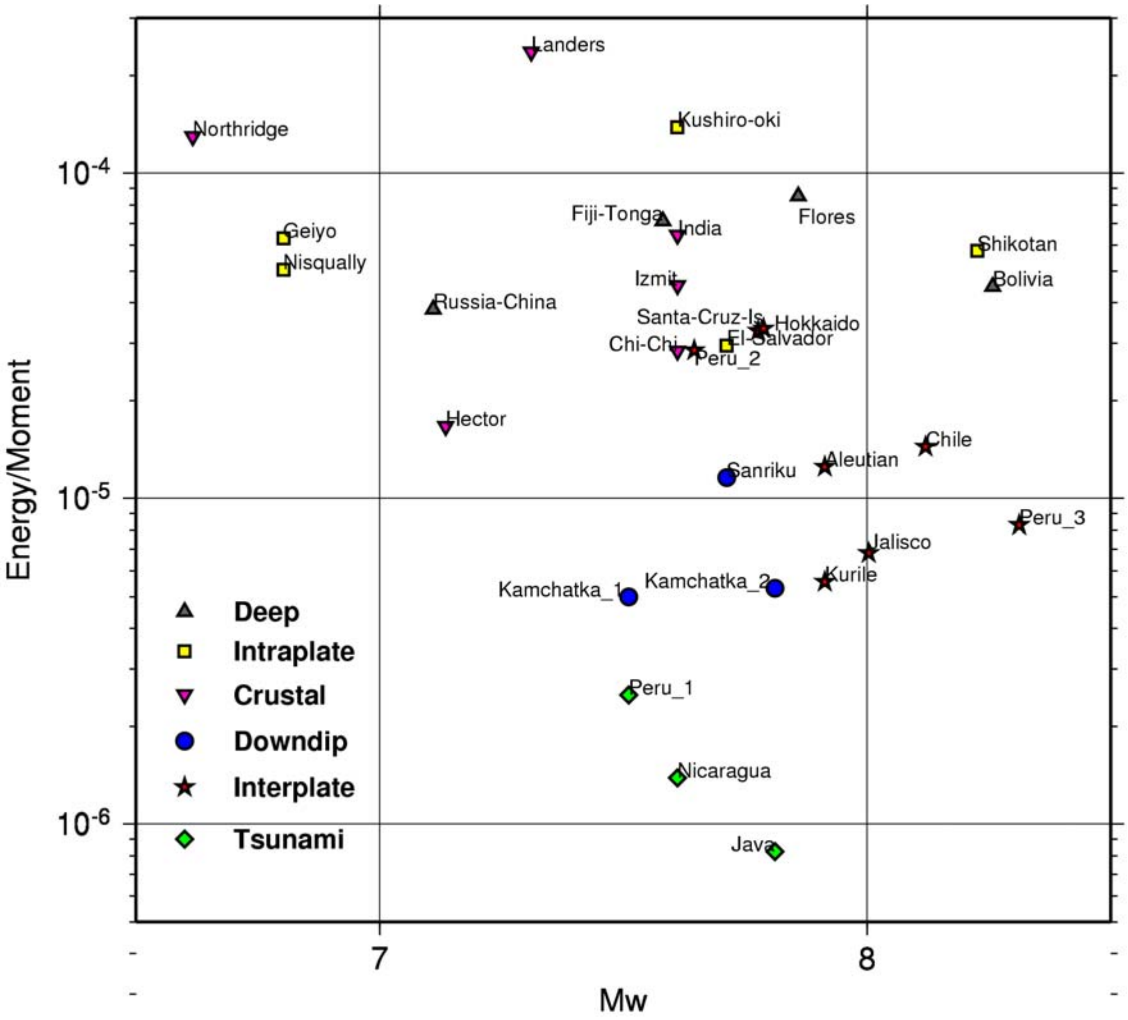

Figure 4.4 The computed energy-to-moment ratios plotted as a function of moment magnitude. The different symbols show different types of earthquakes as described in the legend. It is observed that tsunami earthquakes have the smallest energy-to-moment ratios, and crustal and deep earthquakes have the largest energy-to-moment ratios.

From Figure 4.4 we observe that the radiated energy-to-moment ratio is different for different types of earthquakes; tsunami earthquakes have the smallest radiated energy-to-moment ratio (7×10^{-7} to 3×10^{-6}), interplate and downdip earthquakes have a slightly larger ratio (5×10^{-6} to 2×10^{-5}) and intraplate and deep earthquakes have ratios similar to crustal earthquakes (2×10^{-5} to 3×10^{-4}).

Table 4.1 Radiated energy estimates of the earthquakes studied here

Origin Time	Event Name	Latitude	Longitude	Depth (km)	Dip	Rake	Strike	Radiated Energy (Joules)		Seismic Moment (Nm)	Type
								Mean	Median		
920628115734	Landers*	34.2N	116.4W	7	74	-176	340	0.26×10^{17}	0.15×10^{17}	1.1×10^{20}	3
920902001557	Nicaragua	11.2N	87.8W	20	15	91	303	0.43×10^{15}	0.47×10^{15}	3.1×10^{20}	2
930115110605	Kushiro-oki	43.1N	144.3E	107	11	-30	136	0.43×10^{17}	0.26×10^{17}	3.1×10^{20}	5
930608130338	Kamchatka_1	51.4N	158.8E	46	29	79	207	0.11×10^{16}	0.74×10^{15}	2.2×10^{20}	4
930712131736	Hokkaido	42.8N	139.2E	15	25	104	208	0.18×10^{17}	0.16×10^{17}	5.5×10^{20}	1
940117123055	Northridge+	34.4N	118.6W	19	42	116	130	0.13×10^{16}	NA	1.0×10^{19}	3
940309232807	Fiji-Tonga	17.7S	178.1W	569	27	-30	250	0.20×10^{17}	0.17×10^{17}	2.8×10^{20}	6
940602181737	Java	11.0S	113.0E	15	83	90	99	0.51×10^{15}	0.39×10^{15}	6.2×10^{20}	2
940609003345	Bolivia	13.8S	67.5W	647	89	-103	95	0.13×10^{18}	0.88×10^{17}	2.9×10^{21}	6
941004132328	Shikotan	43.5N	147.4E	56	75	125	49	0.15×10^{18}	0.95×10^{17}	2.6×10^{21}	5
941228121924	Sanriku	40.5N	143.0E	27	12	67	179	0.51×10^{16}	0.44×10^{16}	4.4×10^{20}	4
950730051123	Chile	24.2S	70.7W	32	19	110	8	0.26×10^{17}	0.22×10^{17}	1.8×10^{21}	1
951009153556	Jalisco	19.3N	104.8W	15	9	92	302	0.82×10^{16}	0.41×10^{16}	1.2×10^{21}	1
951203180108	Kurile	44.8N	150.2E	26	12	95	225	0.49×10^{16}	0.45×10^{16}	8.8×10^{20}	1
960221125104	Peru_1	9.9S	80.2W	15	21	66	330	0.55×10^{15}	0.57×10^{15}	2.2×10^{20}	2
960610040335	Aleutian	51.1N	177.4W	29	17	84	248	0.11×10^{17}	0.60×10^{16}	8.8×10^{20}	1
960617112216	Flores	7.4S	123.0E	588	55	-51	100	0.62×10^{17}	0.33×10^{17}	7.3×10^{20}	6

961112165944	Peru_2	15.0S	75.4W	25	64	110	172	0.10×10^{17}	0.90×10^{16}	3.5×10^{20}	1
970421120225	Santa-Cruz-Is	13.2S	166.2E	30	27	35	302	0.19×10^{17}	0.16×10^{17}	5.7×10^{20}	1
971205112704	Kamchatka_2	54.3N	161.9E	34	23	74	202	0.33×10^{16}	0.24×10^{16}	6.2×10^{20}	4
990408131034	Russia-China	43.6N	130.3E	564	28	160	81	0.21×10^{16}	0.14×10^{16}	5.5×10^{19}	6
990817000139	Izmit	41.0N	29.9E	15	83	181	270	0.14×10^{17}	0.11×10^{17}	3.1×10^{20}	3
990920174735	Chi-Chi	23.8N	120.8E	7	30	85	20	0.88×10^{16}	0.64×10^{16}	3.1×10^{20}	3
991016094645	Hector*	34.5N	116.3W	7	78	165	330	0.10×10^{16}	0.78×10^{15}	6.0×10^{19}	3
010113173331	El-Salvador	12.9N	89.1W	51	34	-98	119	0.13×10^{17}	0.10×10^{17}	4.4×10^{20}	5
010126031641	India	23.5N	70.3E	24	50	50	65	0.20×10^{17}	0.17×10^{17}	3.1×10^{20}	3
010228185436	Nisqually	47.0N	122.5W	52	71	-99	346	0.96×10^{15}	0.78×10^{15}	1.9×10^{19}	5
010324062752	Geiyo	34.1N	132.6E	50	38	-121	323	0.12×10^{16}	0.36×10^{15}	1.9×10^{19}	5
010623203313	Peru_3	16.1S	73.3W	17	16	40	301	0.29×10^{17}	0.29×10^{17}	3.5×10^{21}	1

[+] The estimates for these earthquakes are regional estimates from Hiroo Kanamori [written communication, 2002].

[*] These estimates have been corrected for directivity.

Latitude, longitude, dip, rake and strike are in degrees. Type 1: Interplate earthquakes; Type 2: Tsunami earthquakes;

Type 3: Crustal earthquakes; Type 4: Downdip earthquakes; Type 5: Intraplate earthquakes; Type 6: Deep earthquakes.

4.4 Partitioning of Energy in Earthquakes

4.4.1 Radiation Efficiency

From Figure 4.4 we observe that the ratio of radiated energy-to-moment is different for different types of earthquakes. However, to relate these ratios to the physical processes in the fault zone, we have to use a model and understand the partitioning of energy in earthquakes. As discussed in the last chapter, and briefly summarized below, we can use a stress relaxation model to determine the radiation efficiency, where radiation efficiency is defined as the ratio of radiated energy to the sum of the radiated and fracture energy. Using our estimates of radiated energy, estimates of static stress drop (to be discussed) and the stress relaxation model, we can determine the amount of fracture energy expended in the rupture process. Fracture energy can then be related to the physical processes on the fault zone.

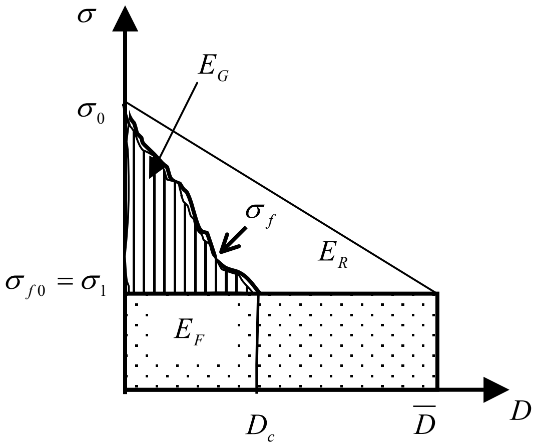

Figure 4.5 (same as Figure 3.4) Schematic representation of the partitioning of energy in earthquakes. The dark line shows the variation of frictional stress on the fault as a function of slip. The striped region represents the fracture energy, while the stippled region represents the frictional energy for the model.

Thus, from figure 4.5, we can write

$$\eta_R = \frac{E_R}{E_R + E_G} = \frac{E_R}{(\sigma_0 - \sigma_1)\overline{D}S/2},$$

where E_R is the radiated energy, and E_G is the fracture energy. Thus from the static stress drop, $\Delta\sigma_s = \sigma_0 - \sigma_1$, the radiated energy, E_R, and seismic moment, M_0, we can determine radiation efficiency $\eta_R = \frac{E_R}{E_R + E_G} = \frac{2\mu\tilde{e}}{\Delta\sigma_s}$, where $\tilde{e} = \frac{E_R}{M_0}$. This fracture energy is the minimum energy that is dissipated on the fault zone and can hence be directly related to physical processes on the fault zone. However, to determine radiation efficiency we require estimates of static stress drop. In the following section, we discuss the difficulties in the estimation of static stress drops and list the best estimates of static stress drops that we compiled from literature.

4.4.2 Static Stress Drop

Static stress drop is defined as the change in the average state of stress on a fault before and after rupture. As stress is proportional to strain, in simple terms, static stress drop can be written as [*Kanamori and Anderson*, 1975]:

$$\Delta\sigma_S = C\mu\frac{\overline{D}}{\tilde{L}}$$

where $\overline{D}$ is the average slip on the fault, $\tilde{L}$ is a characteristic rupture dimension, C is a non-dimensional constant that depends on the shape of the rupture surface and on the type of faulting (orientation of the shear stress) and μ is the shear modulus. The strain is $\overline{D}/\tilde{L}$.

Table 4.2 gives the theoretical static stress drops for different fault geometries; λ is Lame's constant, and usually $\lambda \sim \mu$. For a circular rupture, $\tilde{L} \sim a$, the radius of rupture; for rupture propagating on a rectangular fault, L is the length of the rupture and w is the width of the rupture.

Table 4.2: Static stress drop for different fault geometries

Type of Faulting	**Stress Drop** $\Delta\sigma_s$	**Reference**
Circular fault	$\frac{7\pi}{16}\mu\frac{\overline{D}}{a}$	*Eshelby*, 1957, *Keilis-Borok*, 1959
Strike-slip fault with surface break, half-space, $L >> w$	$\frac{2}{\pi}\mu\frac{\overline{D}}{w}$	*Knopoff*, 1958
Strike-slip fault, whole space, $L >> w$	$\frac{4}{\pi}\mu\frac{\overline{D}}{w}$	*Knopoff*, 1958
Dip-slip fault with surface break, half-space, $L >> w$	$\frac{4}{\pi}\frac{(\lambda+\mu)}{(\lambda+2\mu)}\mu\frac{\overline{D}}{w}$	*Starr*, 1928, *Aki*, 1966
Dip-slip fault, whole space ($\lambda \sim \mu$), $L >> w$	$\frac{16}{3\pi}\mu\frac{\overline{D}}{w}$	*Starr*, 1928

In the above cases, the non-dimensional constant, C, is determined for faults embedded in a whole-space or half-space with $L >> w$. *Boore and Dunbar* [1977] computed the constant C for different depths of burial and for a range of aspect ratios, L/w. Subsequently, *Parsons et al.* [1988] found some inconsistencies in the published results and their revised results are given in the Table below:

Table showing values of C from *Parsons et al.*, 1988

L/w	**Fault Type**	$\frac{d}{w}=0$	$\frac{d}{w}=0.02$	$\frac{d}{w}=0.165$	$\frac{d}{w}\to\infty$
1	Strike-slip	2.04	2.35	2.48	2.55
2	Strike-slip	1.26	1.60	1.75	1.83
∞	Strike-slip	0.65	0.99	1.16	1.28
∞	Dip-slip	0.67	1.10	1.41	1.70

In the above Table, the depth of burial of the fault is given as d . Thus, the limits $d/w = 0$ and $d/w \to \infty$ correspond to surface breaking and infinitely buried faults. From the above results and from Table 4.1, we observe that for most practical cases, C varies between 1.0 and 2.5, thus, if we know the slip and characteristic rupture length, we can estimate the static stress drop to within a factor of 3.

The actual stress drop on a fault can be very heterogeneous because of variations in stress and strength distribution on the fault plane. Thus, the actual slip distribution on the fault plane could vary spatially resulting in very high stress drops locally, as compared to the average value over the fault [*Madariaga*, 1979]. However, we are interested in the average stress drop on the fault, a macroscopic parameter, and studies suggest that estimates of average stress drops will not be significantly affected by heterogeneous slip distribution except when slip is concentrated at the edges of the fault [*Madariaga*, 1977; *Madariaga*, 1979]. *Rudnicki and Kanamori* [1981] show that even in the case of heterogeneous slip distribution on the fault plane, unless the ratio of asperity length to fault size is very small (i.e., too many small patches of slip on a large fault), the estimates of stress drop are good to within a factor of 2. More recent numerical experiments also suggest that for rectangular faults if we know the average slip and approximate fault geometry with some large asperities, we can estimate the average stress drop to within 20% even if the actual distribution of asperities is not well determined [*Das*, 1988].

Several methods are used to estimate stress drop (a discussion of the different methods can be found in *Kanamori*, [1994]). In this study, we used estimates of stress drop that were mostly determined from seismic moment and rupture area. Although moment can be accurately determined, the rupture area which is usually determined from the aftershock area or from inversion of seismic, GPS or tsunami data is in most cases a poorly resolved quantity. The aftershock area is not always representative of the co-seismic rupture area, but in cases where there is no other data, this method is often used to determine rupture area. Seismic, GPS and tsunami data are usually inverted separately or together when more than one dataset is available to determine the slip distribution on the fault plane; however the slip distributions currently obtained from inversion of GPS data alone or tsunami data alone are usually not well constrained.

Inversions of slip models generally use rectangular fault planes with dimensions exceeding the actual dimensions of the rupture area. In most slip models, heterogeneous slip distribution on the fault can result in regions on the fault that have almost zero slip and also the slip falls off towards the edges of the fault plane. Accordingly, these areas of low or zero slip have to be accounted for in determining an “effective” rupture area, i.e., the area where most of the slip is concentrated. Different investigators use different methods to tackle this issue, for example, *Somerville et al.* [1999], use a “trimming criteria”. For using this criteria, the fault plane is considered to be a gridded rectangle with rows and columns with the slip is distributed on this grid; they remove successive rows (or columns) at the fault edge if the average slip per fault element in the entire row or column is less than 3% of the average slip on the whole fault; the seismic moment of the earthquake is slightly smaller after this trimming. *Mai and Beroza* [2000], on the other hand, use an autocorrelation width to determine the effective fault dimensions and also normalize the effective mean slip so that the seismic moment of the fault remains unchanged.

For crustal earthquakes in California (Landers, Northridge, and Hector Mine), we use the rupture dimensions determined by *Nazareth* [2002], where they use the trimming criteria of *Somerville et al.* [1999]. For example, to compute the static stress drop for the Hector Mine earthquake, if we use the formula for static stress drop, $\Delta\sigma_S = \frac{2}{\pi}\frac{M_0}{\sum_N W^2 L}$, where M_0 is the total seismic moment and the summation is over N fault segments, we obtain a static stress drop of 1.8 MPa for the rupture dimensions of the model of *Ji et al.* [2002b], but if we use the trimmed rupture dimensions from *Nazareth* [2002], we obtain a static stress drop of 3.2 MPa. For the trimmed model, if we calculate the static stress drops of the individual segments and then calculate the average stress drop, i.e., if we calculate the static stress drop using, $\Delta\sigma_S = \frac{1}{N}(\frac{2}{\pi}\sum_N \frac{M_0}{W^2 L})$, where M_0 is the moment of each subfault, we still obtain a mean static stress drop of 3.3 MPa. Thus, in this case, the average stress drop on the fault increases by less than 4% when we sum the stress drops of individual fault segments to determine the average stress drop. However, locally, the stress drop on the fault could be very high.

A large number of static stress drop estimates listed in Table 4.3 were obtained from *Masayuki Kikuchi,* [written communication*,* 2002], in which the effective fault area is determined from slip models obtained by inversion of teleseismic data. The length over which most of the moment is concentrated is assumed to be the rupture length and the rupture width is assumed to be equal to half the rupture length. If M_0 is the seismic moment, and S is the rupture area, the stress, $\Delta\sigma_S$, can also be written as

$$\Delta\sigma_S = C\mu\frac{\overline{D}}{\widetilde{L}} = C\frac{M_0}{S^{3/2}}$$

In most of these estimates listed in Table 4.3, a circular fault was assumed and in cases where the rupture broke the surface, a correction for the free-surface effect was included. As mentioned earlier, the stress drop estimates determined by different investigators could be different by a factor of two because of the different values of the constant, C used in the above formula. Moreover, determining the dimensions of the fault plane from inversion of teleseismic data is not very straightforward. It is difficult to determine the rupture area of shallow tsunami earthquakes because of the difficulty in modeling the lateral heterogeneities and complex structure close to the trench. This problem can be solved if there are strong motion stations located close to the trench, but this would usually require ocean bottom seismometers; in most instances, even the land based instruments are not located close to the trench.

For the 1994 Bolivia earthquake, which is the largest deep earthquake that has been well recorded, most investigators find that the rupture occurred over a small area with dimensions of about 40 km x 40 km and hence the stress drops calculated using this dimension are very high (~110 MPa) [*Kikuchi and Kanamori*, 1994; *Goes and Ritsema*, 1995]. Because of the large size of the Bolivia earthquake, coupled with the fortuitous recording of the earthquake by an array of seismometers deployed almost on top of the epicenter, the rupture dimensions for this earthquake are probably better resolved than for other deep earthquakes. Also, it is suspected that locally the stress drop in this earthquake could have been much higher. More generally, in case of deep earthquakes, unless the earthquake is large (like the Bolivia earthquake), the teleseismic signal-to-noise ratio is poor and also the source is almost like a point source for teleseismic waves. Thus, it is difficult to determine the rupture length or rupture dimensions for small deep earthquakes unless a regional network is located close to the epicenter of the earthquake. We surveyed the available literature and for most earthquakes, we could obtain more than one estimate of the static stress drop. In some cases, we used some subjective judgement to decide on the representative rupture area. Table 4.3 is a compilation of the available stress drop estimates of the earthquakes studied here. Figure 4.6 shows the static stress drop estimates listed in Table 4.3 as a function of depth.

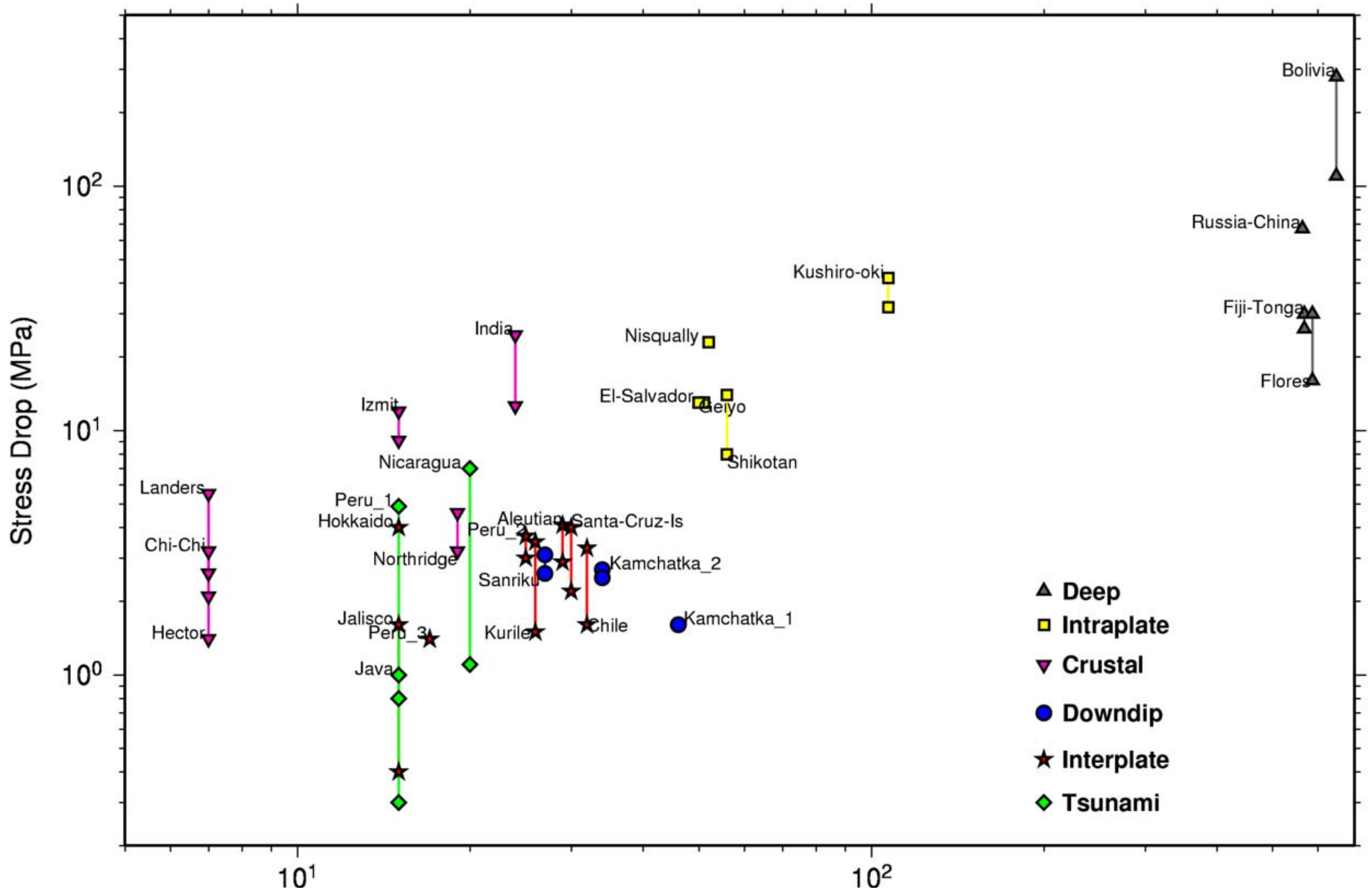

Figure 4.6 Static stress drop plotted as a function of depth for the different types of earthquakes studied.

Table 4.3: Static stress drop estimates of the earthquakes studied here.

Origin Time	Stress Drop (MPa)		Reference for upper limit	Reference for lower limit
	Upper Limit	Lower Limit		
920628115734 Landers (depth=7 km)	5.5	2.6	Calculated from *Thio and Kanamori*, 1996, using $\Delta\sigma_S = \frac{2}{\pi}\mu\frac{\overline{D}}{w}$ $\overline{D} = 3.5\,\text{m}, w = 12\,\text{km}$	Calculated from *Nazareth*, 2002, using $\Delta\sigma_S = \frac{2}{\pi}\mu\frac{\overline{D}}{w}$ $M_0 = 7.68\times10^{19}$ Nm, $w = 15\,\text{km}, L = 84\,\text{km}$
920902001557 Nicaragua (depth=20 km)	7.0	1.1	*Ihmle*, 1996	*Kanamori and Kikuchi*, 1993
930115110605 Kushiro-oki (depth=107 km)	42.0	32.0	*Takeo et al.*, 1993	*Yoshiaka and Tokunaga*, 1998
930608130338 Kamchatka_1 (depth=46 km)	1.6	NA	*Johnson et al.*, 1995	
930712131736 Hokkaido (depth=15 km)	4.0	NA	*Tanioka et al.*, 1995	
940117123055 Northridge (depth=19 km)	4.6	3.2	Calculated from *Nazareth*, 2002, (N-DR model) using $\Delta\sigma_S = \frac{7\pi^{3/2}}{16}\frac{M_0}{S^{3/2}}$ $M_0 = 1.05\times10^{19}$ Nm, $S = 14\times22\,\text{km}^2$	Calculated from *Nazareth*, 2002, (N-HV model) using $\Delta\sigma_S = \frac{7\pi^{3/2}}{16}\frac{M_0}{S^{3/2}}$ $M_0 = 1.63\times10^{19}$ Nm, $S = 20\times26\,\text{km}^2$

940309232807 Fiji-Tonga (depth=569 km)	30.0	26.0	*Tibi et al.*, 1999	*Goes and Ritsema*, 1995
940602181737 Java (depth=15 km)	1.0	0.3	Calculated from *Tanioka and Satake*, 1996, using $\Delta\sigma_S = \frac{1}{2}\frac{7\pi^{3/2}}{16}\frac{M_0}{S^{3/2}}$ $M_0 = 3.5 \times 10^{20}$ Nm, $S = 90 \times 60\,\mathrm{km}^2$	*Abercrombie et al.*, 2001
940609003345 Bolivia (depth=647 km)	280.0	110.0	*Goes and Ritsema*, 1995	*Kikuchi and Kanamori*, 1994
941004132328 Shikotan (depth=56 km)	14.0	11.0	*Ozawa*, 1996	*Kikuchi and Kanamori*, 1995a
941228121924 Sanriku (depth=27 km)	3.1	2.6	*Sato et al.*, 1996	Kikuchi's web-site
950730051123 Chile (depth=32 km)	3.3	1.6	Calculated from Kikuchi's web-site using $\Delta\sigma_S = \frac{1}{2}\frac{7\pi^{3/2}}{16}\frac{M_0}{S^{3/2}}$ $M_0 = 1.7 \times 10^{21}$ Nm, $S = 120 \times 60\,\mathrm{km}^2$	Calculated from *Carlo et al.*, 1999, using $\Delta\sigma_S = \frac{1}{2}\frac{7\pi^{3/2}}{16}\frac{M_0}{S^{3/2}}$ $M_0 = 1.6 \times 10^{21}$ Nm, $S = 190 \times 60\,\mathrm{km}^2$

951009153556 Jalisco (depth=15 km)	1.6	0.4	Calculated from *Pacheco et al.*, 1997, using $\Delta\sigma_S = \frac{1}{2}\frac{7\pi^{3/2}}{16}\frac{M_0}{S^{3/2}}$ $M_0 = 1.8 \times 10^{21}$ Nm, $S = 170 \times 70\,\mathrm{km}^2$	Calculated from *Mendoza and Hartzell*, 1999, using $\Delta\sigma_S = \frac{1}{2}\frac{7\pi^{3/2}}{16}\frac{M_0}{S^{3/2}}$ $M_0 = 8.3 \times 10^{20}$ Nm, $S = 200 \times 100\,\mathrm{km}^2$
951203180108 Kurile (depth=26 km)	3.5	1.5	Kikuchi's web-site	Calculated from *Hurukawa*, 1998, using $\Delta\sigma_S = \frac{7\pi^{3/2}}{16}\frac{M_0}{S^{3/2}}$ $M_0 = 8.8 \times 10^{20}$ Nm, $S = 140 \times 90\,\mathrm{km}^2$
960221125104 Peru_1 (depth=15 km)	4.9	0.8	Kikuchi's web-site	Calculated from *Ihmle et al.*, 1998, using $\Delta\sigma_S = \frac{1}{2}\frac{7\pi^{3/2}}{16}\frac{M_0}{S^{3/2}}$ $M_0 = 2.0 \times 10^{20}$ Nm, $S = 110 \times 40\,\mathrm{km}^2$
960610040335 Aleutian (depth=29 km)	4.1	2.9	Calculated from *Tanioka and Gonzalez*, 1998, using $\Delta\sigma_S = \frac{1}{2}\frac{7\pi^{3/2}}{16}\frac{M_0}{S^{3/2}}$ $M_0 = 7.3 \times 10^{20}$ Nm, $S = 120 \times 30\,\mathrm{km}^2$	Kikuchi's web-site
960617112216 Flores (depth=588 km)	30.0	16.0	*Tibi et al.*, 1999	*Goes et al.*, 1997

961112165944 Peru_2 (depth=25 km)	3.7	3.0	Calculated from *Swenson and Bilek*, 1999, using $\Delta\sigma_S = \frac{7\pi^{3/2}}{16}\frac{M_0}{S^{3/2}}$ $M_0 = 3.4 \times 10^{20}$ Nm, $S = 90 \times 45\,\text{km}^2$	Kikuchi's web-site
970421120225 Santa-Cruz-Is (depth=30 km)	4.0	2.2	*Kaverina et al.*, 1998	Kikuchi's web-site
971205112704 Kamchatka_2 (depth=34 km)	2.7	2.5	Kikuchi's web-site	Calculated from *Wha*, 1998, using $\Delta\sigma_S = \frac{7\pi^{3/2}}{16}\frac{M_0}{S^{3/2}}$ $M_0 = 2.5 \times 10^{20}$ Nm, $S = 88 \times 44\,\text{km}^2$
990408131034 Russia-China (depth=564 km)	16.0	NA	Martin Griffith, personal communication	
990817000139 Izmit (depth=15 km)	12.0	9.1	*Tibi et al.*, 2001	Kikuchi's web-site
990920174735 Chi-Chi (depth=7 km)	3.2	2.1	Kikuchi's web-site	Calculated from *Ji et al.*, 2002, using $\Delta\sigma_S = \frac{1}{2}\frac{7\pi^{3/2}}{16}\frac{M_0}{S^{3/2}}$ $M_0 = 2.7 \times 10^{20}$ Nm, $S = 2924\,\text{km}^2$
991016094645 Hector (depth=7 km)	3.2	1.4	Calculated from *Nazareth*, 2002 (H-J model) method discussed in text	Calculated from *Nazareth*, 2002 (H-K model) method discussed in text

010113173331 El-Salvador (depth=51 km)	13.0	NA	Kikuchi’s web-site	
010126031641 India (depth=24 km)	24.6	12.6	*Negishi et al.*, 2001	*Negishi et al.*, 2001
010228185436 Nisqually (depth=52 km)	23.0	NA	Kikuchi’s web-site	
010324062752 Geiyo (depth=50 km)	13.0	NA	Kikuchi’s web-site	
010623203313 Peru_3 (depth=17 km)	1.4	NA	Kikuchi’s web-site	

Kikuchi’s web site: *Masayuki Kikuchi*, written communication, April 10, 2002.

Events from 1991 to June, 1996

http://wwweic.eri.u-tokyo.ac.jp/EIC/YCU_report/

Events from August, 1996 to March, 2002

http://wwweic.eri.u-tokyo.ac.jp/EIC/EIC_News/

4.5 Results and Discussion

Using the estimates of radiated energy, seismic moment and static stress drop, we calculated the radiation efficiency for all the earthquakes studied. Figure 4.7 is a plot of the strain drop (stress drop/rigidity) and energy-to-moment ratios of these earthquakes. Also shown are lines of constant radiation efficiency ($\eta_R = 2\frac{E_R / M_0}{\Delta\sigma_S / \mu}$) with radiation efficiency increasing diagonally down the page from left to right from 0.01 to 1. From the figure, we observe that the radiation efficiency of most earthquakes lies between 0.25 and 1. Tsunami earthquakes, however, have small radiation efficiencies (<0.25) and the two deep earthquakes: the 1999 Russia-China border event and the 1994 deep Bolivia earthquake have small radiation efficiencies. Thus, most earthquakes have non-dissipative rupture mechanisms but tsunami earthquakes and the two deep earthquakes mentioned above dissipate a large amount of energy on the fault zone.

From Figure 4.4, we observed that the ratio of radiated energy-to-moment is large for intraplate and deep earthquakes and for most crustal earthquakes, but from Figure 4.6 we observe that stress drop is also large for these earthquakes. This implies that the energy available for fracture and for the generation of seismic waves (as given by the top triangle in Figure 4.5) is larger in these earthquakes. Similarly, the interplate and downdip extensional events have smaller energy-to-moment ratios, but the associated stress drops are also small. Hence, despite the differences in the radiated energy-to-moment ratios, because of the corresponding differences in static stress drops, interplate, downdip, intraplate and deep earthquakes have the same radiation efficiencies. Thus, most earthquakes, except for tsunami earthquakes and the two deep earthquakes mentioned earlier, are efficient and have radiation efficiencies between 0.25

and 1. To understand this further, we will study deep earthquakes, tsunami earthquakes and the other earthquakes as three separate groups.

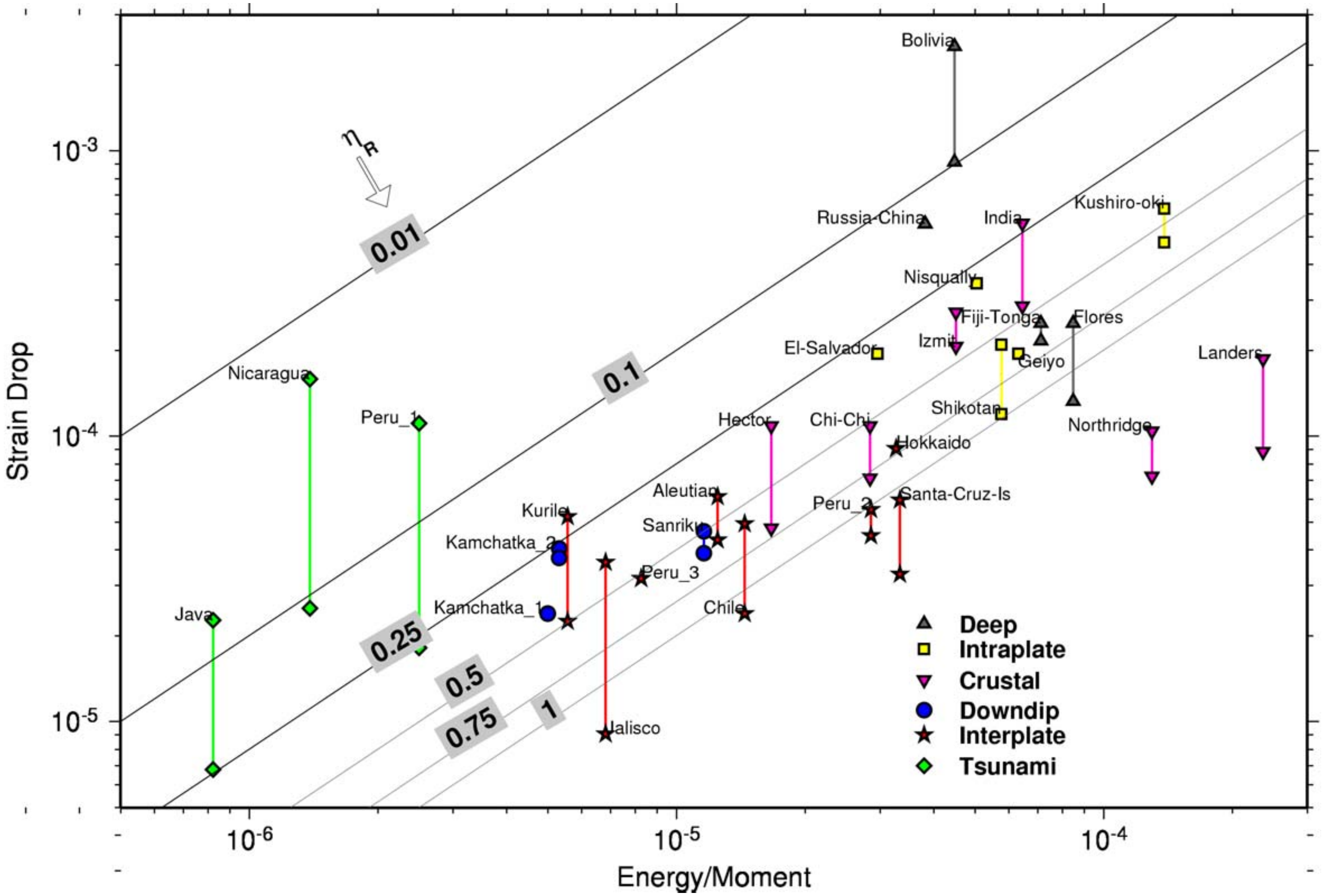

Figure 4.7 Strain (static stress drop/rigidity) is plotted against energy/moment. The lines shown are lines of constant radiation efficiency where radiation efficiency increases diagonally from left to right.

Deep Earthquakes

The 1994 deep earthquake in Bolivia is the largest deep focus earthquake that has been instrumentally recorded [*Kikuchi and Kanamori*, 1994]. Studies have shown that the rupture propagated very slowly (~1km/s) in this earthquake [*Kikuchi and Kanamori*, 1994; *Silver et al.*, 1995] and the earthquake had a very large static stress drop (110MPa – 280MPa) [*Kikuchi and Kanamori*, 1994; *Goes and Ritsema*, 1995]. *Kanamori et al.* [1998], proposed that the earthquake involved frictional melting on the fault plane. In this study, we observe that the radiation efficiency of this event is very small (between 0.1 and 0.04) indicating that a huge amount of energy of about 1×10^{18} J to 3×10^{18} J was dissipated on the fault plane.

Earlier studies have used this dissipated energy to calculate the minimum frictional stress on the fault plane during rupture. However, in these studies, the physical models used to understand the partitioning of energy in an earthquake assumed that this dissipated energy was completely used in frictional heating on the fault plane [*Kikuchi*, 1992; *Kanamori et al.*, 1998; *Wiens*, 2001]. These models do not explicitly account for the fracture energy, i.e., the mechanical energy (other than heat energy) that is dissipated during fracture processes. Fracture energy and frictional energy cannot be distinguished as such, but for a rupture to propagate, some amount of energy has to be spent in mechanical processes on the fault zone. In the earlier studies, it was assumed that this dissipated energy was completely used in frictional heating on the fault plane, but unless it is assumed that only a small part of this energy is consumed in other mechanical processes, this energy cannot be used to determine the minimum frictional stress on the fault. A part of this fracture energy (Figure 4.5) could eventually be dissipated as heat on the fault, but we cannot determine this from seismology.

The 1999 Russia-China earthquake also has small radiation efficiency (about 0.14); the average rupture velocity for the Russia-China event is small, about 2 km/s [*Martin Griffiths,* written communication*,* 2002]. The 1994 Bolivia earthquake and the 1999 Russia-China earthquake are unlike the other two deep earthquakes studied (the 1994 Fiji-Tonga earthquake and the 1996 Flores Sea earthquake) which have radiation efficiencies larger than 0.5, much smaller static stress drops and rupture velocities between 3-5 km/s (V/β between 0.7 and 0.9) [*Tibi et al.*, 1999].

Another seismological observation is based on the earthquake magnitude-frequency relationships in different subduction zones. The Fiji-Tonga slab has a large number of small deep earthquakes, i.e., a large b-value, while the South American slab has a very small b-value with very few small earthquakes and some very large earthquakes [*Giardini*, 1988; *Frolich*, 1989]. The slab that subducts beneath the Flores Sea region has a large number of small earthquakes, while the Japan slab that ruptured in the Russia-China earthquake does not have as much deep seismicity in this region [*Wiens and Gilbert*, 1996; *Wu and Chen*, 2001]. *Wiens and Gilbert* [1996] and *Wiens* [2001] use a thermal parameter which is defined as the product of the slab vertical descent rate and the age of the subducting lithosphere as a measure of the temperature of the slab at depth; a larger thermal parameter is indicative of a colder slab at depth. They observe a systematic relationship between b-values and the thermal parameter in slabs–slabs with smaller b-values have smaller thermal parameter and are hence warmer. Further, they also observe that the radiation efficiency (they call it seismic efficiency) increases with a decrease in thermal parameter. Thus, our results are consistent with their observations–the 1994 Bolivia earthquake has the smallest radiation efficiency and correspondingly the smallest thermal parameter, both parameters are slightly larger for the 1999 Russia-

China event that occurred in the Japan slab, and even larger for the 1996 Flores Sea and the 1994 Fiji-Tonga events.

We next try to address the issue of the mechanisms of deep earthquake faulting, a problem that has invoked significant interest through the years, and whether our results help us understand this problem better. Since we cannot envisage ordinary brittle failure at the pressures and temperatures at which deep earthquakes occur, several mechanisms have been proposed to explain deep earthquakes. Some of the suggested mechanisms include 1) dehydration embrittlement, where brittle fracture is induced by the release of volatiles which serve to increase the pore pressure and thus reduce the effective stress on the fault [*Meade and Jeanloz*, 1991]; 2) transformational faulting where phase changes cause faulting due to the rapid growth of an anticrack and the resulting thermal runaway processes cause the fault to grow catastrophically [*Green II and P.C.*, 1989]; and 3) creep induced shear instabilities and melting where deformation of a material occurs rapidly enough compared to the timescale of thermal diffusion so that heat is accumulated in regions of high-strain and a positive feedback between deformation-induced heating and deformation leads to thermal runaway [*Karato et al.*, 2001]. There have been several attempts to use seismological parameters to constrain the faulting mechanism [*Frolich*, 1989; *Green II and Houston*, 1995] and the more recent studies [*Wiens*, 2001; *Karato et al.*, 2001] favor creep induced shear instabilities as the more probable mechanism for deep earthquake faulting.

Among other things, any mechanism that seeks to explain deep earthquake faulting should be able to explain the small radiation efficiencies and the differences in the observed seismological parameters between Bolivia and Russia-China earthquakes on the one hand, and the Flores and Fiji-Tonga earthquakes on the other. [*Wiens*, 2001, *Karato et al.*, 2001] argue that thermal shear instabilities would be able to explain most seismological observations. In creep induced thermal instabilities, temperature in a zone increases due to shear heating, but due to viscous dissipation, the width of this zone decreases gradually. However, at a critical width of the shear zone, the temperature increases explosively and the stress drops rapidly; this causes melting and thus induces slip in the shear zone, i.e., an earthquake [*Griggs and Baker*, 1968; *Ogawa*, 1990]. Since large deep earthquakes (e.g., the Bolivia earthquake) involved coseismic melting along narrow zones [*Kanamori et al.*, 1998], thermal instability is a plausible mechanism for these earthquakes.

Why do warmer slabs favor stress release through large earthquakes with high stress drops while colder slabs favor stress release through small earthquakes with smaller stress drops? [*Karato et al.*, 2001] suggest thermal runaway instabilities are facilitated by high strain rates and a large degree of thermal feedback. According to the thermal runaway model, colder slabs have higher strain rates (larger deformation) and hence will result in a large number of earthquakes (as observed in the Fiji-Tonga region). Though warmer slabs have smaller strain rates, once a sufficient amount of strain has been accumulated, a thermal instability can be initiated. Warmer slabs probably have a better thermal feedback mechanism due to the higher temperature in the slabs and hence once the instability is initiated it can cascade into a large earthquake. This would explain the infrequent large earthquakes in warm slabs. Moreover, since the temperature in warmer slabs is higher, the rupture mechanism would involve a large amount of melt and hence the growth of the fault would be a very dissipative process. However, thermal instability models depend strongly on the effects of temperature on slab rheology and these effects are not yet well understood. Such “creep rupture” [*Lawn*, 1993] is a vast area of study and further work is required to understand it better.

Differences between slabs could be due to differences in thermal parameter as mentioned earlier; however, some recent studies have suggested that the depth of penetration of slabs (i.e., age of subduction) and lower mantle structure could also control seismicity [*Gurnis et al.*, 2000; *Karato et al.*, 2001]. Another possibility is that different deep earthquake mechanisms operate in different slabs and this may result in differences in rupture processes as has been suggested by *Wiens and McGuire* [1995].

Tsunami Earthquakes

From Figure 4.7, we observe that tsunami earthquakes have small radiation efficiencies. Thus, these earthquakes dissipate a large amount of energy during the fracture process and are left with very little energy to radiate. Tsunami earthquakes are also known to have small rupture velocities and hence involve slow rupture [*Kanamori*, 1972; *Kanamori and Kikuchi*, 1993; *Polet and Kanamori*, 2000]. These earthquakes rupture the shallow portions of subduction zones resulting in a large amount of slip occurring very close to the ocean surface. To the first order, the size of a tsunami is proportional to the amount of water displaced at the tsunami source, which is proportional to the volume of the displaced ocean surface [*Kajiura*, 1970; *Kanamori*, 1972], thus, the large amount fault slip close to the ocean floor causes more displacement of the ocean floor and generates larger tsunamis than would be expected if the same amount of slip had occurred deeper. *Tanioka and Satake* [1996] and *Polet and Kanamori* [2000] also suggest that since the near surface structure plays a critical role in estimating the distribution of fault slip in tsunami events, the actual displacement on the ocean floor calculated from the seismic moment may be underestimated due to the presence of lateral heterogeneities that are usually not accounted for in seismic source inversions. Figures 4.8(a) and (b) show the ocean floor close to a trench at two different subduction zones.

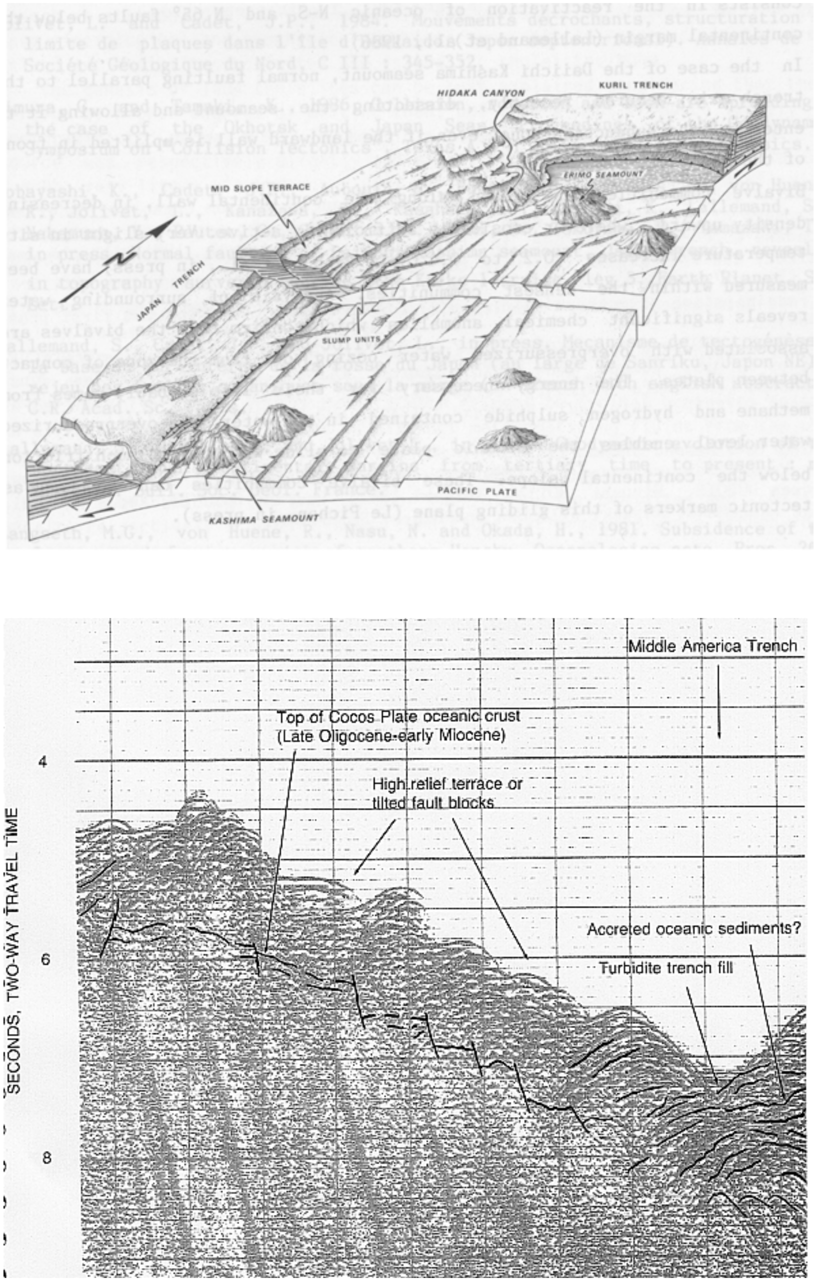

Figure 4.8(a) A perspective diagram of the Kurile and Japan trench illustrating the results of the Kaiko project (Cadet et al., 1986). The highly segmented ocean floor with horst and graben structures can be observed; **(b)** A multi-channel seismic profile of the trench off Nicaragua (Crowe and Buffler, 1985). The profile was shot very close to the location of the 1992 tsunami earthquake in Nicaragua; it can be observed that the ocean floor close to the trench is highly faulted, has a small accretionary prism and a thin sediment layer.

Most tsunami earthquakes rupture updip towards the trench in regions where the ocean floor close to the trench is highly faulted, has a small accretionary prism and a thin veneer of sediments [*Tanioka et al.*, 1997; *Polet and Kanamori*, 2000] (Figures 4.8(a) and (b)). The presence of sediments has been used to explain the slow character of these tsunami events. Our results suggest high fracture energy in tsunami earthquakes. It is probable that the highly faulted trench and deformed sediments results in larger energy dissipation during failure. It has been observed that highly damaged material has an excessive amount of branching and bifurcation of cracks which gives rise to inelastic behavior and hence a large dissipation of energy [*Barragan et al.*, 2001]. Moreover, in a recent study *Poliakov et al.* [2002] suggest that secondary failure in a damage zone causes the fracture energy to be much larger than when the rupture propagates along a single surface. Similarly, it is possible that the morphology of the trench causes branching and bifurcation of rupture resulting in the large energy dissipation during the rupture process of tsunami earthquakes.

Other Earthquakes - Rupture Velocity and Radiation Efficiency

Most crustal, interplate, downdip, intraplate and deep earthquakes have radiation efficiencies between 0.5 and 1 and are thus efficient in generating seismic waves. In these earthquakes, only a small fraction of the energy is dissipated in mechanical processes on the fault zone. Also, most earthquakes propagate at velocities close to the shear wave velocity.

In Chapter 3, we discussed the relationship between the ratio of rupture velocity and limiting rupture speed (V/c_L) and radiation efficiency that is obtained from crack theory and from simple energy considerations. We observed that the radiation efficiency was small for small V/c_L. For the earthquakes we studied, we observe a similar pattern. Most of these earthquakes have rupture velocities such that the ratio of rupture velocity to shear wave speed (V / β) is between 0.6 and 0.85 and for these earthquakes the radiation efficiency is between 0.3 and 1 (see Figure 4.7). However, the 1994 Bolivia earthquake, the 1999 Russia-China border event and the tsunami earthquakes, have small V / β and small radiation efficiencies.

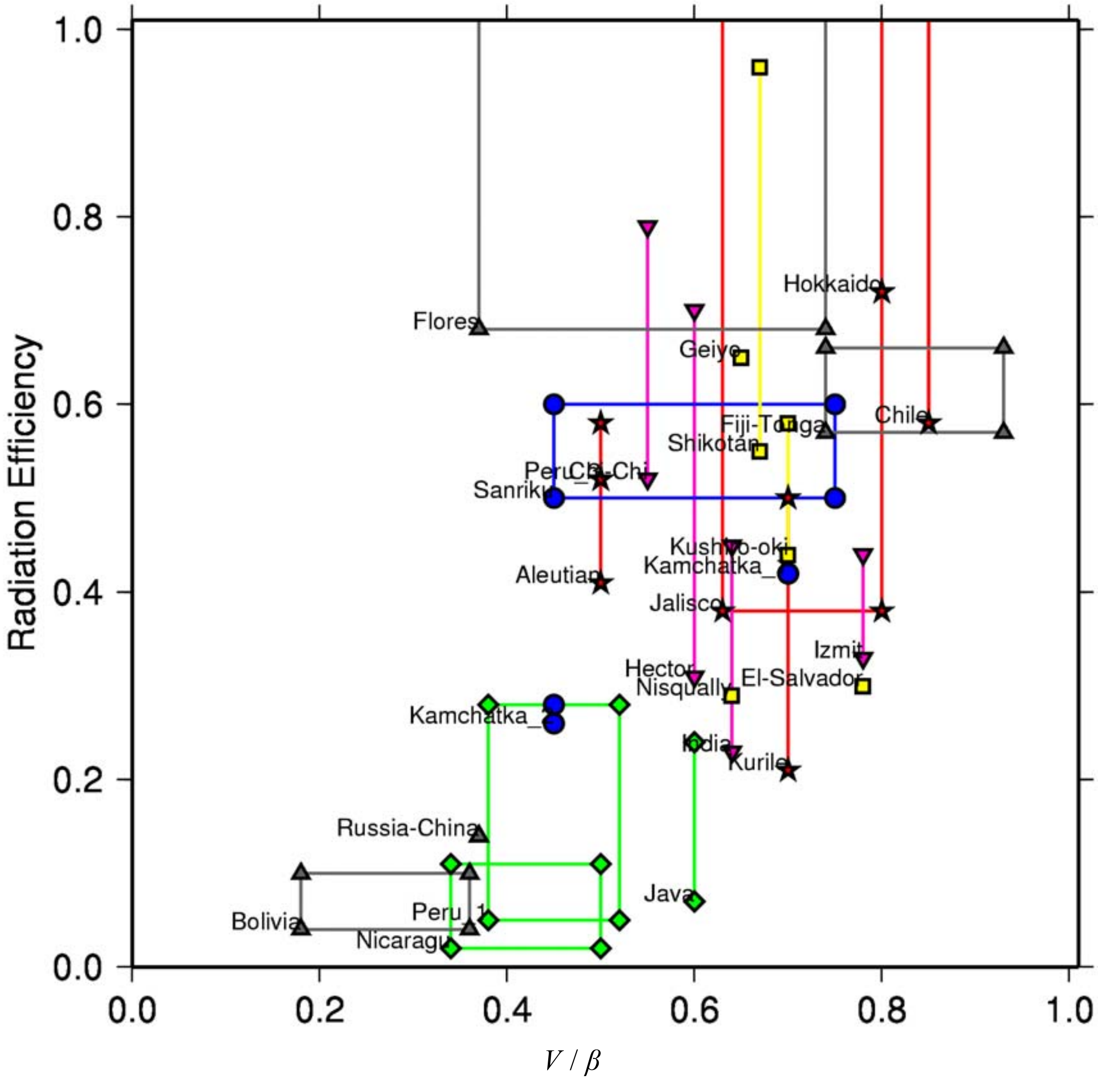

Figure 4.9 Radiation efficiencies determined from the radiated energy-to-moment ratios and estimates of static stress drop plotted against the estimates of the ratio of rupture velocity to shear wave velocity obtained from literature. Symbols are the same as before.

Figure 4.9 shows the radiation efficiencies determined in this study and rupture velocities obtained from literature for the earthquakes studied here. Average rupture velocities are usually determined from inversion of seismic waves and the results can be nonunique, but for most of the larger earthquakes, the estimates of rupture velocities are quite robust. For each earthquake, we plot the upper and lower limit of radiation efficiencies that were determined earlier and an upper and lower limit of the ratio of rupture velocities to shear wave velocities (V/β) obtained from literature. We did not plot earthquakes for which the radiation efficiencies are larger than 1 (discussed later).

Earlier, we assumed that in the model in Figure 4.5, the striped region represents fracture energy and hence this model can be used to calculate radiation efficiency. From crack theory, we know that the radiation efficiency is related to V/c_L by equations (3.18a) and (3.18b) in Chapter 3. In Figure 4.9, we plot computed estimates of radiation efficiencies and estimates of V/β determined from data and we observe that the radiation efficiencies are smaller for smaller V/β and larger for larger V/β, a relationship that we could expect from crack theory and from simple energy considerations. Since rupture velocity is an independently determined quantity, this consistency in the observed relationship between radiation efficiency and V/β on the one hand, and the calculations from crack theory on the other (shown in Figure 4.10), suggest that the model shown in Figure 4.5 is probably good for most earthquakes.

From the equation of motion, $G = 2\gamma$, where γ is the surface energy. If γ is independent of V, since G^* increases with crack length, for the equation of motion to be satisfied, $g(V)$ should decrease, i.e., V should increase with crack length (from equations (3.16) and (3.18)). This would imply that large earthquakes have large rupture velocity. However, if γ increases with V as a result of extensive plastic deformation near the crack tip, as has been experimentally demonstrated by *Rosakis and Zehnder*

[1985], V can be significantly lower than the shear wave velocity. Thus, under such conditions, we can have a large earthquake with a small rupture velocity.

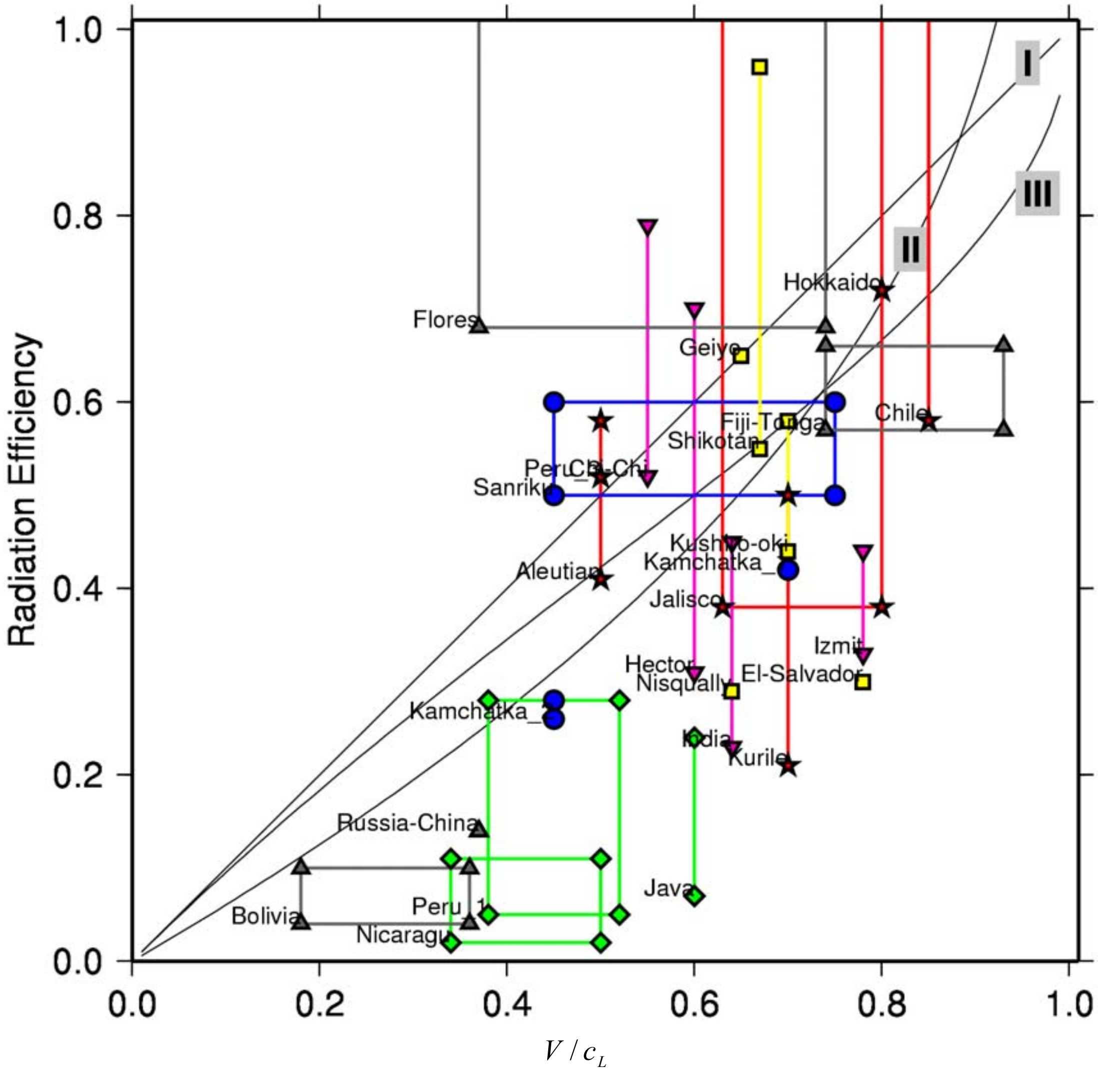

Figure 4.10 Same as Figure 4.9; for comparison, the theoretical curves relating radiation efficiency to rupture velocity for Mode I, Mode II and Mode III cracks have also been plotted.

Specific Fracture Energy

As mentioned in Chapter 3, fracture energy E_G can be determined estimates of radiated energy and static stress drop and from rupture velocities using equations (3.17) and (3.18). From both methods, the fracture energy for most large events is small–at most comparable to E_R. Since $E_G + E_R = \frac{1}{2}\Delta\sigma_S DS$ from Figure 4.5, the specific surface energy $G = E_G / S$ is at most of the order of

$$G = \frac{E_G}{S} \approx \frac{1}{2}\frac{(1/2)\Delta\sigma_S DS}{S} = \frac{1}{4}D\Delta\sigma_S$$

For large events assuming *D*=3 m, and $\Delta\sigma_S$ =30 bar, *G* is on the order of 2 MJ/m^2, which is the value often quoted in seismology. This value is much larger than that directly measured for crystals and metals, and should not be interpreted as the specific surface energy in the ordinary sense. It should be interpreted as energy dissipated in a large volume near the crack tip or in the breakdown zone. In a recent study by *Janssen et al.* [2001], the authors calculate the fractured energy involved in deformation of experimental samples using a formula: $G_f = 0.5G_G(\rho_C V_C + A_{mf})$, where G_f is the fracture energy, G_G is the specific fracture energy, ρ_C is the density of cracks and V_C is the volume of the fracture process zone (or breakdown zone) and A_{mf} is the fault area. Using a relationship like this would include the deformation in a volume around the crack tip and is probably a more appropriate method of calculating the specific fracture energy for earthquakes. Also, *Poliakov et al.* [2002], suggest that a part of the fracture energy is dissipated outside the main fault surface where there is secondary failure in the damage zone.

Static Stress Drops and Rupture Velocity

The estimates of static stress drop listed in Table 4.3 are based on determination of rupture area. Thus, if the static stress drop is constant, $M_0 \propto S^{3/2}$ [*Kanamori and Anderson*, 1975]. Stress drop can also be determined from the rupture duration if we assume that, $M_0 \propto \tau^{1/3}$, where τ is the rupture duration. This would imply that $S \propto \tau^2$. By using estimates of τ from literature, and assuming $S \propto \tau^2$, we determined estimates of static stress drop from τ. Figure 4.11 shows estimates of stress drop from area (as tabulated in Table 4.3) plotted against estimates of static stress drop from duration, τ. If the ratio of rupture velocity to shear wave speed (V/β) is between 0.65 and 0.85 (values observed for most earthquakes, e.g., *Heaton* [1990]), the estimates of stress drops from both methods should be similar. So, if we observe significant differences between the two estimates of static stress drops, it implies that there is something unusual about the rupture. From Figure 4.11 we observe that for most earthquakes, the two estimates of static stress drop are similar to within a factor of two. However, for the 1994 Bolivia earthquake and the tsunami earthquakes the stress drop estimates from rupture area is significantly larger than the estimate from duration, despite the possible errors in the estimates. This is indicative of the slow character of the rupture for these events, i.e., small rupture velocity. Rupture velocity is given as $V \approx \sqrt{S}/\tau$; in the Bolivia earthquake the area of rupture is very small compared to what would be expected for an earthquake of its magnitude, whereas the duration of rupture in the tsunami earthquakes is anomalously large. Thus, an independent measure of rupture velocity can be used to check the consistency of the estimates of stress drops.

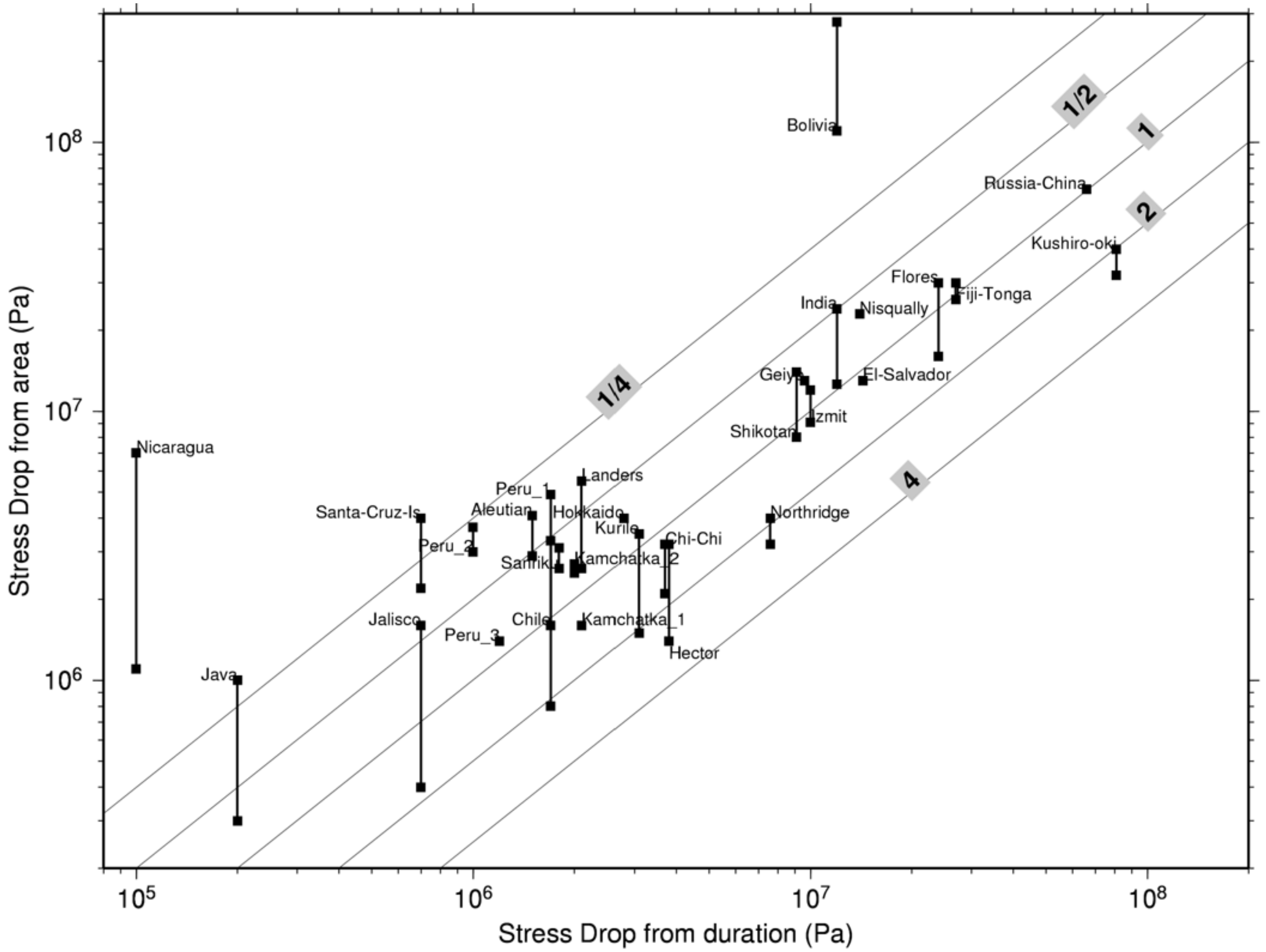

Figure 4.11 Static stress drops determined from rupture area and listed in Table 4.3 are plotted against static stress drops estimated from the rupture duration.

Small Earthquakes: What does the Stress Relaxation Model Imply?

Estimates of radiated energy of earthquakes show a change in the energy-to-moment ratio with earthquake size. Though the methods used to estimate radiated energy for these small earthquakes have large uncertainties associated with them, most studies suggest a change in the energy-to-moment ratio at $M_W \approx 4$ [*Abercrombie*, 1995; *Mayeda and Walter*, 1996]. If this observation is true, then what would it mean in terms of fracture energy? To answer this question, we have to know the stress drop. *Abercrombie* [1995] uses the duration to determine the static stress drop, but as was discussed in the Chapter 4, this method of measuring static stress drop is appropriate only if the ratio of rupture velocity to shear velocity is between 0.65 and 0.85. If we assume that this is true, then the static stress drop will be between 1-10MPa [*Abercrombie*, 1995]; if rigidity, $\mu = 3\times10^{10}\ \mathrm{N/m^2}$, for an energy-to-moment ratio, $\varepsilon = 10^{-6}\ \mathrm{to}\ 10^{-7}$, this would result in very small radiation efficiencies of 0.006 to 0.06. But small radiation efficiencies imply that the fracture energy is large and thus that the rupture velocity is small; this is contrary to the assumption involved in calculating stress drop from duration. Thus, the stress drop calculated from duration is not appropriate; either rupture velocity is smaller than usual or larger than usual. Since the rupture velocity in these earthquakes is already close to the shear wave velocity, the only possible explanation is that small earthquakes have smaller rupture velocities. This implies larger fracture energy and also small rupture area (since $V \approx \sqrt{S}/\tau$), this implies that the static stress drop for these small earthquakes should be large. A recent study by *Liu and Heaton* [2002] suggests that smaller earthquakes could have a larger variability of stress drops. Thus, it is possible that these small earthquakes have large static stress drops.

Earthquakes with radiation efficiency larger than 1?

How do we explain earthquakes with radiation efficiencies larger than 1? There are two possibilities; either the estimates of radiated energy and/or stress drops are inaccurate, or the model we use to calculate radiation efficiency is inappropriate. Despite the careful corrections we applied, the poor knowledge of the attenuation structure of the earth at higher frequencies could result in inaccuracies in the energy estimates. Also, as mentioned earlier, the estimates of static stress drop also have uncertainties. However, it is also possible that there is a stress undershoot (i.e., the final stress on the fault is larger than the residual frictional stress).

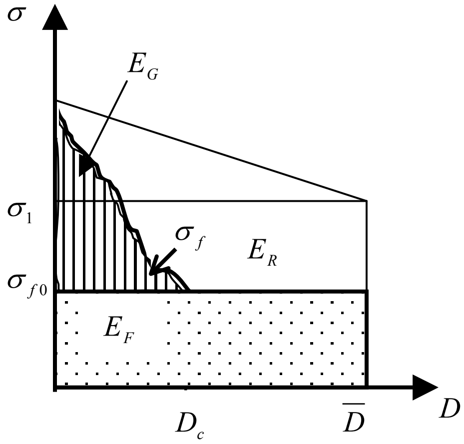

Figure 4.12 Undershoot model: The final stress on the fault is larger than the residual frictional stress on the fault. This could happen when the fault hits an obstacle and locks up prematurely.

In this case, from Figure 4.10, we can write

$$\begin{aligned}\eta_R &= \frac{E_R}{E_R + E_G} = \frac{E_R}{\Delta\sigma_S DS/2 + (\sigma_1 - \sigma_{f0})DS} \\ &= \frac{E_R / M_0}{\frac{\Delta\sigma_S}{2\mu}(1 + \frac{(\sigma_1 - \sigma_{f0})DS}{\Delta\sigma_S})} \\ &= \frac{\eta'_R}{(1 + \frac{(\sigma_1 - \sigma_{f0})DS}{\Delta\sigma_S})},\end{aligned}$$

where $\eta'_R = \frac{E_R / M_0}{\Delta\sigma_S / 2\mu}$ is the radiation efficiency calculated from the radiated energy-to-moment ratio and strain drops. Thus

$$\eta'_R = (1 + \frac{2(\sigma_1 - \sigma_f)}{\Delta\sigma_S})\eta_R ,$$

and hence is there is a stress undershoot, it is possible that $\eta'_R > 1$ and this could explain our observations. Moreover, if the rupture propagates as a slip pulse [*Heaton,* 1990], we would expect an undershoot model of stress relaxation. Some studies suggest that the Landers earthquake (1992) and the Northridge earthquake (1994) data are better explained by slip pulse models; however, further investigations are required to understand the undershoot model.

It is also possible that there is a stress overshoot as shown in Figure 4.13.

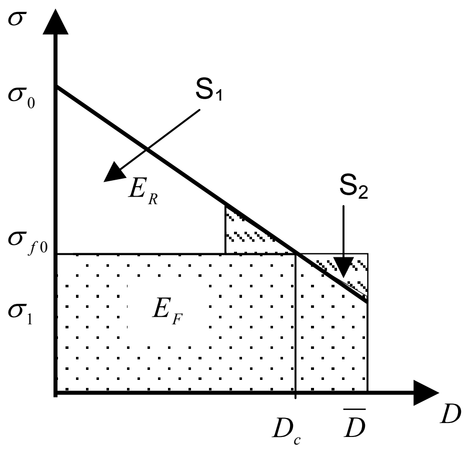

Figure 4.13 Overshoot model: The final stress on the fault is smaller than the residual frictional stress on the fault. This could happen when the fault motion is such that it overshoots the equilibrium.

When there is a stress overshoot,

$$\begin{aligned}\tilde{e} = \frac{E_R}{M_0} &= \frac{1}{\mu}(\frac{\sigma_0 + \sigma_1}{2} - \sigma_{f0}) \\ &= \frac{1}{\mu}(\frac{\Delta\sigma_S}{2} + (\sigma_1 - \sigma_{f0})) < \frac{\Delta\sigma_S}{2\mu}\end{aligned}$$

So, if the overshoot were large, the radiated energy would be small. *Madariaga* [1976] and *Kostrov and Das* [1988] show that overshoot does not exceed 0.3, i.e.,

$$\frac{(\sigma_0 - \sigma_{f0})}{(\sigma_{f0} - \sigma_1)} = \frac{D_c}{\overline{D}} = 0.3$$

$$\frac{S_1}{S_2} = 0.09$$

S_1 is the area of the top triangle in Figure 4.13 and S_2 is the area of the shaded triangle. Thus, the effect of stress overshoot on the estimates of radiation efficiency is negligible.

4.6 Conclusions

We compute teleseismic estimates of radiated energy for 23 large subduction zone earthquakes; most of these earthquakes have $M_w > 7.5$, but we also included some smaller well-studied earthquakes. For comparison, we include 6 crustal earthquakes. We observe that the radiated energy-to-moment ratio is different for different types of earthquakes; tsunami earthquakes have the smallest radiated energy-to-moment ratio (7×10^{-7} to 3×10^{-6}), interplate and downdip earthquakes have a slightly larger ratio (5×10^{-6} to 2×10^{-5}) and intraplate and deep earthquakes have ratios similar to crustal earthquakes (2×10^{-5} to 3×10^{-4}).

We also compiled the static stress drop estimates for these 29 earthquakes from literature. From the seismic moment, radiated energy and static stress drop values we calculate the radiation efficiency for these earthquakes and interpret our results in the light of differences in rupture mechanisms. We observe that most earthquakes have large radiation efficiencies between 0.25 and 1, while tsunami earthquakes and some deep earthquakes like the 1994 Bolivia earthquake and the 1999 Russia-China earthquake have small radiation efficiencies (<0.25) and hence dissipate a large amount of energy on the fault plane. We discuss the possible reasons for this difference in the radiation efficiencies of tsunami earthquakes and the deep Bolivian earthquake and suggest that they could be due to fundamental differences in the rupture mechanics of different events. In case of deep events, the energy is probably dissipated in thermal processes on the fault zone, while it is possible that the morphology of the trench causes branching and bifurcation of rupture resulting in the large energy dissipation during the rupture process of tsunami earthquakes.

CHAPTER 5

Conclusions

In this thesis, we develop a new method of estimating radiated energy from regional data using an empirical Green's function method and use this method to determine the radiated energy for the Hector Mine earthquake. Since the regional estimates of radiated energy for the Hector Mine earthquake are robust, they constitute an important data point for studies involving the radiated energy. Moreover, with better data quality, the empirical Green's function method can be extended to study smaller events. We also modify existing methods of estimating radiated energy from teleseismic data by improving the corrections applied to the observed seismic data for attenuation and directivity effects and use this modified method to determine radiated energy for the Hector Mine earthquake and other large earthquakes. For the Hector Mine earthquake, we observe that the regional estimates are almost the same as the teleseismic estimates. Thus, this event could serve as a calibration for future studies of radiated energy using regional and teleseismic data.

To investigate the differences between the different types of subduction zone earthquakes and to understand the rupture mechanics these earthquakes, we use macroscopic source parameters: radiated seismic energy, seismic moment, rupture area and rupture velocity. The advantage of using such macroscopic parameters is that they reflect the overall frictional conditions on the fault; we do not have to determine the details of the rupture processes on the fault plane. Using the modified teleseismic method, we compute teleseismic estimates of radiated energy for 23 large subduction zone earthquakes; most of these earthquakes have $M_w > 7.5$, but we also included some smaller well-studied earthquakes. For comparison, we include 6 crustal earthquakes. We observe that the radiated energy-to-moment ratio is different for different types of earthquakes; tsunami earthquakes have the smallest radiated energy-to-moment ratio (7×10^{-7} to 3×10^{-6}), interplate and downdip earthquakes have a slightly larger ratio (5×10^{-6} to 2×10^{-5}) and intraplate and deep earthquakes have ratios similar to crustal earthquakes (2×10^{-5} to 3×10^{-4}).

Subsequently, we use a stress relaxation model to understand the partitioning of energy in earthquakes and hence relate the macroscopic parameters such as radiated energy, seismic moment, and static stress drop to radiation efficiency and fracture energy. Since fracture energy is directly related to the physical processes on the fault zone, this parameter can be used to understand the dynamics of faulting. To use this model, we compiled the static stress drop estimates for these 29 earthquakes from literature. From the seismic moment, radiated energy and static stress drop values, we calculate the radiation efficiency for these earthquakes and interpret our results in the light of differences in rupture mechanisms.

We observe that most earthquakes have large radiation efficiencies between 0.25 and 1, while tsunami earthquakes and some deep earthquakes, like the 1994 Bolivia earthquake and the 1999 Russia-China earthquake, have small radiation efficiencies (<0.25) and hence dissipate a large amount of energy on the fault plane. We discuss the possible reasons for this difference in the radiation efficiencies of tsunami earthquakes and the deep Bolivian earthquake and suggest that they could be due to fundamental differences in the rupture mechanics of different events. In case of deep events, the energy is probably dissipated in thermal processes on the fault zone, while it is possible that the morphology of the trench causes branching and bifurcation of rupture resulting in the large energy dissipation during the rupture process of tsunami earthquake.

We also compile the rupture velocities for these 29 earthquakes from literature and plot the radiation efficiency against the ratio of rupture velocity to shear wave velocity (V/β). Since rupture velocity is an independently determined quantity, consistency in the observed relationship between radiation efficiency and V/β on the one hand, and the calculations from crack theory on the other hand, suggest that the stress relaxation model that we use is probably good for most earthquakes.

Thus, we have better radiated energy estimates of larger events and with better data quality, the empirical Green's function method can be extended to study smaller events; thus, with the increasing number of downhole stations, better instrumentation and greater knowledge of the earth's structure it will become possible to improve the estimates of radiated energy from smaller earthquakes and understand the differences between the rupture mechanics of small and large earthquakes. Moreover, we also show that estimates of E_R/M_0 alone cannot be used to understand earthquake mechanics; we have to go one step further and use a stress relaxation model along with the macroscopic seismic parameters – radiated energy, seismic moment, rupture area and rupture velocity to understand the differences in the rupture mechanics of earthquakes.

Appendix A

Attenuation Corrections Applied to Observed Data

To estimate the attenuation correction, we use frequency dependent t^* models that are derived from the models *Der* [1998]. Here, we briefly outline the procedure we use to determine the t^* models. As attenuation of seismic energy is dominated by near surface effects, we decide to broadly account for the differences in the crustal structure beneath seismic stations. We divide all the teleseismic stations into two categories: shield stations and tectonic stations, based on a seismic tomography model (*S20RTS, Ritsema* [1999]). Stations that lie within regions 4 percent faster than *PREM* at 120 km are denoted as shield stations; all other stations are tectonic. For the shield stations, we use the *QP S-T* model of *Der* [1998], while for the tectonic stations we use a model that is obtained by combining the *QP S-T* and *QP S-S* models. The long period t^* at each station is determined by using the velocity and *Q* structure for the western US given by *Archambeau et al.* [1969]. Using this initial t^* and the appropriate frequency dependent t^* model, we apply a frequency dependent t^* correction at each station (see figure).

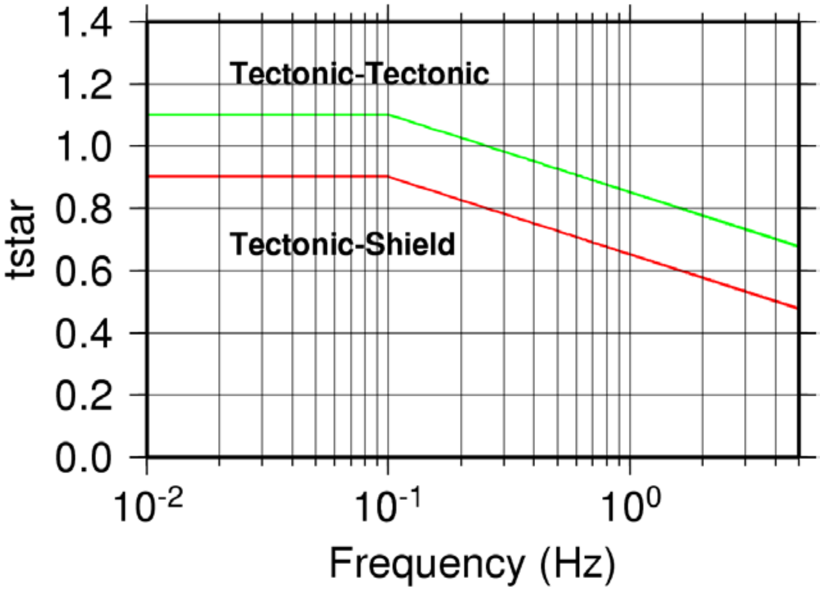

Figure A1 This is a plot of t^* models: the plot shows the variation of t^* with frequency for tectonic and shield stations at a distance of 50^0 from the source. We also include a slight distance dependence of t^*; for tectonic stations t^* varies from 0.87 at 30^0 to 0.79 at 90^0, whereas for shield stations t^* varies from 0.67 at 30^0 to 0.59 at 90^0.

Appendix B

Plots of Energy-to-moment Ratios

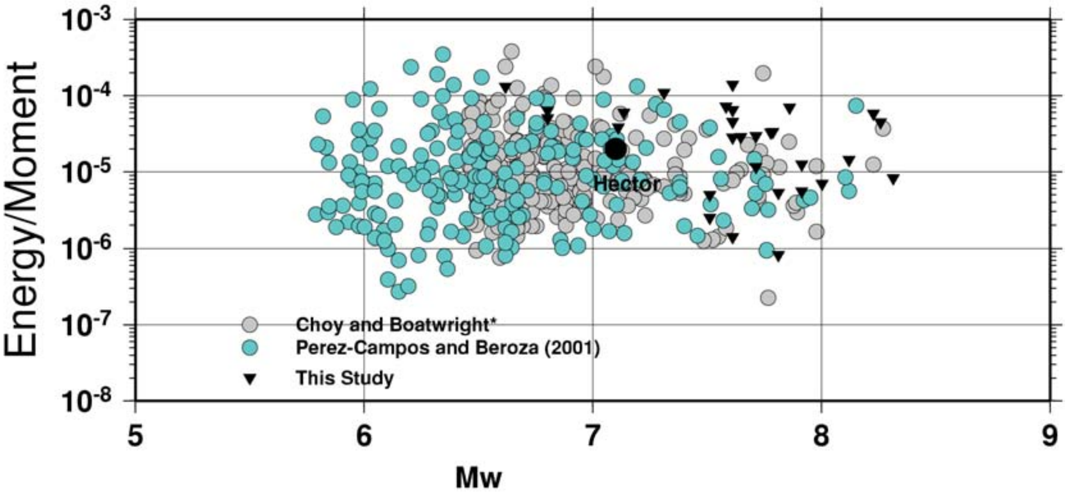

Figure B1 Plot of teleseismic estimates of radiated energy-to-moment ratios: comparison with other studies.

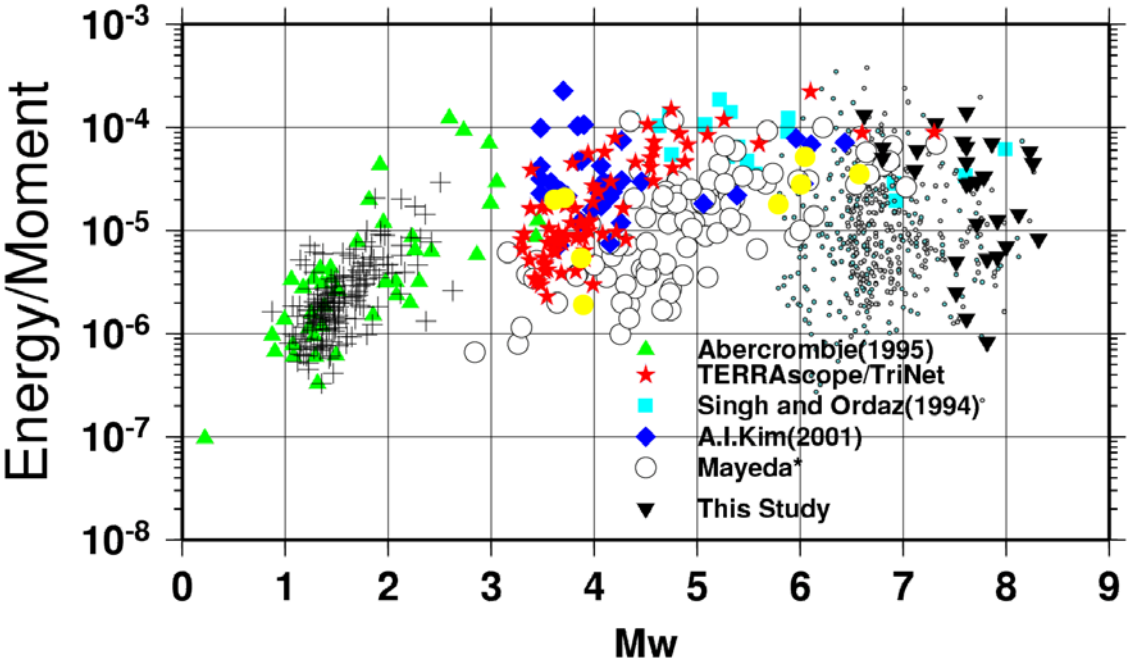

Figure B2 Plot of regional and teleseismic estimates of radiated energy-to-moment ratios obtained by different investigators.

Appendix C

Plots of Energy-density Spectra

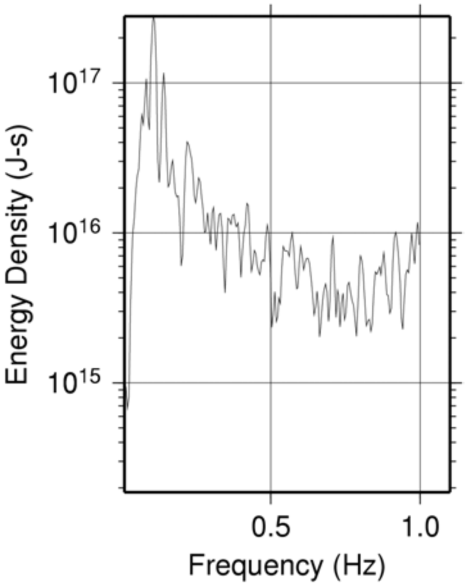
(a) 930712-Hokkaido

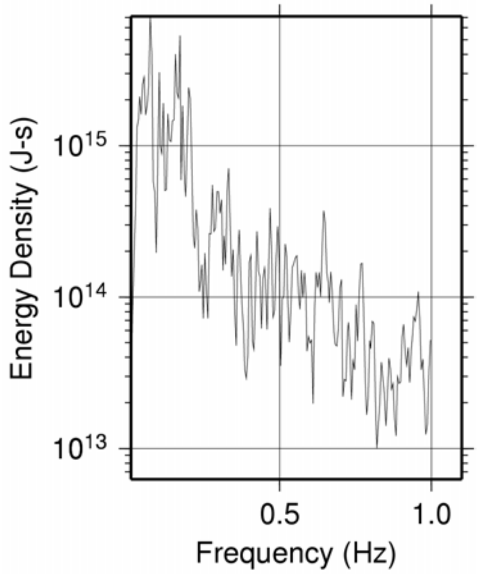
(b) 920902-Nicaragua

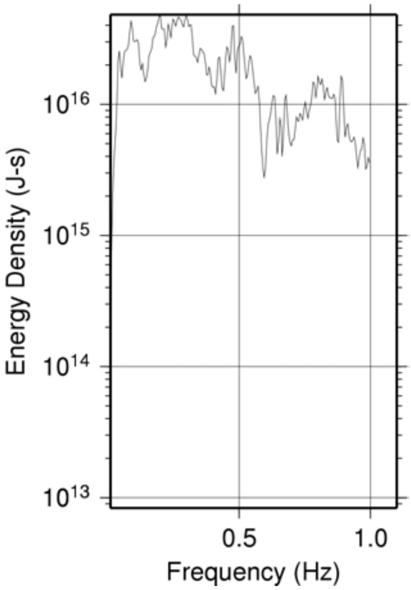
(c) 940309-Fiji

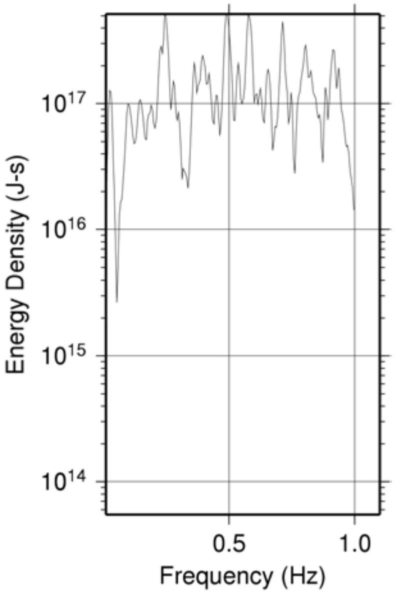
(d) 940609-Bolivia

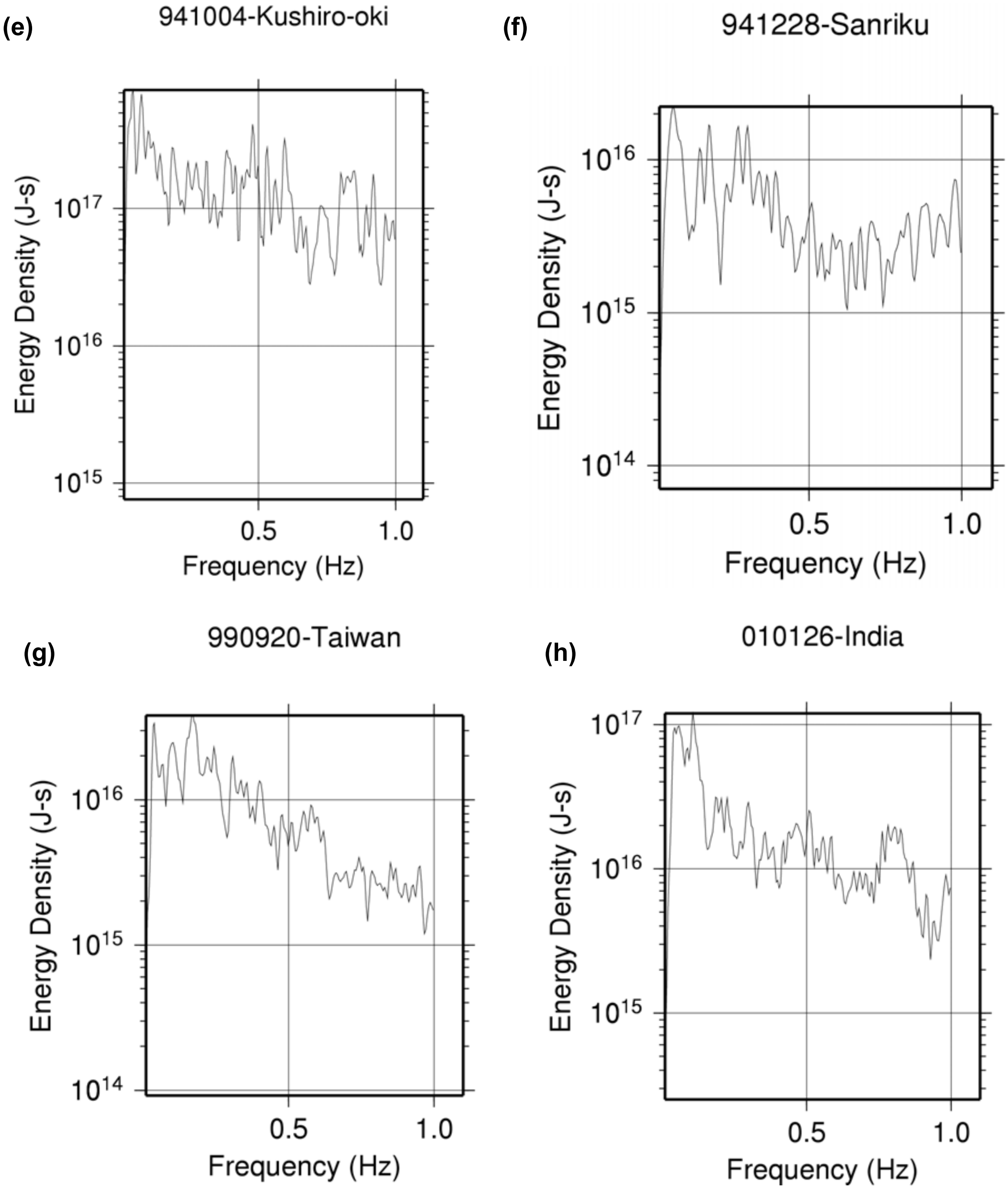

Figure C Teleseismic average energy-density spectra: **(a)** 920902-Nicaragua tsunami earthquake; **(b)** 930712-Hokkaido interplate earthquake; **(c)** 940309-Fiji-Tonga deep earthquake; **(d)** 940609 -Bolivia deep earthquake; **(e)** 941004-Kushiro-oki interplate earthquake; **(f)** 941228-Sanriku downdip earthquake; **(g)** 990920-Taiwan crustal earthquake; **(h)** 010126-India crustal earthquake.

References

Abercrombie, R., Earthquake source scaling relationships from -1 to 5 ML using seismograms recorded at 2.5 km depth, *J. Geophys. Res.*, *100*, 24,015-24,036, 1995.

Abercrombie, R., M. Antolik, K. Felzer, and G. Ekstrom, The 1994 Java tsunami earthquake: slip over a subducting seamount, *J. Geophys . Res.*, *106* (B4), 6595-6607, 2001.

Abercrombie, R., and P. Leary, Source parameters of small earthquakes recorded at 2.5 km depth, Cajon Pass, Southern California: Implications for earthquake scaling, *Geophys. Res. Lett.*, *20*, 1511-1514, 1993.

Aki, K., Generation and propagation of G waves from the Niigata earthquake of June 16, 1964. Part 2. Estimation of earthquake moment, from the G wave spectrum, *Bull. Earthquake Res. Inst. Tokyo Univ.*, *44*, 73-88, 1966.

Aki, K., Earthquake mechanism, *Tectonophysics*, *13* (1-4), 423-446, 1972.

Archambeau, C. B., E. A. Flinn and D. G. Lambert, (1969). Fine Structure of the Upper Mantle, J. Geophys. Res. 74, 5825-5865.

Barragan, B. E., G. M. Giaccio, and R. L. Zerbino, Fracture and failure of thermally damaged concrete under tensile loading, *Materials and structures*, *34*, 312-319, 2001.

Bath, M., Earthquake energy and magnitude, in *Contributions in Geophysics: In Honor of Beno Gutenberg*, edited by M. E. H. Benioff, B. F. Howell Jr., and F. Press, Pergamon Press, New York, 1966.

Boatwright, J., and G. L. Choy, Teleseismic estimates of the energy radiated by shallow earthquakes, *J. Geophys. Res.*, *91*, 2095-2112, 1986.

Boatwright, J., G. L. Choy, and L. C. Seekins, Regional estimates of the radiated seismic energy, *Bull. Seis. Soc. Am.* (in press), 2002.

Boatwright, J., and M. Cocco, Frictional constraints on crustal faulting, *J. Geophys. Res.*, *101* (B6), 13,895-13,909, 1996.

Boatwright, J., and J. B. Fletcher, The partition of radiated energy between P and S waves, *Bull. Seis. Soc. Am.*, *74*, 361-376, 1984.

Boore, D. M., and J. Boatwright, Average body-wave radiation coefficients, *Bull. Seis. Soc. Am.*, *74* (5), 1615-1621, 1984.

Boore, D. M., and S.W. Dunbar, Effect of the free surface on calculated stress drops, *Bull. Seis. Soc. Am.*, *67* (6), 1661-1664, 1977.

Brodsky, E. E., and H. Kanamori, The elastohydrodynamic lubrication of faults, *J. Geophys. Res.*, *106*, 16,357-16,375, 2001.

Brune, J., Tectonic stress and spectra of seismic shear waves from earthquakes-Correction, *J . Geophys . Res.*, *76*, 5009, 1971.

Brune, J. N., Tectonic stress and spectra of seismic shear waves from earthquakes, *J. Geophys. Res.*, *75*, 4997-5009, 1970.

Cadet, J. P., K. Kobayashi, S. Lallemand, and L. Jolivet, Subduction in the Japan trench: The Kaiko results, in *The Origin of Arcs*, edited by F.-C. Wezel, pp. 461-481, Elsevier, New York, 1986.

Carlo, D. L., T. Lay, C. J. Ammon, and J. Zhang, Rupture Process of the 1995 Antofagasta Subduction Earthquake (M_w = 8.1), *Pure Appl. Geophys.*, *154* (3-4), 677-708, 1999.

Choy, G. L., and J. L. Boatwright, Global patterns of radiated energy and apparent stress, *J. Geophys. Res.*, *100*, 18205-18228, 1995.

Courboulex, F., S. K. Singh, J. Pacheco, and C. J. Ammon, The October 9, 1995 Colima-Jalisco, Mexico earthquake (M_w 8): A study of the rupture process, *Geophys. Res. Lett.*, *24*, 1019-1022, 1997.

Crowe, J. C., and R. T. Buffler, Multichannel seismic records across the Middle America Trench and Costa Rica-Nicaragua convergent margin, NCY-7 and NIC-1, in *Middle America Trench off Western Central America*, edited by J. W. Ladd, and R. T. Buffler, pp. 11, Woods Hole, Mass., 1985.

Dahlen, F. A., The balance of energy in earthquake faulting, *Geophys. J. R. Astr. Soc.*, *48*, 239-261, 1977.

Das, S., Relation between average slip and average stress drop for rectangular faults with multiple asperities, *Bull. Seis. Soc. Am.*, *78* (2), 924-930, 1988.

Der, Z. A., High frequency *P* and *S* wave attenuation in the earth, *Pageoph*, *153*, 273-310, 1998.

Dreger, D. S., Investigation of the rupture process of the 28 June 1992 Landers earthquake utilizing TERRAscope, *Bull. Seis. Soc. Am.*, *84*, 713-724, 1994.

Eshelby, J. D., The determination of the elastic field of an ellipsoidal inclusion and related problems, *Proceedings of the Royal Soc. London*, *241*, 376-396, 1957.

Eshelby, J. D., The elastic field of a crack extending non-uniformly under general anti-plane loading, *J. Mech. Phys. Solids*, *17*, 177-199, 1969.

Fossum, A. F., and L. B. Freund, Nonuniformly moving shear crack model of a shallow focus earthquake mechanism, *J . Geophys . Res.*, *80*, 3343-3347, 1975.

Frankel, A., and H. Kanamori, Determination of rupture duration and stress drop for earthquakes in southern California, *Bull. Seis. Soc. Am.*, *73*, 1527-1551, 1983.

Freund, L. B., Crack propagation in an elastic solid subjected to general loading. II. Nonuniform rate of extension, *J. Mech. Phys. Solids*, *20*, 141-152, 1972a.

Freund, L. B., Energy flux into the tip of an extending crack in an elastic solid, *J. Elasticity*, *2*, 341-349, 1972b.

Frolich, C., The nature of deep-focus earthquakes, *Ann. Rev. Earth and Planetary Sciences*, *17*, 227-254, 1989.

Giardini, D., Frequency distribution and quantification of deep earthquakes, *J. Geophys . Res.*, *93* (B3), 2095-2105, 1988.

Goes, S., and J. Ritsema, A broadband *P* wave analysis of the large deep Fiji Island and Bolivia earthquakes of 1994., *Geophys. Res. Lett.*, *22* (16), 2249-2252, 1995.

Goes, S., L. J. Ruff, and N. W. Winslow, The complex rupture process of the 1996 deep Flores, Indonesia earthquake (M_w 7.9) from teleseismic P-waves, *Geophys. Res. Lett.*, *24* (11), 1295-1298, 1997.

Green II, H. W., and H. Houston, The mechanics of deep earthquakes, *Ann. Rev. Earth & Planetary Sciences*, *23*, 169-213, 1995.

Green II, H. W., and P. C., Burnley, A new self-organizing mechanism for deep-focus earthquakes, *Nature*, *341*, 733-737, 1989.

Griggs, D. T., and D. W. Baker, The origin of deep-focus earthquakes, in *Properties of matter under unusual conditions: in honor of Edward Teller's 60th birthday*, edited by M. Hans, and F. Sidney, pp. 23-42, John Wiley, New York, 1968.

Guatteri, M., and P. K. P. Spudich, What can strong-motion data tell us about slip-weakening fault-friction laws?, *Bull. Seis. Soc. Am.*, *90* (1), 98-116, 2000.

Gurnis, M., J. Ritsema, and H. J. van Heijst, Tonga slab deformation: the influence of a lower mantle upwelling on a slab in a young subduction zone, *Geophys. Res. Lett.*, *27* (16), 2373-2376, 2000.

Gutenberg, B., Earthquake magnitude, intensity, energy, and acceleration, *Bull. Seis. Soc. Am.*, *32*, 163-191, 1942.

Gutenberg, B., The energy of earthquakes, *Quarterly J. Geological Soc. London*, *112*, 1-14, 1956.

Gutenberg, B., and C. F. Richter, Depth and geographical distribution of deep-focus earthquakes, *Bull. Geol. Soc. Am.*, *49*, 249-288, 1938.

Gutenberg, B., and C. F. Richter, Depth and geographical distribution of deep-focus earthquakes, *Bull. Geol. Soc. Am.*, *50*, 1511-1528, 1939.

Gutenberg, B., and C. F. Richter, Earthquake magnitude, intensity, energy, and acceleration, *Bull. Seis. Soc. Am.*, *46*, 105-145, 1956a.

Gutenberg, B., and C. F. Richter, Magnitude and energy of earthquakes, *Ann. Geofis. Rome*, *9*, 1-15, 1956b.

Hartog, J. R., and S. Y. Schwartz, Directivity analysis of the December 28, 1994 Sanriku-oki earthquake (M_w=7.7), Japan, *Geophys. Res. Lett.*, *23* (16), 2037-2040, 1996.

Hartzell, S., Earthquake aftershocks as Green's functions, *Geophys. Res. Lett.*, *5*, 1-4, 1978.

Haskell, N., Total energy and energy spectral density of elastic wave radiation from propagating faults, *Bull. Seis. Soc. Am.*, *56*, 1811-1842, 1964.

Hauksson, E., L. M. Jones, and L. K. Hutton, The 1999 M_w7.1 Hector Mine, California earthquake sequence: Complex conjugate strike-slip faulting, *Bull. Seis. Soc. Am.* (in press), 2002.

Heaton, T., Evidence for and implications of self-healing pulses of slip in earthquake rupture, *Physics of the Earth and Planetary Interiors*, *64*, 1-20, 1990.

Heki, K., S. Miyazaki, and T. Hiromichi, Silent fault slip following an interplate thrust earthquake at the Japan trench, *Nature*, *386* (6625), 595-598, 1997.

Hisada, Y., An efficient method for computing Green's functions for a layered half-space with sources and receivers at close depths, *Bull. Seis. Soc. Am.*, *84* (5), 1456-1472, 1994.

Houston, H., Broadband source spectrum, seismic energy, and stress drop of the 1989 Macquarie ridge earthquake, *Geophys. Res. Lett.*, *17*, 1021-1024, 1990a.

Houston, H., A comparison of broadband source spectra, seismic energies, and stress drops of the 1989 Loma Prieta and 1988 Armenian earthquakes, *Geophys. Res. Lett.*, *17*, 1413-1416, 1990b.

Houston, H., and H. Kanamori, Comparison of strong motion spectra with teleseismic spectra for three magnitude 8 subduction-zone earthquakes, *Bull. Seis. Soc. Am.*, *80*, 913-934, 1990.

Hurukawa, N., The 1995 Off-Etorofu earthquake: joint relocation of foreshocks, the mainshock, and aftershocks and implications for the earthquake nucleation process., *Bull. Seis. Soc. Am.*, *88* (5), 1112-1126, 1998.

Husseini, M. I., Energy balance for formation along a fault, *Geophys. J. R. Astr. Soc.*, *49*, 699-714, 1977.

Hutton, W., C. DeMets, O. Sanchez, G. Suarez, and J. Stock, Slip kinematics and dynamics during and after the 1995 October 9 Mw=8.0 Colima-Jalisco earthquake, Mexico, from GPS geodetic constraints, *Geophys. J. Int.*, *146*, 637-658, 2001.

Ida, Y., Cohesive force across the tip of a longitudinal-shear crack and Griffith's specific fracture energy, *J . Geophys . Res.*, *77*, 3796-3805, 1972.

Ida, Y., Stress concentration and unsteady propagation of longitudinal shear cracks, *J . Geophys . Res.*, *78*, 3418-3429, 1973.

Ide, S., and M. Takeo, Determination of constitutive relations of fault slip based on seismic wave analysis, *J. Geophys. Res.*, *102*, 27,379-27,391, 1997.

Ihmle, P. F., Monte Carlo slip inversion in the frequency domain: application to the 1992 Nicaragua slow earthquake, *Geophys. Res. Lett.*, *23* (9), 913-916, 1996.

Ihmle, P. F., J. Gomez, P. Heinrich, and S. Guibourg, The 1996 Peru tsunamigenic earthquake: broadband source processes., *Geophys. Res. Lett.*, *25* (14), 2691-2694, 1998.

Janssen, C., F. C. Wagner, A. Zang, and G. Dresen, Fracture process zone in granite: a microstructural analysis, *International Journal of Earth Sciences*, *90*, 46-59, 2001.

Ji, C., D. V. Helmberger, D. J. Wald, and K.-F. Ma, Slip history and dynamic implications of the 1999 Chi-Chi, Taiwan earthquake, *J . Geophys . Res.*, *in press*, 2002.

Ji, C., D. J. Wald, and D. V. Helmberger, Source description of the 1999 Hector Mine, California earthquake; Part II: Complexity of slip history, *Bull. Seis. Soc. Am.* (in press), 2002b.

Johnson, J. M., Y. Tanioka, K. Satake, and L. J. Ruff, Two 1993 Kamchatka earthquakes, *Pure Appl. Geophys.*, *144* (3/4), 633-647, 1995.

Jones, L., and D. V. Helmberger, Earthquake source parameters and fault kinematics in the eastern California shear zone, *Bull. Seis. Soc. Am.*, *88*, 1337-1352, 1998.

Kajiura, K., Tsunami source, energy and the directivity of wave radiation, *Bull. Earthq. Res. Inst. Tokyo Univ.*, *48*, 835-869, 1970.

Kanamori, H., Mechanism of tsunami earthquakes, *Phys. Earth Planet. Inter.*, *6*, 346-359, 1972.

Kanamori, H., The energy release in great earthquakes, *J. Geophys. Res.*, *82*, 2981-2876, 1977.

Kanamori, H., Mechanics of Earthquakes, *Ann. Rev. Earth & Planetary Sciences*, *22*, 207-237, 1994.

Kanamori, H., and C. R. Allen, Earthquake repeat time and average stress drop., in *[Monograph] Earthquake source mechanics.*, edited by S. Das, J. Boatwright, and C. Scholz, pp. 227-235, American Geophysical Union, Washington, D.C., 1986.

Kanamori, H., and D. L. Anderson, Theoretical basis of some empirical relations in seismology, *Bull. Seis. Soc. Amer.*, *65* (5), 1073-1095, 1975.

Kanamori, H., T. H. Anderson, and T. H. Heaton, Frictional melting during the rupture of the 1994 Bolivian Earthquake, *Science*, *279*, 839-842, 1998.

Kanamori, H., E. Hauksson, L. K. Hutton, and L. M. Jones, Determination of earthquake energy release and M_L using TERRAscope, *Bull. Seis. Soc. Am.*, *83*, 330-346, 1993.

Kanamori, H., and T. Heaton, Microscopic and Macroscopic Mechanisms of Earthquakes, in *AGU Monograph Series, Physics of Earthquakes*, edited by J. Rundle, D. L. Turcotte, and W. Klein, American Geophysical Union, Washington, D. C., 2000.

Kanamori, H., and M. Kikuchi, The 1992 Nicaragua earthquake: a slow tsunami earthquake associated with subducted sediments., *Nature*, *361*, 714-716, 1993.

Kanamori, H., and G. J. Stewart, Seismological aspects of the Guatemala earthquake of February 4, 1976, *Geophys. Res.*, *83* (B7), 3427-3434, 1978.

Karato, S., M. R. Riedel, and D. A. Yuen, Rheological structure and deformation of subducted slabs in the mantle transition zone: implications for mantle circulation and deep earthquakes, *Phys. Earth Planet. Inter.*, *127*, 83-108, 2001.

Kaverina, A., D. Dreger, and M. Antolik, Source process of the 21 April, 1997 Santa Cruz Island earthquake (Mw 7.8). *Geophys. Res. Lett.*, *25* (21), 4027-4030, 1998.

Keilis-Borok, V., On estimation of the displacement in an earthquake source and of source dimensions, *Ann. Geofis. Rome*, *12*, 205-214, 1959.

Kikuchi, M., Strain drop and apparent strain for large earthquakes, *Tectonophysics*, *211*, 107-113, 1992.

Kikuchi, M., and Y. Fukao, Seismic wave energy inferred from long-period body wave inversion, *Bull. Seis. Soc. Am.*, *78*, 1707-1724, 1988.

Kikuchi, M., and H. Kanamori, Inversion of complex body waves - III, *Bull. Seismol. Soc. Amer.*, *81*, 2335-2350, 1991.

Kikuchi, M., and H. Kanamori, The mechanism of the deep Bolivia earthquake of June 9, 1994., *Geophys. Res. Lett.*, *21* (22), 2341-2344, 1994.

Kikuchi, M., and H. Kanamori, The Shikotan earthquake of October 4, 1994: lithospheric earthquake, *Geophys. Res. Lett.*, *22* (9), 1025-1028, 1995a.

Kikuchi, M., and H. Kanamori, Source characteristics of the 1992 Nicaragua tsunami earthquake inferred from teleseismic body waves, *Pure Appl. Geophys.*, *144*, 441-453, 1995b.

Kisslinger, C., and M. Kikuchi, Aftershocks of the Adreanof Islands earthquake of June 10, 1996, and local seismotectonics, *Geophysical Research Letters*, *24* (15), 1883-1886, 1997.

Knopoff, L., Energy release in earthquakes, *Geophys. Jour.*, *1*, 44-52, 1958.

Kostrov, B. V., Unsteady propagation of longitudinal shear cracks, *J. Appl. Math. Mech. (transl. P. M. M.)*, *30*, 1241-1248, 1966.

Kostrov, B. V., Seismic moment and energy of earthquakes, and seismic flow of rock (translated to English), *Izv. Earth Physics*, *1*, 23-40, 1974.

Kostrov, B. V., and S. Das, *Principles of Earthquake Source Dynamics*, 286 pp., Cambridge University Press, Cambridge, 1988.

Lawn, B., *Fracture of Brittle Solids-Second Edition*, 378 pp., Cambridge University Press, Cambridge, 1993.

Li, V. C., Mechanics of shear rupture applied to earthquake zones., in *Fracture Mechanics of Rock*, edited by B. Atkinson, pp. 351-428, Academic Press, London, 1987.

Liu, J., and T. Heaton, The effect of slip variability on earthquake slip-length scaling, *pre-print*, 2002.

Ma, K.-F., A. T.-R. Song, S.-J. Lee, and H.-I. Wu, Spatial slip distribution of the September 20, 1999, Chi-Chi, Taiwan, Earthquake (Mw 7.6) - Inverted from teleseismic data, *Geophysical Research Letters*, *27* (20), 3417-3420, 2000.

Madariaga, R., Dynamics of an expanding circular fault, *Bull. Seis. Soc. Am.*, *66*, 639-666, 1976.

Madariaga, R., Implications of stress-drop models of earthquakes for the inversion of stress drop from seismic observations, *Pure Apply. Geophysics*, *115*, 301-316, 1977.

Madariaga, R., On the relation between seismic moment and stress drop in the presence of stress and strength heterogeneity, *J. Geophys. Res.*, *84*, 2243-2250, 1979.

Mai, P.M., and G. C. Beroza, Source scaling properties from finite-fault-rupture models, *Bull. Seis. Soc. Am.*, *90* (3), 604-615, 2000.

Matsuzawa, T., Estimation of seismic wave energy excited by small earthquakes in the western Nagano region, Masters thesis, University of Tokyo, Tokyo, 2001.

Mayeda, K., and W. R. Walter, Moment, energy, stress drop, and source spectra of western United States earthquakes from regional coda envelopes, *J. Geophys. Res.*, *101*, 11,195-11.208, 1996.

Meade, C., and R. Jeanloz, Deep focus earthquakes and recycling of water into the earth's mantle., *Science*, *252*, 68-72, 1991.

Melbourne, T., I. Carmichael, C. DeMets, K. Hudnut, O. Sanchez, J. Stock, G. Suarez, and F. Webb, The geodetic signature of the M8.0 Oct. 9, 1995 Jalisco subduction earthquake, *Geophys. Res. Lett.*, *24* (6), 715-718, 1997.

Mendoza, C., and E. Fukuyama, The July 12, 1993, Hokkaido-Nansei-Oki, Japan, earthquake: coseismic slip pattern from strong-motion and teleseismic recordings, *J . Geophys . Res.*, *101*, 791-801, 1996.

Mendoza, C., and S. Hartzell, Fault-slip distribution of the 1995 Colima-Jalisco, Mexico, earthquake, *Bull. Seis. Soc. Am.*, *89* (5), 1338-1344, 1999.

Molnar, P., and M. Wyss, Moments, source dimensions and stress drops of shallow-focus earthquakes in the Tonga-Kermadac Arc, *Phys. Earth Planet. Inter.*, *6*, 263-278, 1972.

Mori, J., Fault plane determinations for three small earthquakes along the San Jacinto fault, California: Search for cross faults, *J. Geophy. Res.*, *98*, 17,711-17,722, 1993.

Mori, J., and A. Frankel, Source parameters for small events associated with the 1986 North Palm Springs, California, earthquake determined using empirical Green functions, *Bull. Seis. Soc. Am.*, *80*, 278-295, 1990.

Mori, J., H. Kanamori, J. Davis, E. Hauksson, R. Clayton, T. Heaton, L. Jones, and A. Shakal, Major improvements in progress for southern California earthquake monitoring, *EOS Trans. American Geophysical Union*, *79*, 217-221, 1998.

Mott, N. F., Brittle fractures in mild-steel plates - II, *Engineering*, *165*, 16-18, 1948.

Nakayama, W., and M. Takeo, Slip history of the 1994 Sanriku-Haruka-Oki, Japan, earthquake deduced from strong-motion data, *Bull. Seis. Soc. Am.*, *87* (4), 918-931, 1997.

Nazareth, J., The structure of and the distribution of earthquakes within the crust of Southern California, California Institute of Technology, Pasadena, 2002.

Negishi, H., J. Mori, T. Sato, R. P. Singh, and S. Kumar, Aftershock and slip distribution of mainshock, in *A comprehensive survey of the 26 January 2001 earthquake (Mw 7.7) in the state of Gujarat, India, Report by the research team supported by the grant-in-aid for specially promoted research provided by MEXT of Japan in the fiscal year of 2001*, edited by T. Sato, pp. 33-45, 2001.

Newman, A. V., and E. A. Okal, Teleseismic estimates of radiated energy: the E/Mo discriminant for tsunami earthquakes, *J . Geophys . Res.*, *103* (B11), 26885-26898, 1998.

Ogawa, M., Shear instability in a viscoelastic material as the cause of deep focus earthquakes, *J . Geophys . Res.*, *92*, 13801-13810, 1990.

Orowan, E., Mechanism of seismic faulting in rock deformation, *Geol. Soc. Am. Mem.*, *79*, 323-345, 1960.

Ozawa, S., Geodetic inversion for the fault model of the 1994 Shikotan earthquake, *Geophys. Res. Lett.*, *23* (16), 2009-2012, 1996.

Pacheco, J., S. K. Singh, J. Dominguez, A. Hurtado, L. Quintanar, and J. Jimenez, The October 9, 1995 Colima-Jalisco, Mexico earthquake (Mw 8): an aftershock study and comparison of this earthquake with those of 1932, *Geophys. Res. Lett.*, *24* (17), 2223-2226, 1997.

Parsons, I. D., J. F. Hall, and G. A. Lyzenga, Relationships between the average offset and the stress drop for two- and three-dimensional faults, *Bull. Seis. Soc. Am.*, *78* (2), 931-945, 1988.

Polet, J., and H. Kanamori, Shallow subduction zone earthquakes and their tsunamigenic potential, *Geophys. J. Int.*, *142*, 684-702, 2000.

Poliakov, A. N. B., R. Dmowska, and J. R. Rice, Dynamic shear interactions with fault bends and off-axis secondary faulting, *J . Geophys . Res.*, *(submitted)*, 2002.

Pulido, N., and K. Irikura, Estimation of dynamic rupture parameters from the radiated seismic energy and apparent stress, *Geophys. Res. Lett.*, *27* (23), 3945-3948, 2000.

Rabinowicz, E., *Friction and wear of materials*, 244 pp., Wiley, New York, 1965.

Richter, C.F., An instrumental earthquake magnitude scale, *Bull. Seis. Soc. Am.*, *25*, 1-32, 1935.

Ritsema, J., H. J. van Heijst, and J. Woodhouse, Complex shear wave velocity structure imaged beneath Africa and Iceland, *Science*, *286*, 1925-1928, 1999.

Rosakis, A. J., and A. T. Zehnder, On the dynamic fracture of structural metals, *International Journal of Fracture*, *27* (3-4), 169-186, 1985.

Rudnicki, J. W., and H. Kanamori, Effects of fault interaction on moment, stress drop, and strain energy release, *J . Geophys . Res.*, *86* (B3), 1785-1793, 1981.

Ruegg, J. C., J. Campos, R. Armijo, S. Barrientos, and P. Briole, The M_w=8.1 Antofagasta (North Chile) earthquake of July 30, 1995: first results from teleseismic and geodetic data, *Geophys. Res. Lett.*, *23* (9), 917-920, 1996.

Sato, T., K. Imanishi, and M. Kosuga, Three-stage rupture process of the 28 December 1994 Sanriku-Oki earthquake, *Geophys. Res. Lett.*, *23* (1), 33-36, 1996.

Savage, J. C., and M. D. Wood, The relation between apparent stress and stress drop, *Bull. Seismol. Soc. Am.*, *61*, 1381-1388, 1971.

Scholz, C., C. Aviles, and S. G. Wesnousky, Scaling differences between large interplate and intraplate earthquakes, *Bull. Seis. Soc. Am.*, *76*, 65-70, 1986.

Scholz, C. H., Mechanics of faulting, *Ann. Rev. Earth Planet. Sci.*, *17*, 309-334, 1989.

Scholz, C. H., *The mechanics of earthquake faulting*, 438 pp., Cambridge University Press, New York, 1990.

Schwartz, S.Y., Noncharacteristic behavior and complex recurrence of large subduction zone earthquakes, *J . Geophys . Res.*, *104* (B10), 23111-23125, 1999.

Silver, P. G., S. L. Beck, T. C. Wallace, C. Meade, S. C. Myers, D. E. James, and R. Kuehnel, Rupture characteristics of the deep Bolivian earthquake of 9 June, 1994 and the mechanism of deep-focus earthquakes., *Science*, *268*, 69-73, 1995.

Singh, S. K., and M. Ordaz, Seismic energy release in Mexican subduction zone earthquakes, *Bull. Seismol. Soc. Am.*, *84*, 1533-1550, 1994.

Somerville, P., K. Irikura, R. Graves, S. Sawada, D. J. Wald, N. Abrahamson, Y. Iwasaki, T. Kagawa, N. Smith, and A. Kowada, Characterizing crustal earthquake slip models for the prediction of strong ground motion, *Seismo. Res. Let.*, *70* (1), 59-80, 1999.

Starr, A. T., Slip in a crystal and rupture in a solid due to shear, *Proc. Camb. Phil. Soc.*, *24*, 489-500, 1928.

Swenson, J. L., and S. L. Bilek, Source characteristics of the 12 November 1996 M_w 7.7 Peru subduction zone earthquake, *Pure Appl. Geophys.*, *154*, 731-751, 1999.

Takeo, M., S. Ide, and Y. Yoshida, The 1993 Kushiro-Oki, Japan, earthquake-A high stress drop event in a subducting slab, *Geophys. Res. Lett.*, *23*, 2607-2610, 1993.

Tanioka, Y., and F. I. Gonzalez, The Aleutian earthquake of June 10, 1996 (Mw 7.9) ruptured parts of both the Adreanof and Delarof segments, *Geophys. Res. Lett.*, *25* (12), 2245-2248, 1998.

Tanioka, Y., L.J. Ruff, and K. Satake, What controls the lateral variation of large earthquake occurrence along the Japan trench?, *The Island Arc*, *6*, 261-266, 1997.

Tanioka, Y., and K. Satake, Tsunami generation by horizontal displacement of ocean bottom, *Geophys. Res. Lett.*, *23* (8), 861-864, 1996.

Tanioka, Y., K. Satake, and L. J. Ruff, Total analysis of the 1993 Hokkaido Nansei-oki earthquake using seismic wave, tsunami, and geodetic data, *Geophys. Res. Lett.*, *22* (1), 9-12, 1995.

Thio, H. K., and H. Kanamori, Source complexity of the 1994 Northridge earthquake and its relation to aftershock mechanisms, *Bull. Seis. Soc. Am.*, *86*, S84-92, 1996.

Tibi, R., G. Bock, M. Xia, M. Baumbach, and H. Grosser, Rupture processes of the 1999 August 17 Izmit and November 12 Duzce (Turkey) earthquakes, *Geophys. J. Int.*, *144*, F1-F7, 2001.

Tibi, R., C. H. Estabrook, and G. Bock, The 1996 June 17 Flores Sea and the March 9 Fiji-Tonga earthquakes: source processes and deep earthquake mechanisms, *Geophys. J. Int.*, *138*, 625-642, 1999.

Trieman, J. A., K. J. Kendrick, W. A. Byrant, T. K. Rockwell, and S. F. McGill, Primary surface rupture associated with the M_w7.1 16 October, 1999 Hector Mine earthquake, San Bernardino County, California, *Bull. Seis. Soc. Am.*, 2001.

Vassiliou, M. S., and H. Kanamori, The energy release in earthquakes, *Seismol. Soc. Am. Bull.*, *72* (2), 371-387, 1982.

Wald, D. J., and T. H. Heaton, Spatial and temporal distribution of slip for the 1992 Landers, California, earthquake, *Bull. Seismol. Soc. Am.*, *84*, 668-691, 1994.

Wha, S. S., The 1997 Kamchatka earthquake, *Individual Studies by Participants at the International Institute of Seismology and Earthquake Engineering*, *34*, 91-99, 1998.

Wiens, D., Seismological constraints on the mechanism of deep earthquakes: temperature of deep earthquake source properties, *Phys. Earth Planet. Inter.*, *127*, 145-163, 2001.

Wiens, D., and H. J. Gilbert, Effect of slab temperature on deep-earthquake aftershock productivity and magnitude-frequency relationships., *Nature*, *384*, 153-156, 1996.

Wiens, D. A., and J. McGuire, The 1994 Bolivia and Tonga events: fundamentally different types of deep earthquakes?, *Geophys. Res. Lett.*, *22* (16), 2245-2248, 1995.

Winslow, N. W., and L. J. Ruff, A hybrid method for calculating the radiated wave energy of deep earthquakes, *Physics of the Earth and Planetary Interiors*, *115*, 181-190, 1999.

Wood, H. O., and F. Neumann, Modified Mercalli intensity scale of 1931, *Bull. Seis. Soc. Am.*, *21*, 277-283, 1931.

Wu, L.-R., and W.-P. Chen, Rupture of the large (Mw 7.8), deep earthquake of 1973 beneath the Japan Sea with implications for seismogenisis, *Bull. Seis. Soc. Am.*, *91* (1), 102-111, 2001.

Wyss, M., and J. Brune, Regional variations of source properties in southern California estimated from the ratio of short- to long-period amplitudes, *Bull. Seis. Soc. Am.*, *61*, 1153-1168, 1971.

Yagi, Y., and M. Kikuchi, Source rupture process of the Kocaeli, Turkey, earthquake of August 17, 1999, obtained by joint inversion of near-field data and teleseismic data, *Geophys. Res. Lett.*, *27* (13), 1969-1972, 2000.

Yoshiaka, S., and Y. Tokunaga, Numerical simulation of displacement and stress fields associated with the 1993 Kushiro-oki, Japan, earthquake, *Pure Appl. Geophys.*, *152* (3), 443-464, 1998.